MESA-ASSISTED VLS GROWTH OF GAAS NANOWIRES

MESA-ASSISTED VLS GROWTH OF GAAS NANOWIRES

By

MICHAEL B. ROUMELIOTIS, B.Eng. Engineering Physics

A Thesis

Submitted to the School of Graduate Studies

in Partial Fulfillment of the Requirements

for the Degree

Master of Applied Science

McMaster University

MASTER OF APPLIED SCIENCE (2008) McMaster University

(Engineering Physics) Hamilton, Ontario

TITLE: Mesa-assisted VLS Growth of GaAs Nanowires

AUTHOR: Michael B. Roumeliotis, B.Eng. Engineering Physics (McMaster University)

SUPERVISOR: Dr. R.R. LaPierre

NUMBER OF PAGES: xvi, 94

Abstract

Periodic arrays of Au patterns (dots and lines) were produced via electron beam lithography (EBL). GaAs mesas were produced by using the Au structures as a mask and wet etching the GaAs (111)B substrates, leaving Au resting above GaAs pillars. Annealing experiments at typical nanowire growth temperatures (550°C) were performed on both mesa-supported samples and a control sample without mesas, and were later characterized by scanning electron microscopy (SEM). From SEM images, a model is proposed to describe the evolution of the Au seed particle during exposure to typical growth conditions. The Au particle is subject to not only a melting process but is also modified by a volume increase due to incorporating Ga atoms and a subsequent crystal structure change. Palpable discrepancies between the mesa-supported and control samples were observed after annealing experiments, suggesting the mesas were effective in confining the migration of the Au. NWs were then grown via gas source molecular beam epitaxy (GS-MBE). Discernable variation amongst the results was evident when a comparison between annealed samples and the grown counterpart was made. The inconsistency is ascribed to the NW growth process beginning only after supersaturation at the growth interface. This saturation took place only after 2-D film growth on the substrate surpassed the height of the mesas rendering the structures less functional.

Acknowledgments

I would like to thank my supervisor Dr. Ray LaPierre, whose guidance and commitment throughout my Master's degree has made the process an informative and insightful experience. I would also like to acknowledge the staff at the Centre for Emerging Device Technology and the Brockhouse Institute for Materials Research, particularly Steve Koprich for his technical support with SEM imaging. Special recognition should be noted to Dr. Todd Simpson from the University of Western Ontario whose support with the electron beam lithography process was invaluable. Finally, I would like to thank my family and friends that provide immeasurable motivation.

Table of Contents

List of Figures

List of Tables

1 Introduction

1.1 Semiconductor Nanowires

The continuing reduction in device size as well as the necessity to more adeptly control device size in order to accommodate the complexity of electronic devices has prominently defined the need to shift beyond photolithography techniques that are resolution-limited. Enormous pursuit has been focused on developing nanowires (NWs) for electronic, biomedical, and photonic device applications [1.1-5]. NWs are typically grown with tremendous aspect ratios which possess diameters of tens of nanometers while lengths can be measured on the order of a few microns [1.6]. In electronic devices, these NWs have already been used as the building blocks of logic gates and FETs [1.7-9]. In the biomedical field, NWs have been shown to detect single biological particles [1.10, 11]. Recent optical developments include implementing these NWs in integrated circuit components such as waveguides, LEDs, modulated lasers, and photodetectors [1.12-15].

Since the first proposal of a photonic bandgap effect [1.16], this subject has found rapidly increasing interest. Varying dielectric structures can be designed to control electromagnetic behavior in photonic crystals in an analogous way to electron behavior being controlled in semiconductors. Controlled growth of NWs in predetermined sites would have promising influence in photonic bandgap engineering and new methods of waveguiding. The focus of this thesis is in discussing the results of a mesa-assisted

approach to Vapor-Liquid-Solid (VLS) growth in order to control the location of wires on a substrate.

1.2 Vapor-Liquid-Solid Growth Process

When NWs are grown via the VLS growth mechanism, there is typically a preparation phase in which a metal film (commonly Au) is deposited on the substrate surface. The substrate is later heated for NW growth which causes the metal to agglomerate and create a random distribution of metal particles on the substrate [1.17, 18]. These metal seed particles provide the site for the growth of NWs when exposed to the appropriate conditions.

The VLS growth mechanism was first proposed in 1964 by Wagner to describe the growth of silicon wires [1.19]. Since the early silicon growths, the process has been used to make more complex III-V semiconductor wires including GaAs, InP, and AlGaAs [1.20-22]. Beyond growing simple NWs, many other, more complex devices have been created, including NW heterostructures [1.23, 24] and simple lasing devices [1.25].

Described in further detail in section 2.8, the VLS growth process utilizes a supply of adatoms at the substrate where, under elevated temperatures, migration of these impinging atoms to the metal seed particle can occur. Once saturation of adatoms at the metal-substrate interface occurs, growth of the NW begins [1.19].

1.3 Mesa-assisted Nanowire Growth

Through the implementation of electron beam lithography (EBL), well-patterned arrays of Au are synthesized and the formation of randomly distributed Au seed particles through annealing is averted. However, the substrate is still exposed to high temperatures (~550°C) during the molecular beam epitaxy (MBE) growth procedure of the NWs. Therefore, migration of the seed particle is still a recurring problem in EBL-patterned samples. In order to circumvent the Au migration, mesa structures are produced in an attempt to confine the migration of the Au via surface tension. The ambition to produce periodic arrays of arbitrary, well-controlled dimension is met by patterning not only dots of varying diameter and Au thickness but also lines structures. NWs are typically cylindrical structures in which dot seed particles are ideal. However, in an attempt to confine the shape of the NW to be non-cylindrical, arbitrarily shaped Au structures confined by surface tension are patterned in an attempt to guide NW growth in the shape of the seed particle.

In this thesis, the effect of mesa structures on the wire growth is made in Chapter 3. Juxtaposition of samples annealed with and without mesa support is made to determine the effect of high temperatures on the Au seed particle. More importantly, however, is the characterization of the resulting periodic array with mesa support after annealing when compared to its counterpart after growth.

2 Experimental Methods

2.1 Scanning Electron Microscopy Theory

Imaging with electrons becomes a powerful tool when the limited resolution of optical microscopy becomes evident. That is, the relatively large wavelengths of optical radiation become insufficient in resolving smaller structures. Electron wavelengths can be described by Equation (2.1), known as the de Broglie wavelength:

$$\lambda = \frac{h}{p} \tag{2.1}$$

where h is Planck's constant and p is the momentum of the particle. The energy associated with an electron accelerated through a potential difference, V, is written in Equation (2.2):

$$E = \frac{p^2}{2m} = qV \tag{2.2}$$

Rearranging equations (2.1) and (2.2), the wavelength of an electron can be described in terms of the accelerating voltage.

$$\lambda = \frac{h}{\sqrt{2mqV}} \tag{2.3}$$

As voltages approach the order of tens of kV, the electron wavelengths are on the order of picometres. Typically, electrons are accelerated between 5 and 20 kV. A basic SEM system is shown below in Figure 2.1.

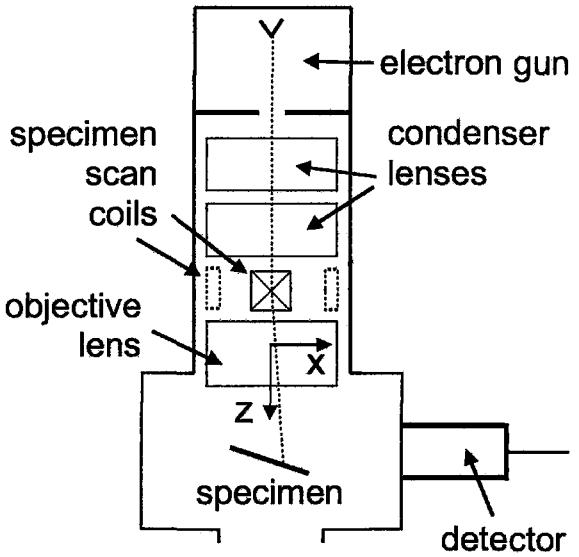

Figure 2.1. SEM instrumentation schematic. Adapted from Egerton [2.1].

The charged nature of electrons allows the electrons ejected from an electron source to be manipulated by a series of magnetic condenser lenses. Spray diaphragms reduce the conical area of emitted electrons to interact with the condenser lenses [2.1]. After passing through both lenses, the final objective lens provides the ability to focus the beam to a fine point on the sample (approximately a few nanometers in diameter), illustrated in Figure 2.2. The beam finally interacts with the sample producing both backscattered and secondary electrons.

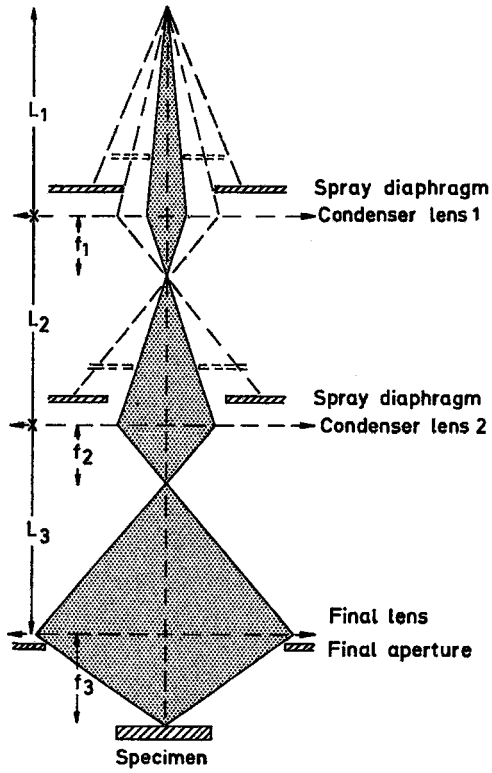

Figure 2.2. Focusing instrumentation in a typical SEM system. Lens focal points, f, and lens spacing, L, are shown. Adapted from Reimer [2.2].

Electrons that interact with the sample partake in both inelastic and elastic scattering events. Elastic scattering events impart negligible loss of energy in the interaction and produce backscattered electrons. Inelastic processes involve a loss of energy when interacting with the sample and produce secondary electrons, Auger electrons, and x-ray photons. A schematic illustrating these features is shown in Figure 2.3.

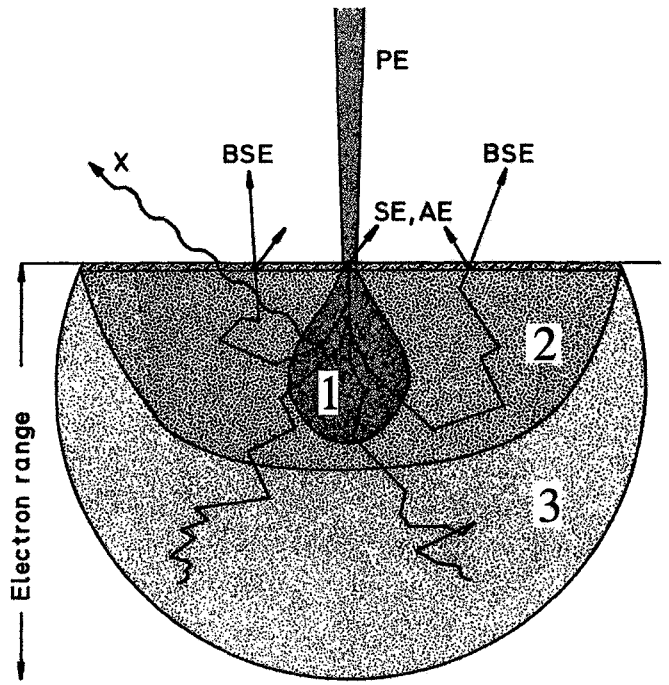

Figure 2.3. Model of the electron interaction region. X-ray photons (X), primary electrons (PE), backscattered electrons (BSE), secondary electrons (SE), and Auger Electrons (AE) are labeled. The regions are labeled indicating where the byproducts of departed energy are created: (1) x-ray photons, (2) escape depth of backscattered electrons, (3) entire volume of interaction, and (thin hatched region) escape depth of secondary and Auger electrons [2.3].

Backscattered electrons are produced when incident electrons interact with the positively charged nuclei of atoms within the sample. The large mass of the nuclei causes negligible energy loss during the interaction. The higher energy backscattered electrons have much greater escape lengths when compared to secondary electrons. Consequently, the ability to resolve topographical details with backscattered electrons is very limited. However, the probability of primary electron interaction with nuclei in the sample increases with increasing atomic number. This provides backscattered electrons with the unique ability to sharply contrast different elemental components of the sample [2.4].

Secondary electrons are produced when primary electrons interact with electrons in the sample. The high kinetic energy of the primary electrons is imparted partially onto the atomic electrons. Accordingly, the secondary electrons have relatively low energy and small escape depths on the order of a few nanometers. Since the escape depth of the secondary electrons is relatively small, these electrons are very useful in imaging topographical features of a sample [2.5].

2.2 Scanning Electron Microscopy System

All SEM measurements were made via the JEOL JSM-7000F SEM system at McMaster University. GaAs samples were mounted on steel stubs with carbon adhesive tape to ensure good electrical conductivity. The samples were then placed on a sample stage in the evacuation chamber which was initially pumped down to ~10^{-3} Pa. A movable transfer arm was then used to place the sample stage into the high vacuum chamber. The pressure in the chamber was lowered further to ~10^{-5} Pa where the shutter to the field emission electron beam could be opened. Unless imaging with tilted views, a working distance of 6mm was selected and the sample was raised to the corresponding height in the chamber. At the lowest magnification (25x), an image was formed at this working distance and the focusing process began.

At low magnification (below 3-5000x), artifacts on the surface of the sample were centered and focused via the coarse focus control to more accurately adjust the height of the sample stage to the appropriate position. Beyond a magnification of 5000x, the fine focus control was used to reduce astigmatism effects. The accelerating voltage was

typically set relatively low (~5-10 keV) when imaging Au patterns as the patterns tended to be easier to locate. The voltage was set much higher (~15-20 keV) when imaging nanowire patterns that had been grown.

2.3 Electron Beam Lithography Theory

Electron beam lithography (EBL) provides a means to circumvent the physical limitations of photolithography techniques (largely resolution). The operating principle in EBL device fabrication is similar to photolithography. That is, a mask is created in resist such that metal deposition followed by lift-off will leave metal only in prescribed areas. In EBL, this is done using a finely focused electron beam that is scanned over the sample and deflected on and off to produce the desired pattern. The resist is specifically sensitive to electrons which break or join molecules that can later be selectively removed by the immersion of the resist in a development solution.

Through the use of focusing lenses, modern electron beams can be focused to a few nanometers in diameter. While a number of factors prohibit the electron beam diameter from being perfectly focused, the practical resolution limit is largely due to the interaction and forward scattering of incident electrons in the resist [2.6]. This forward scattering process is the fundamental source of the limitations of the minimum linewidth in patterns using EBL technology.

2.4 Electron Beam Lithography Process

Prior to electron beam exposure, the samples were etched in 10% buffered HF solution for 30 seconds followed by a rinse in deionized water. A positive resist was spun onto the samples at 2500RPM to provide a nominal thickness of 250nm. ZEP 520A resist (provided by Nippon Zeon) was diluted with ZEP thinner at a ratio of 1.4 parts of resist per 1 part thinner and was spun onto the samples where they were later baked at 180°C for two minutes on a hot plate. Electron beam exposure was conducted using the LEO 1530 field emission SEM at the University of Western Ontario. Typical patterns were exposed to 85μC/cm^2 with the exception of a number of patterns which required varying doses due to the feature sizes of the structures. These patterns were 60nm lines, 60nm dots, and 250nm dots which were exposed at 0.35nC/cm^2, 170μC/cm^2, and 75μC/cm^2, respectively. The required dose is determined by both the size of the features and the proximity of nearby features. In close-packed features a relatively small dose is required while in small isolated features higher doses are needed. Optimal doses were all selected by experimentation to produce well-formed structures. This sample was recreated identically 7 additional times to provide a total of 8 samples (summarized in Table 2.1 and 2.2). The line and dot patterns are shown below in Figures 2.4 and 2.5.

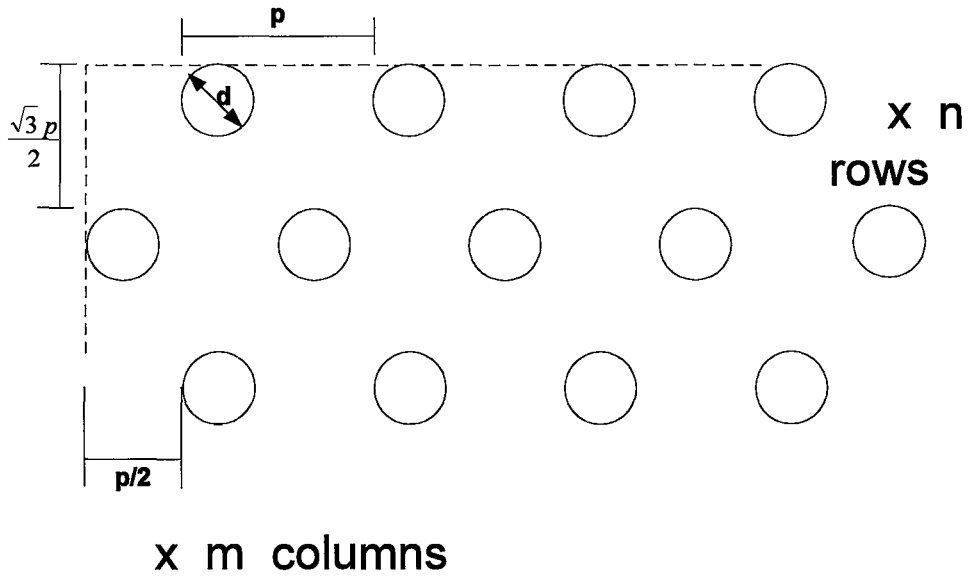

Figure 2.4. Generic outline of dot patterns. As the diameter, d, of the dots increased, the centre-to-centre pitch remained constant creating less space between Au structures.

d (nm)	p (nm)	m	n
60	500	> 100	> 100
100	500	> 100	> 100
140	500	> 100	> 100
180	500	> 100	> 100
250	500	> 100	> 100

Table 2.1. Parameters for dot patterns with dot diameter, d, pitch between dots, p, and the number of rows and columns, m and n respectively.

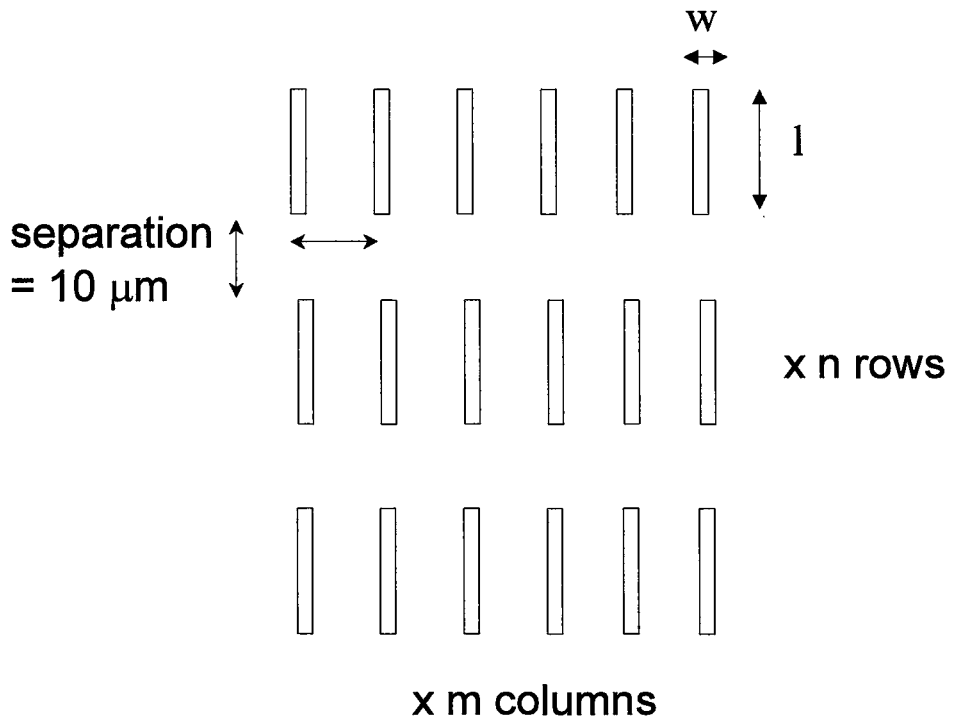

Figure 2.5. Generic outline of line patterns. The length of wires, l, was 10μm while the linewidth, w, was varied over the set of Au structures.

w (nm)	l (μm)	m	n
60	10	> 100	> 100
90	10	> 100	> 100
120	10	> 100	> 100
150	10	> 100	> 100
200	10	> 100	> 100
300	10	> 100	> 100

Table 2.2. Parameters for line patterns with linewidth w, length of lines, l, and the number of rows and columns, m and n respectively.

The samples were then developed in ZED N50 (also provided by Nippon Zeon) for 2 minutes. Au was subsequently deposited using a custom electron beam evaporation system and Temescal 4-pocket electron beam source at the University of Western Ontario.

Au was deposited at the desired thicknesses (15, 25, 35, and 50nm) which were measured by *in situ* quartz crystal monitoring which was in turn calibrated by prior deposition. The liftoff of remaining resist and unwanted Au was done at room temperature. All samples were soaked in acetone until the resist film could be removed with a gentle spray from an acetone squirt bottle. Typical soak times were in the range of 8 to 12 minutes.

2.5 Wet Etching Details

All samples that were etched to produce mesa structures were first rinsed in deionized water. While soaking in a running water bath, the etchant was prepared. A beaker was filled with 250mL of deionized water. 3mL of H_2O_2 was added to the solution first, followed by 3mL of NH_4OH. Each sample was removed from the H_2O bath and dried with a nitrogen gun. The sample was then placed in the etchant for 5 seconds and was gently agitated during the soak. After 5 seconds, the sample was quickly removed from the etchant and immediately placed into a second beaker of deionized water. The sample was left in the beaker for approximately 2 minutes and then transferred to the running water bath to further clean the sample of unwanted etchant that would further etch the GaAs substrate. After soaking in the running water bath for approximately 5 minutes, the samples were removed and sprayed with nitrogen to remove any remaining water from the sample.

2.6 Atomic Force Microscopy Theory

In addition to SEM, samples were characterized by atomic force microscopy to measure the thickness of Au and the etch depth described above. AFM implements the use of a small probe at the apex of a cantilever to scan over the sample surface. The AFM system utilizes a piezoelectric scanner that moves the sample when a voltage is applied. This piezoelectric system is used to move the sample in 3 dimensions. A schematic of this is shown below in Figure 2.6.

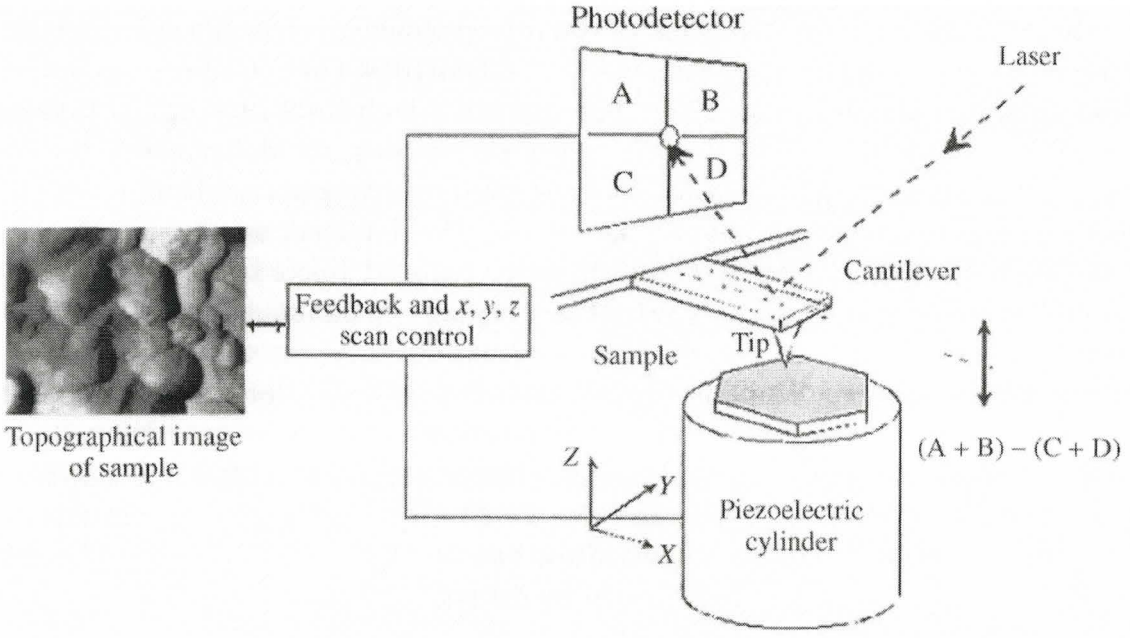

Figure 2.6. Schematic of AFM operating principle. A position-sensitive photodetector tracks the position of the probe as it is repositioned in response to the height contour of the sample. Adapted from Drelich and Mittal [2.7].

To form an image, the tip is brought close to the surface and scanned over the sample. The cantilever will deflect according to the varying surface contour A laser

reflects off the back of the cantilever surface and is directed into a position-sensitive photodetector mapping the movement of the cantilever.

The repulsive forces that exist between overlapping electron orbitals between the probe and the surface of the sample cause the deflection of the cantilever arm. The forces acting on the tip vary depending on the imaging mode. The first mode is constant-force mode which maintains the cantilever deflection at a constant level by moving the piezoelectric scanner. Feedback adjusts the height of the sample away from the cantilever to maintain constant deflection. This simply manipulates the z-component of the piezoelectric scanner. The alternate method is constant-height mode which employs the use of varying the cantilever deflection such that the force between the sample and the probe is maintained. These modes of operation allow surface fluctuations to be recorded on the order of single Angstroms. However, when imaging is completed in an air environment, layers of water are adsorbed which produces an additional attractive force due to the interfacial tension.

To avoid the shortcomings of contact-mode imaging, an alternate method can be used to monitor the interaction between the probe and the sample. This utilizes the longer-range attractive forces that are much weaker than the repulsive forces of electron orbitals that are documented in contact-mode imaging. The mode (referred to as tapping mode) oscillates the cantilever electrically to produce amplitudes of approximately 100nm so that the cantilever is tapping the surface of the sample. The system is set to detect perturbations in the oscillation amplitude that vary from the default oscillation position. Figure 2.7 below illustrates the forces taken advantage of in the different AFM

imaging modes. The tapping mode and other non-contact modes utilize the longer-range forces while contact-mode maps the closer-range electron orbitals.

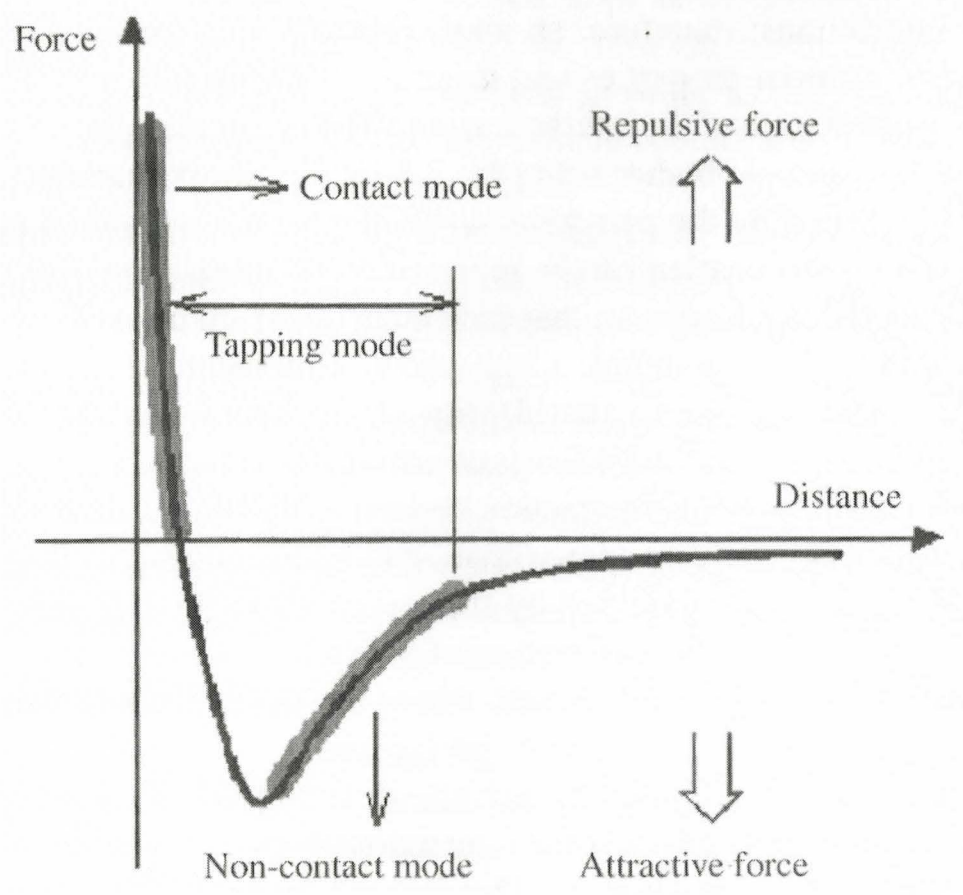

Figure 2.7. Force v. Distance curve that reflects the interaction between the scanning probe and sample during AFM measurements. Adapted from Drelich and Mittal [2.7].

2.7 Atomic Force Microscopy Measurements

Samples to be surveyed via AFM were first placed on a stage where a camera was focused over the tip. All imaging was done with the Digital Instruments MultiMode AFM system and the Nanoscope IIIa Scanning Probe Microscope Controller The AFM system

is stationed on an air table to minimize the influence of vibration on the image. Tips were made of silicon and supplied by Asylum Research. Once the camera was viewing the probe, the laser was manually aligned on the tip of the probe. A mirror was then lowered in place such that the laser would reflect onto the photodetector sensitive to laser position. By adjusting the position of the sample stage, the probe could be placed at any location on the sample and engaged. When the probe was in the appropriate position, tapping mode was engaged to begin oscillation of the tip.

2.8 Molecular Beam Epitaxy and Vapor Liquid Solid Nanowire Growth

Molecular beam epitaxy is a system by which semiconductor films can be grown with deposition control on the scale of atomic layers. The notion behind supplying the atoms in a molecular beam is that the pressure in the chamber is sufficiently small such that the mean free path of the incident species is larger than the distance traveled to the substrate providing no interaction between atoms or molecules in the molecular beams before impinging the substrate.

The basic outline of an MBE system is shown below in Figure 2.8.

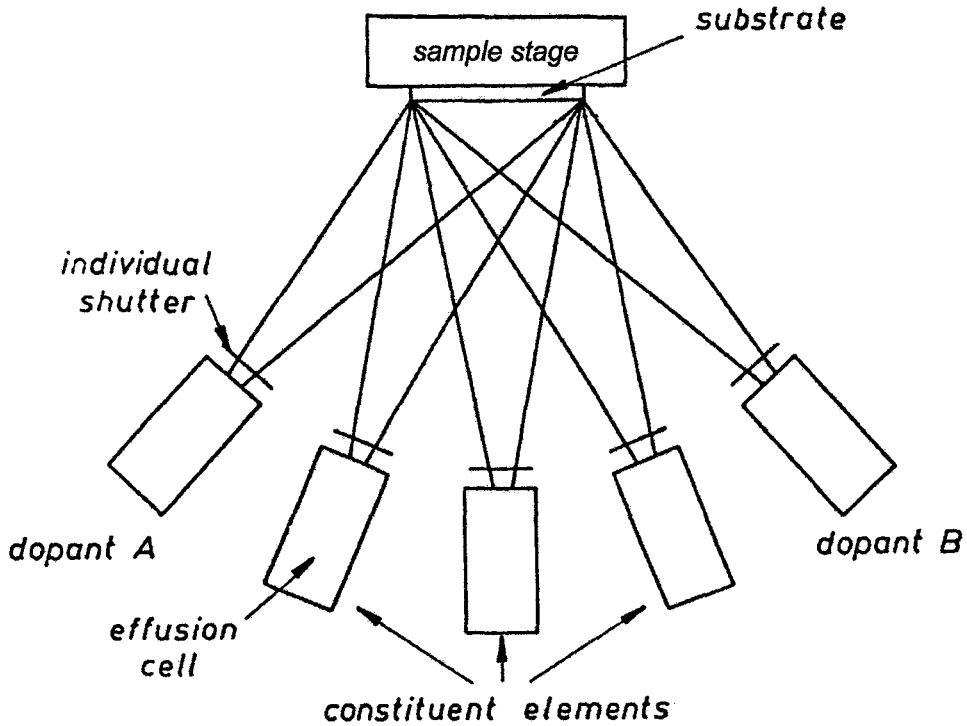

Figure 2.8. Schematic of MBE chamber. The sample is placed on a rotating sample stage where cells containing the constituent elements are individually shuttered. Adapted from Herman and Sitter [2.8].

The sample on which the film is grown is mounted on a rotating stage and sealed in an ultra-high vacuum chamber (~10^{-9} Torr). The rotating stage allows a uniform deposition of atoms on the substrate since the molecular beams may be off-centered from the substrate. Group III materials are typically supplied from a solid elemental effusion source. Group V materials are supplied via hydrides (AsH_3 for As and PH_3 for P). The gas sources are cracked thermally at 950°C to produce predominantly dimers (As_2 and P_2) that subsequently impinge the substrate.

This MBE chamber is used to grow nanowires via the VLS process. The VLS mechanism supplies atoms to the substrate of the sample mounted in the chamber. The atoms impinging the substrate on and around the Au collector particles (designed via

EBL) eventually become saturated at the collector-substrate interface. When saturation occurs at the interface, bottom up growth of the nanowires occurs. The pathways by which impinging atoms reach the growth interface are: (i) adsorbed atoms impinge and diffuse through the substrate and wire walls, (ii) adsorbed atoms impinge the surface of the collector particle and proceed via bulk diffusion to the interface, and (iii) adsorbed atoms impinge the surface of the collector and migrate along the surface of the particle to the interface. Adsorbed atoms impinging the substrate and diffusing to the growth interface is the dominant mechanism in the VLS growth process.

3 Analysis of Mesa-assisted VLS Growth

3.1 Introduction

Nanostructures are under development for a multitude of far-reaching applications. Synthesis of NWs in many different materials systems as well as heterostructure NWs and superlattice structures [3.1-3] have been reported. Despite substantial advances in the processing of NWs that have been made, effort has largely been focused on improving the control of single NW structures. To further explore NW applications, the next step is to produce highly uniform structures which are individually accessible along with the ability to define a variety of key structural parameters. Specifically, control of the structures height and diameter are especially critical when applying these structures to electrical and optical applications in which dimension are fundamentally important. The development of highly periodic NW devices to influence and confine the propagation of electromagnetic waves through a dielectric material is desirable.

While reasonable success has been achieved using metal-organic chemical vapor deposition techniques to produce periodic structures [3.4], limited success has been achieved with growing uniform structures via GS-MBE. Despite the success in MOCVD growth, there are unique characteristics native to MBE grown NWs making success highly desirable through the VLS growth mechanism. MBE growth has the potential to create NWs of much greater aspect ratios due to the very high diffusion length of adatoms on the surface [3.5-7]. In this thesis, an attempt is made to produce highly uniform arrays of NWs with precise control of structure diameter. Periodic patterns were

produced through EBL patterning and later analyzed via SEM imaging in intermittent stages to provide insight into the process responsible for the formation of the NWs. A relatively novel approach to localizing the growth of NW structures is made by wet-etching "mesas" to confine the seed particles.

In this chapter, the results of these NW growths are reported. A model is proposed to describe the results observed after exposing the seed particles to elevated temperatures in order to elucidate the mechanisms driving the migration and nucleation of Au on the substrate surface.

3.2 Motivation and Analysis

Metallic seed particles for NW growth are typically synthesized by Au evaporation followed by thermal annealing. However, this process produces a randomized distribution of Au seed particles on the substrate surface as illustrated by the SEM images in Figure 3.1. Therefore, this method of Au nanoparticle synthesis is incapable of producing patterned arrays of NWs or precisely positioned NWs essential in some applications such as photonic bandgap devices.

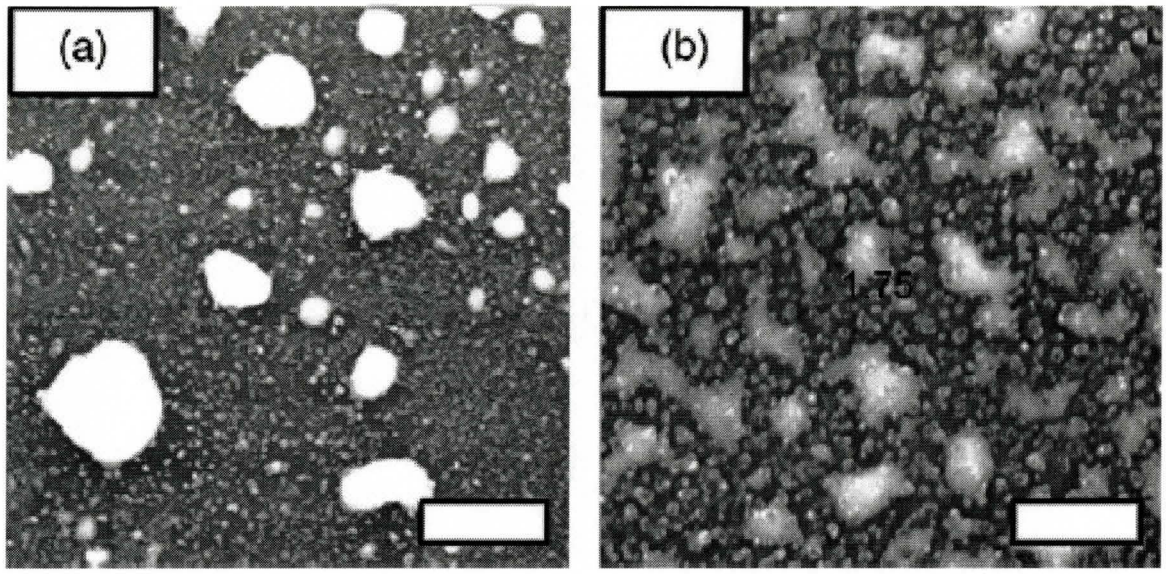

Figure 3.1. Plan view SEM images of surfaces after the annealing of a 4-nm-thick Au film at 500°C for 5 minutes on GaAs (111)B substrate. (a) was treated with HF solution while (b) with HCl solution. The length bars indicate 500nm [3.8].

To produce patterned arrays of NWs, electron beam lithography (EBL) may be employed to fabricate Au templates. The Au arrays used in this study were prepared on n-type GaAs (111)B substrates with a doping concentration range between $1.4x10^{18}$ and $2.3x10^{18}$ atoms/cm^3 (provided by AXT). The substrates were submitted to a 20 minute UV-ozone treatment to remove contamination from hydrocarbons and grow a sacrificial layer of oxide film. The sample oxide was etched in 10% buffered HF solution for 30 seconds followed by a rinse in deionized water ZEP 520A resist was spun onto the sample at 2000 RPM to provide a nominal thickness of 250 nm, and subsequently baked at 180°C for 2 minutes. Electron beam exposure was conducted using a LEO 1530 field emission SEM with NPGS lithography system and TSL laser interferometric stage. Each sample was prepared with 11 distinct patterned arrays consisting of 5 sets of dots at 60,

100, 140, 180 and 250nm diameters and 6 sets of lines at 60, 90, 120, 150, 200, and 300nm widths (all 10μm in length) as outlined in Tables 2.1 and 2.2.

All patterns were produced by an electron beam current of 85μC/cm^2 with the exception of the 60nm lines, 60nm dots, and 250nm dots which were exposed at 0.35nC/cm^2, 170μC/cm^2, and 75μC/cm^2, respectively. After e-beam exposure, the samples were developed in ZED N50 for two minutes. The latter procedure was repeated 7 additional times on different substrates pieces, producing 8 samples in total. After development, Au was deposited over the patterned resist using a custom electron beam evaporation system and Temescal 4-pocket electron beam source. Two identical sets containing 4 samples each were fabricated. Each of the 4 samples within each set had a different Au thickness. The Au thicknesses were 15, 25, 35, and 50nm. After Au deposition, a liftoff procedure was performed at room temperature whereby the resist and overlying Au was removed, leaving behind the Au on the substrate surface created by the openings in the resist as defined by the electron beam exposure. The samples were soaked in acetone until the resist film could be removed with a gentle spray from an acetone squirt bottle. Typical soak times were in the range of 8 to 12 minutes. This process resulted in Au patterns as illustrated by the SEM images in Figure 3.2.

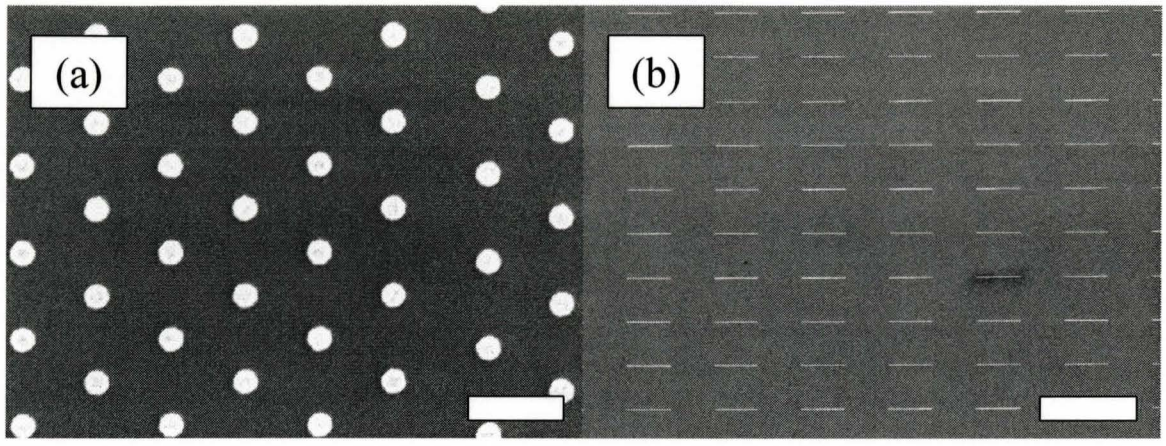

Figure 3.2. Top view SEM images of EBL-patterned Au. (a) Dot array. (b) Line array. The length bars indicate 500nm and 20μm, respectively.

Next, annealing experiments were conducted on the set of 4 samples previously imaged by SEM. Annealing was performed using an AG Associates Mini-Pulse rapid thermal annealing (RTA) furnace to simulate the thermal treatment that is typical of MBE conditions during NW growth (550°C). The samples were placed in the RTA at room temperature and ramped to 550°C at a rate of 5°C per second. Following RTA experiments, the samples were again imaged in the same SEM system to analyze the effects of annealing on the Au patterns. Representative SEM images are shown in Figures 3.3 and 3.4 for dots and lines, respectively, illustrating the destructive consequences of exposing the samples to elevated temperatures. Clear evidence of Au migration is shown for the dots in Figure 3.3. In addition to Au migration, the patterned lines in Figure 3.4 demonstrate clear evidence of the Au structure "fractionating" after exposure to high temperatures. In this scenario, the structure remains localized within the area prescribed by the initial EBL patterning, but the lines break up into smaller Au structures. Further results are presented in Section 3.6 where the results of annealing the as-deposited Au are

compared with the results of mesa-supported Au for each of the dots and lines of varying thickness.

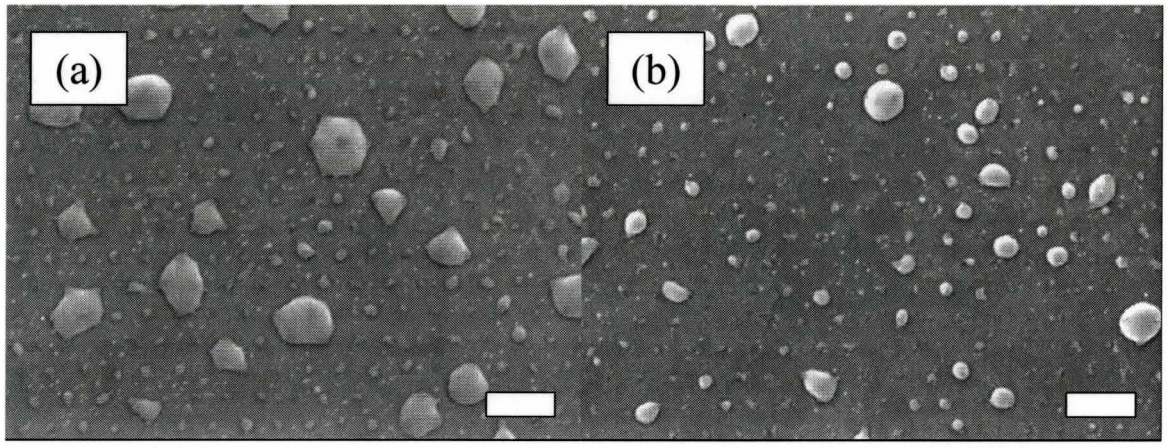

Figure 3.3. Results of annealing EBL-patterned dot samples exposed to 550 °C for 5 minutes. (a) 250nm dots, 25nm Au thickness (b) 140nm dots, 35nm Au thickness. The length bars indicate 1μm.

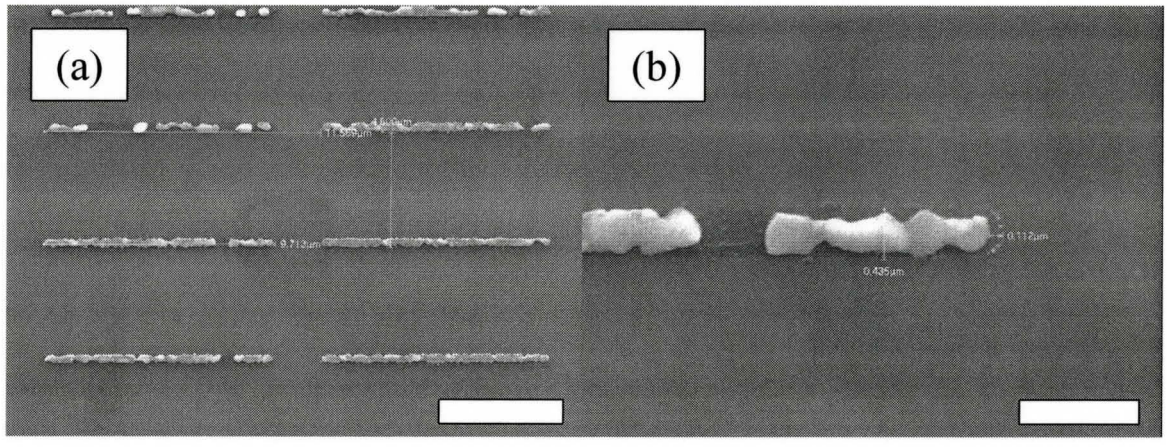

Figure 3.4. Results of annealing EBL-patterned line samples exposed to 550 °C for 5 minutes. The length bars indicate 5μm and 1μm, respectively.

To understand the change in Au patterns that occurs at elevated temperatures, we refer to the phase diagram of Au-Ga alloys in Figure 3.5 [3.9]. During NW growth, Ga uptake into the Au particle due to alloying with the substrate and due to the supply of Ga

from the molecular beam causes the Au particle to change towards an Au-Ga alloy. This composition change of the Au seed particle was confirmed by energy dispersive X-ray spectroscopy (EDS) measurements performed at room temperature in the transmission electron microscope (JEOL system at McMaster University). The fraction of Ga atoms present in the Au seed particle was found (by EDS) to be between 18 and 22% [3.8], indicating the existence of the β' phase [3.9]. The As content in the Au particle was also measured by EDS and was found to be negligible, which is consistent with the negligible solid solubility of As in Au at the growth or annealing temperature (550°C) as determined by the Au-As phase diagram, shown below in Figure 3.6 [3.10].

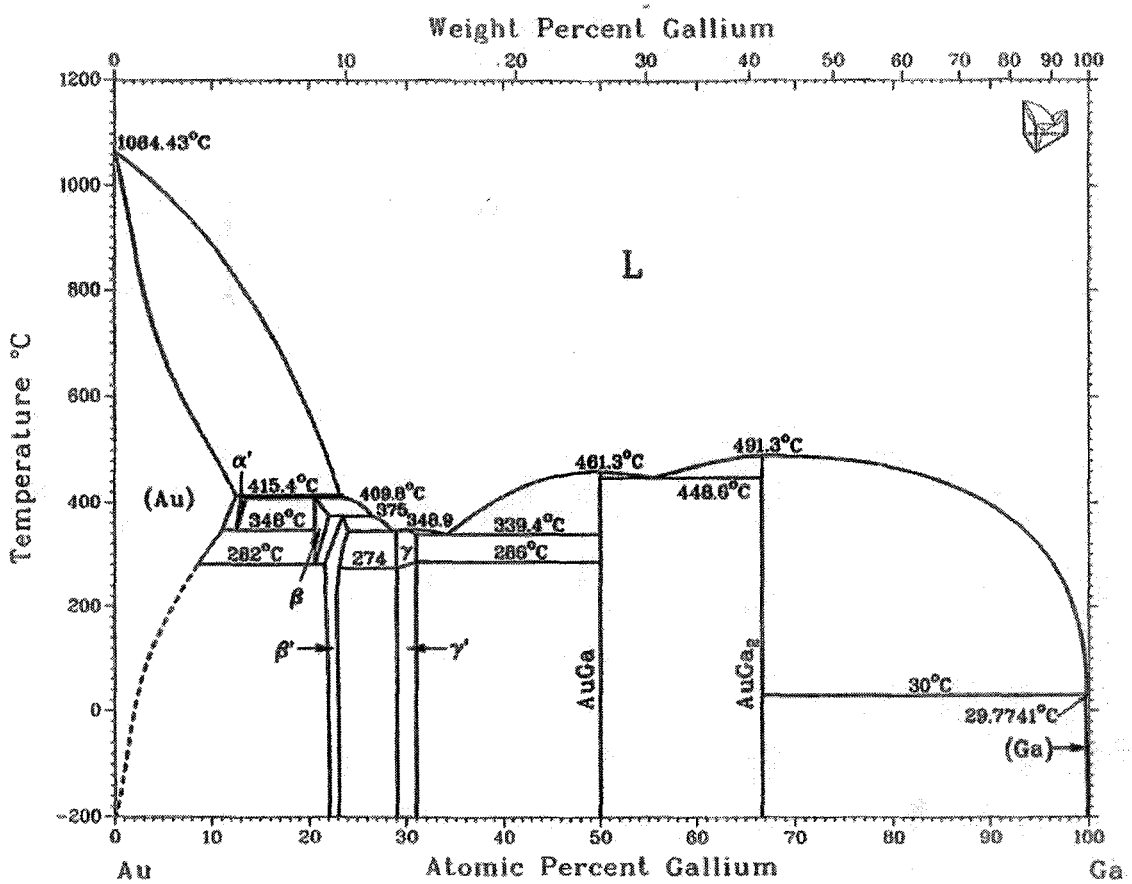

Figure 3.5. Au-Ga Phase Diagram [3.9].

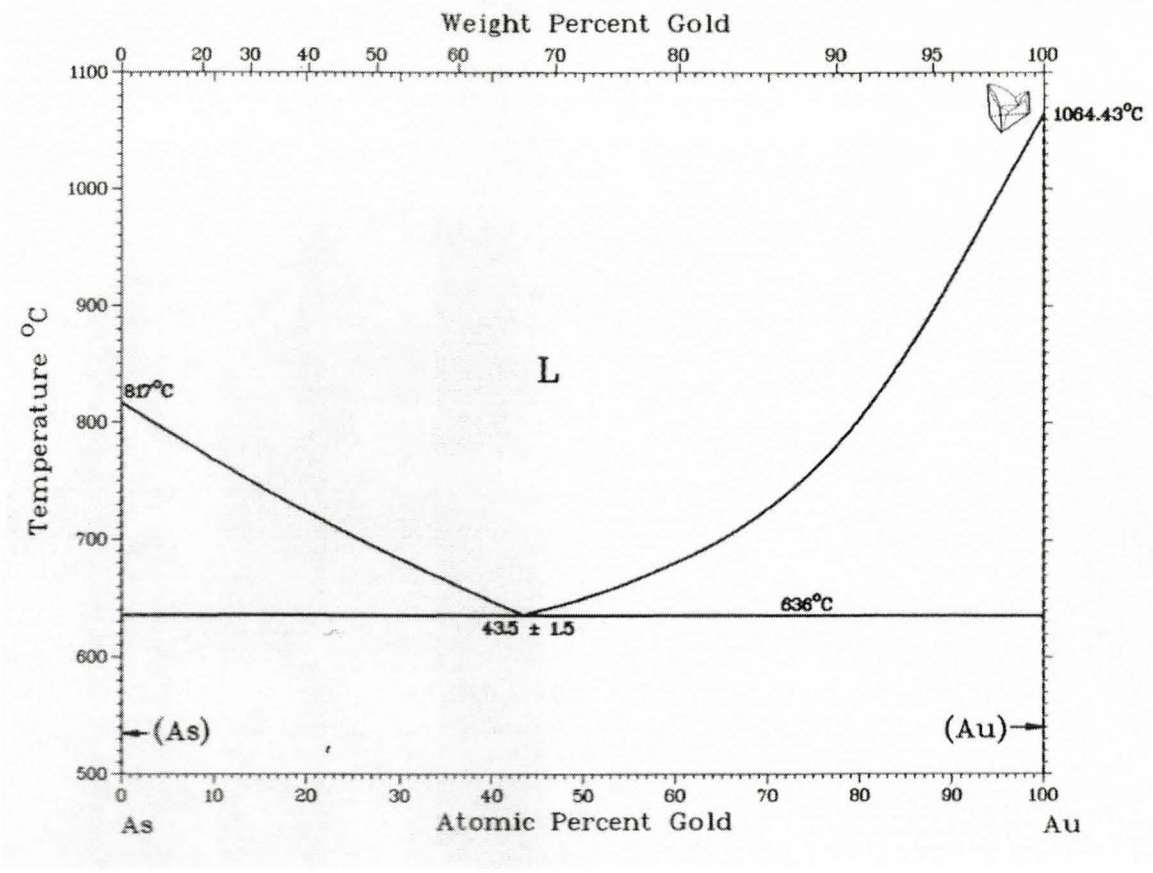

Figure 3.6. Au-As Phase Diagram [3.10].

Assuming the same Au-Ga alloy composition of the β' structure exists at the NW growth temperature of 550˚C, and referring to Figure 3.5, the phase of the Au-Ga alloy is evidently liquid at the growth temperature. The EDS analysis therefore indicates that the patterned Au dots and lines will melt at the annealing or NW growth temperature (550˚C) due to the formation of an Au-Ga alloy The discrete Au structures that existed prior to annealing are therefore compromised by melting resulting in a broader size distribution of the particles and random positions. That is, some of the Au structures appear to have unified via cohesive forces in the liquid Au to create larger Au islands, although smaller islands are also observed. This liquid alloy state is evidently mobile on the substrate

surface and promotes the pattern disturbances seen in Figures 3.3 and 3.4. The motion of the Au particles can be explained by examining the effect of Ostwald ripening which describes the interaction of islands in close proximity and sintering which describes the interaction of small islands in contact [3.11]. In Ostwald ripening, a collection of islands of varied size exists in close proximity and over time the interaction of the islands becomes evident as a consequence of the desire to minimize the free energy of the structures. Larger particles, with their higher volume to surface area ratio, represent a lower energy state. Atoms from the smaller island will tend to diffuse to the larger island. In sintering, the interacting islands are in contact. Shown in Figure 3.7 below is the time evolution of 2 islands in contact.

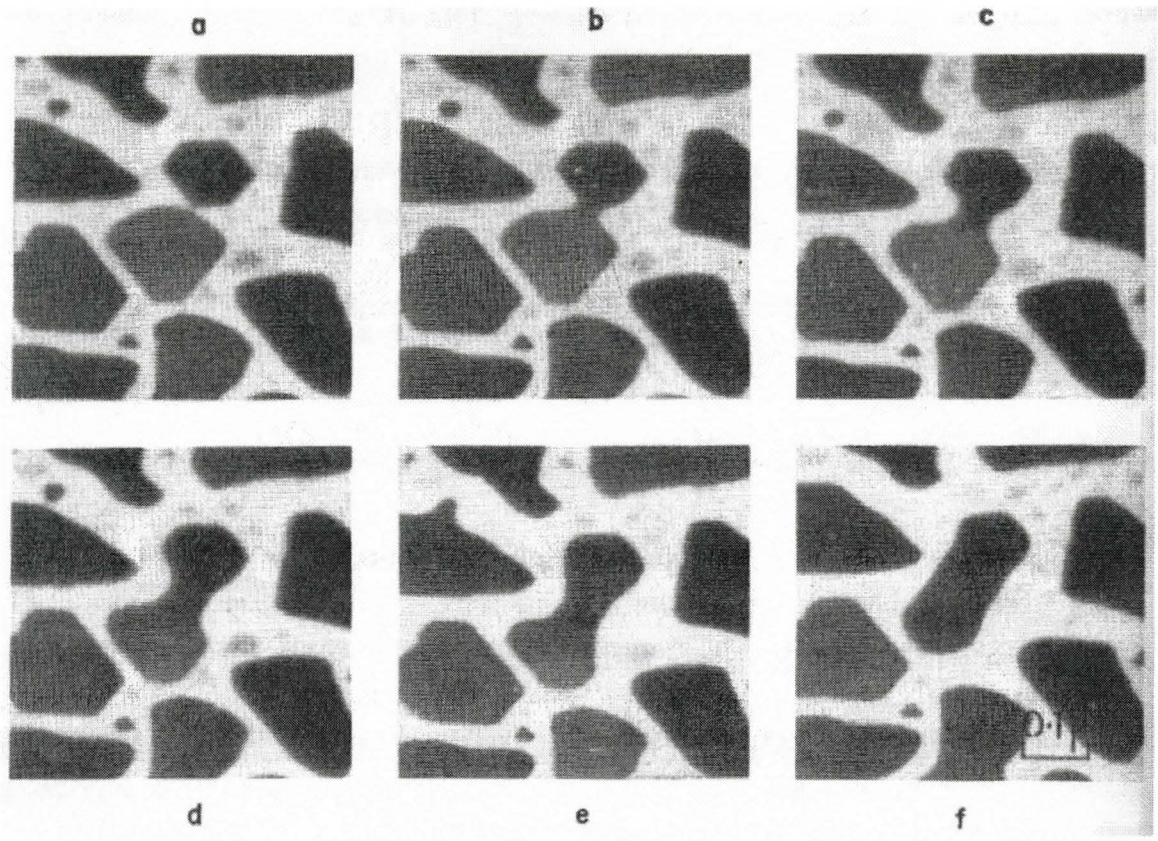

Figure 3.7. Successive electron micrographs of Au deposited on molybdenite at 400°C illustrating coalescence by sintering. (a) arbitrary zero time, (b) 0.06 seconds, (c) 0.18 seconds, (d) 0.50 seconds, (e) 1.06 seconds, (f) 6.18 seconds [3.11].

The formation of a neck region is quickly evident in (b) of Figure 3 7 The driving force for the growth of this region is the minimization of free energy described in Ostwald ripening. Beyond this, atoms located in the neck have a lower activity than atoms in the original islands. This causes an effective concentration gradient and the neck region is allowed to develop by mass transport of the molecules. A combination of both phenomena likely contributes to the results observed in Figure 3.3 providing a seemingly randomized distribution of Au particle sizes.

Due to the change in state of the Au particle to a liquid Au-Ga alloy upon heating from room temperature to the NW growth temperature, the shape of the particle is expected to change due to surface tension forces [3.12]. Consider the change in shape of a single solid Au dot upon the formation of a liquid Au-Ga alloy and before the onset of particle migration. The Au deposited on the substrate after EBL patterning is ideally in the form of a simple cylinder or pillbox with volume:

$$V_i = h \cdot \pi \cdot r_i^2 \tag{3.1}$$

where h is the pillbox height (thickness of the Au deposition), and r_i is the initial EBL-defined radius of the Au dot. However, this initial Au pillbox changes from a solid to a liquid state due to the uptake of Ga from the substrate surface during annealing and from the impinging Ga flux during NW growth. In a liquid state, the most energetically favorable shape for the Au-Ga alloy is that of a truncated sphere due to the surface tension between the liquid alloy particle, the substrate, and the vapor surrounding the system. The resulting Au-Ga island is a truncated sphere creating a contact angle θ with the substrate that is less than 90°, as illustrated in Figure 3.8. The volume V of a truncated spherical island is given by [3.13]:

$$V = a_3 \cdot r_f^3 \tag{3.2}$$

where

$$a_3 = \frac{\pi\left[2 - 3\cos(\theta) + \cos^3(\theta)\right]}{3} \tag{3.3}$$

and r_f is the Au-Ga island radius.

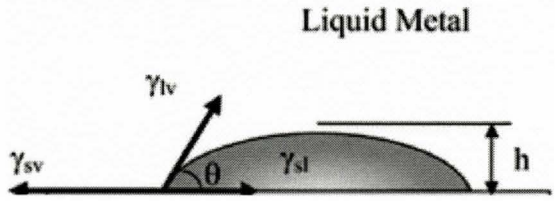

Figure 3.8. An illustration of a contact angle formed between the liquid seed particle and substrate. γ indicates the surface tension between different interfaces. γ_{sv} the tension between solid and vapor, γ_{sl} the tension between solid and liquid, and γ_{lv} the tension between liquid and vapor [3.13].

The contact angle θ of several Au-Ga islands on the substrate surface was measured directly by cross-sectioning the annealed Au dots using a focused ion beam in an SEM. Cross-sectioned Au-Ga islands were prepared from 15nm thickness Au dots annealed at 550°C for 5 minutes. The FIB images provide a direct measurement of the contact angle θ of the Au-Ga island with the substrate surface at room temperature. It is assumed that the contact angle measured at room temperature is similar to that at 550°C; i.e., cool down of the liquid Au-Ga alloy freezes the contact angle. Figure 3.9 shows the results of SEM imaging after FIB cross-sectioning of a typical Au-Ga island. Through examining 4 images similar to Figure 3.9, an average contact angle was found to be 55° ± 5°

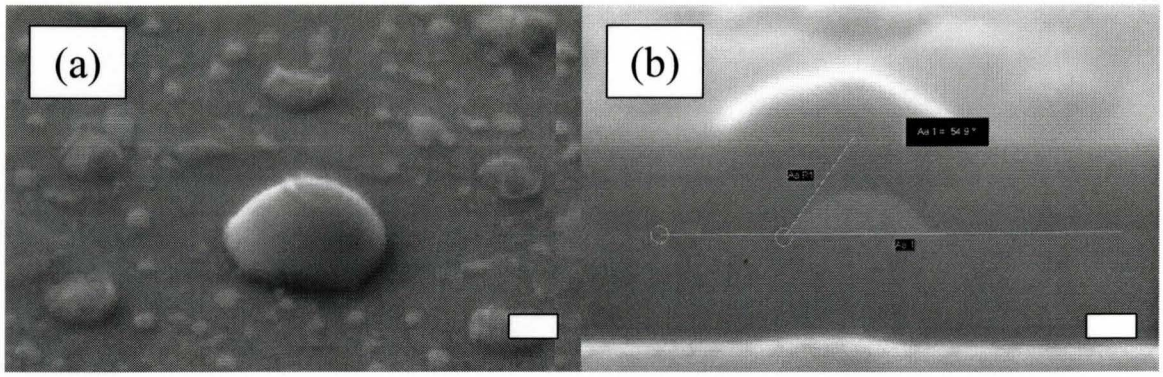

Figure 3.9. (a) SEM Image of a Au-Ga island. (b) Cross-sectional image of the same Au-Ga particle in (a) showing a natural contact angle of 55° made with the substrate. The length bar indicates 100nm.

Equating Equations (3.1) and (3.2) allowed a determination of the expected Au-Ga island diameters r_f for each of the dots in Table 3.1 by using the average contact angle of 55° as determined by FIB, the initial radius r_i of each dot as prescribed by EBL, and the initial Au dot height, h. Table 3.1 shows the calculated Au-Ga island diameters expected after annealing. The effects of Ostwald ripening and sintering compromised the integrity of the structures without mesa support such that this calculation only applies to the isolated Au islands before any cohesive forces cause islands to unify and change size. In the calculations of Table 3.1, the actual Au dot diameters as measured by SEM were used rather than the nominal diameters which were somewhat larger As shown in Table 3 1 and Figure 3.10, the diameter of the Au-Ga island increases with thickness of the initial Au dot. The results of Table 3 1 will be used below when discussing the effect of mesas on the Au annealing. Cells in Table 3 1 were shaded in which the resulting Au-Ga island diameter changed by less than 25% compared to the mesa diameter, as discussed in a later section.

Nominal Initial Au Dot Diameter	Actual Initial Au Dot Diameter	Au-Ga Island Diameter (nm)			
		15 nm thick Au deposit	25 nm thick Au deposit	35 nm thick Au deposit	50 nm thick Au deposit
60 nm	63.3	83.6	99.2	110.9	125.0
100 nm	91.6	117.5	139.3	155.9	175.6
140 nm	130.4	147.1	174.4	195.0	219 7
180 nm	170.0	174.0	206.3	230.8	259.9
250 nm	245.5	216.5	256.7	287 1	323.4

Table 3.1. Expected Au island diameter after melting of various Au dot diameters and thicknesses. Shaded regions are discussed in the text.

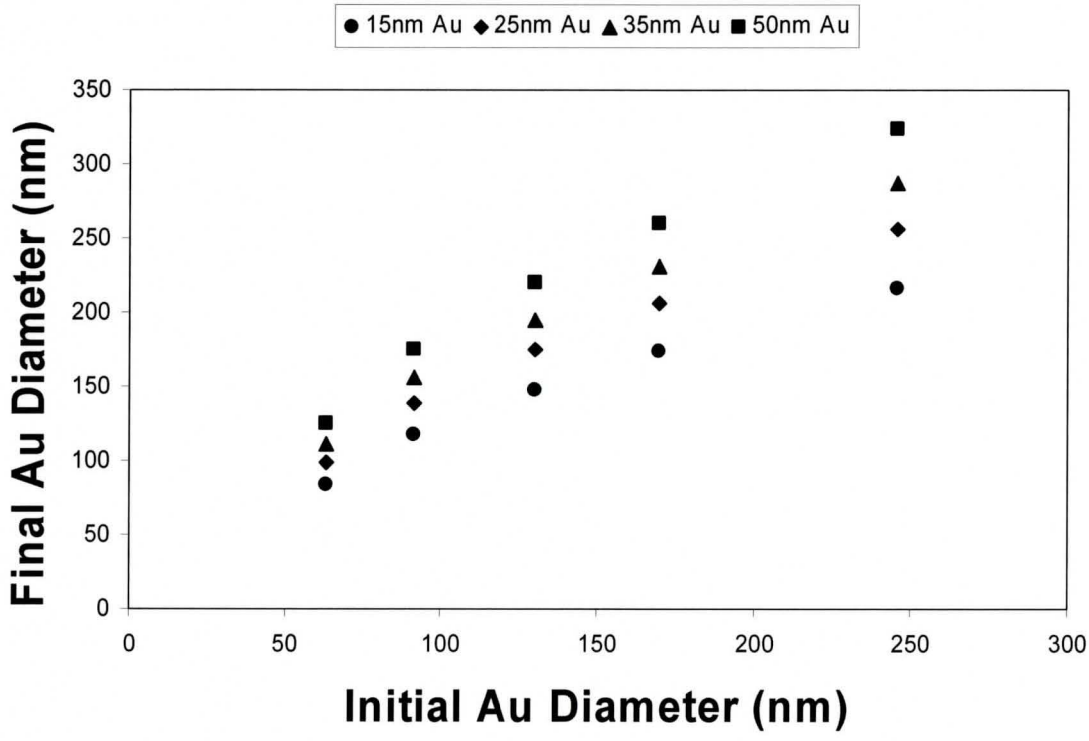

Figure 3.10. The Au-Ga ellipsoid diameter (ordinate) after melting of an initial Au dot pillbox with the indicated diameter (abscissa) as calculated from Table 3.1.

The predicted diameter in Table 3 1 does not account for the increase in volume experienced by the Au particle due to the uptake of Ga. As mentioned previously, the seed particle contains approximately 18 to 22 atomic percent Ga after growth [3.8]. The

volume of the truncated sphere can be adjusted to incorporate the influx of Ga atoms. Pure Au possesses face-centered cubic crystal structure with lattice parameter 4.079Å and 4 atoms per unit cell [3 14]. By dividing the volume of the initial Au pillbox in Equation 3.1 by the unit cell volume of the Au crystal structure and multiplying by 4 atoms per unit cell, we can determine the total number of Au atoms available in the pillbox. To calculate the revised final volume of the truncated Au-Ga sphere, the crystal structure of the Au-Ga alloy must be known. The Au-Ga alloy exists in the hexagonal crystal structure with lattice parameters a = b = 7.64Å and c = 2.73Å [3.15]. The volume of this particular unit cell is 138Å^3 and contains 2 atoms of Ga and 7 atoms of Au. Hence, by dividing the total number of available Au atoms in the pillbox as determined above by 7, and multiplying by 138 Å^3, we arrive at the total volume of the Au-Ga island. Using the contact angle as before, the diameter of the truncated sphere is calculated accounting for the uptake of Ga atoms. The results in Table 3.2 indicate slightly larger Au-Ga island diameters when the uptake of Ga is included. Cells in Table 3.2 were shaded in which the resulting Au-Ga island diameter changed by less than 25% compared to the mesa diameter, as discussed in a later section.

Nominal Initial Au Dot Diameter	**Actual Initial Au Dot Diameter**	**Au-Ga Island Diameter (nm)**			
		15 nm thick Au deposit	**25 nm thick Au deposit**	**35 nm thick Au deposit**	**50 nm thick Au deposit**
60 nm	63.3	94.7	112.3	125.6	141.5
100 nm	91.6	121.2	143.7	160.7	181.0
140 nm	130.4	153.3	181.8	203.4	229 1
180 nm	170.0	183.0	217.0	242.7	273.4
250 nm	245.5	233.8	277.2	310.1	349.3

Table 3.2. Expected Au-Ga island diameter after melting of various Au dot diameters and thicknesses. Shaded regions are discussed in the text.

To prevent the migration and fractionation of Au particles on the substrate surface that occurs at elevated temperatures, an attempt was made to confine the Au dots and lines by the fabrication of "mesas" In this approach, as illustrated in Figure 3 11, mesas were fabricated in which the Au patterns are supported above GaAs islands. Intuitively, there exists a range of dot diameters and thicknesses which may be contained by the mesa and remain localized. Conversely, sufficiently thick Au dots cannot be contained by the mesa and the liquid particle is likely to "spill" over the edge of the mesa and migrate on the substrate surface. On the other hand, too small a diameter of the Au dots would cause fractionation of the Au structure on top of the mesa.

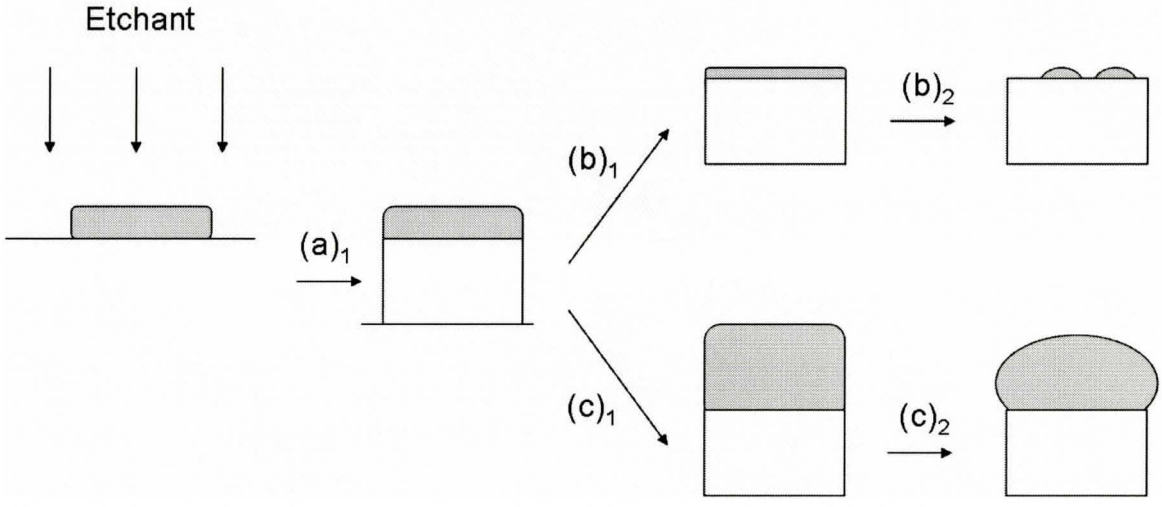

Figure 3.11. Path (a_1) illustrates the process which selectively etches the GaAs substrate while using the Au pillbox as a mask. Path (b) depicts the outcome after a film too thin is applied which allows fractionation to occur within the localized mesa structure. Path (c) depicts the outcome after a film too thick is applied which forces the Au to eventually spill over the edge when the surface tension cannot support the Au structure that has broadened beyond the confines of the mesa.

4 of the 8 samples were prepared for mesa fabrication using the patterned Au as an etch mask. The samples were etched for five seconds in the following solution:

$$3 \cdot NH_4OH : 3 \cdot H_2O_2 : 250 \cdot H_2O \qquad (3.4)$$

This procedure etched the GaAs substrate but was inactive with respect to the Au structures. This effectively allowed the Au patterns to be used as a mask by which mesa structures could be etched into the surface of the GaAs substrate. Prior to the application of this process to the Au patterned samples, a calibrated etch rate was first established using specially fabricated calibration samples. The calibration samples were fabricated using GaAs (111)B substrates with one area of the substrate surface covered by a shadow mask made of aluminum and the remaining region of the substrate exposed. A nominal thickness of 25nm of Au was then deposited on the masked substrate using the electron beam evaporation system. In this way, a thin film of Au was applied in one region of the substrate. The Au thickness in this region was verified by a step-height measurement using atomic force microscopy.

After applying the etchant described in Equation (3.4) for a duration of 30 seconds, the resulting etch depth, and therefore the etch rate, was determined by an AFM step-height measurement of the Au film. This process was repeated on different samples (with the same preparation) to determine the etch rate for various dilutions of the etchant as shown in Figure 3.12. Dilution of the etchant was performed by adding deionized water to 3mL of NH_4OH and 3mL of H_2O_2.

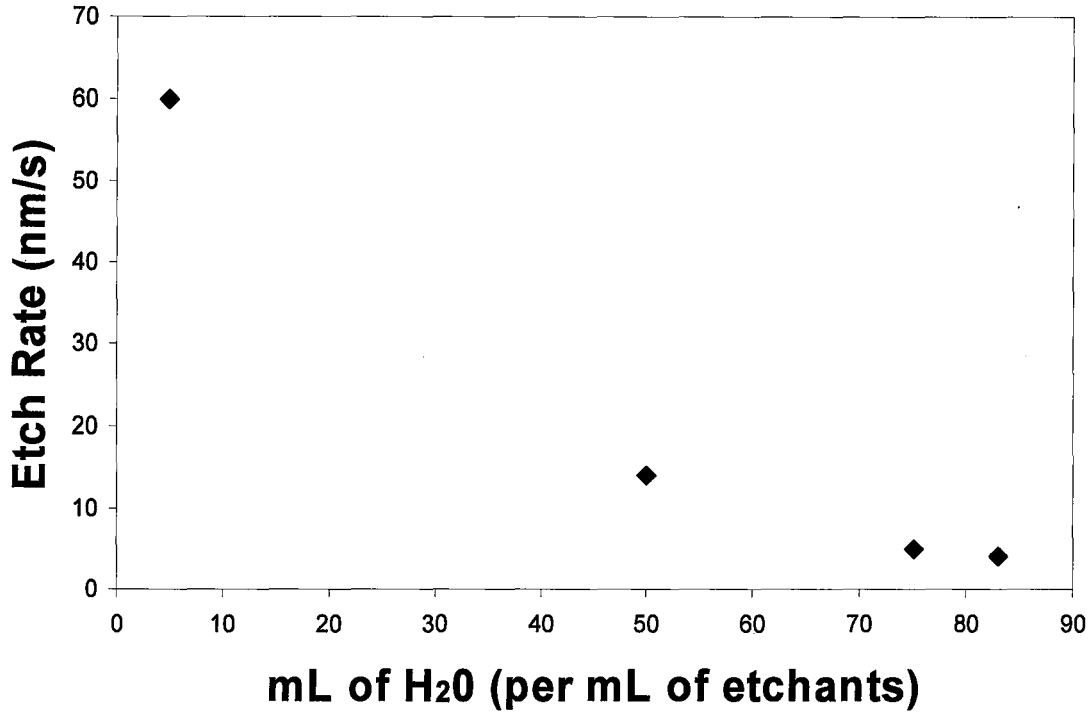

Figure 3.12. Graph illustrating H_2O dilution. All recipes possessed 3mL of both NH_4OH and H_2O_2.

To avoid undercutting of the GaAs, target mesa heights were chosen to be between 20 and 30nm, which is less than the smallest Au dot diameter of 60nm. After calibration of the etch rates as illustrated in Figure 3.12, the etchant was applied to the EBL patterned samples for 5 seconds. To verify the presence of mesas after etching, SEM imaging was performed as illustrated in Figures 3.13 and 3.14 for 350nm diameter dots (test sample) after a 5 second etch duration with etch rate of 6nm/s, indicating that well-formed structures with little undercutting are easily produced. The expected depth under these conditions was 30nm, while 100nm (accounting for the 60° tilt) of etch depth is evident in Figure 3.13.

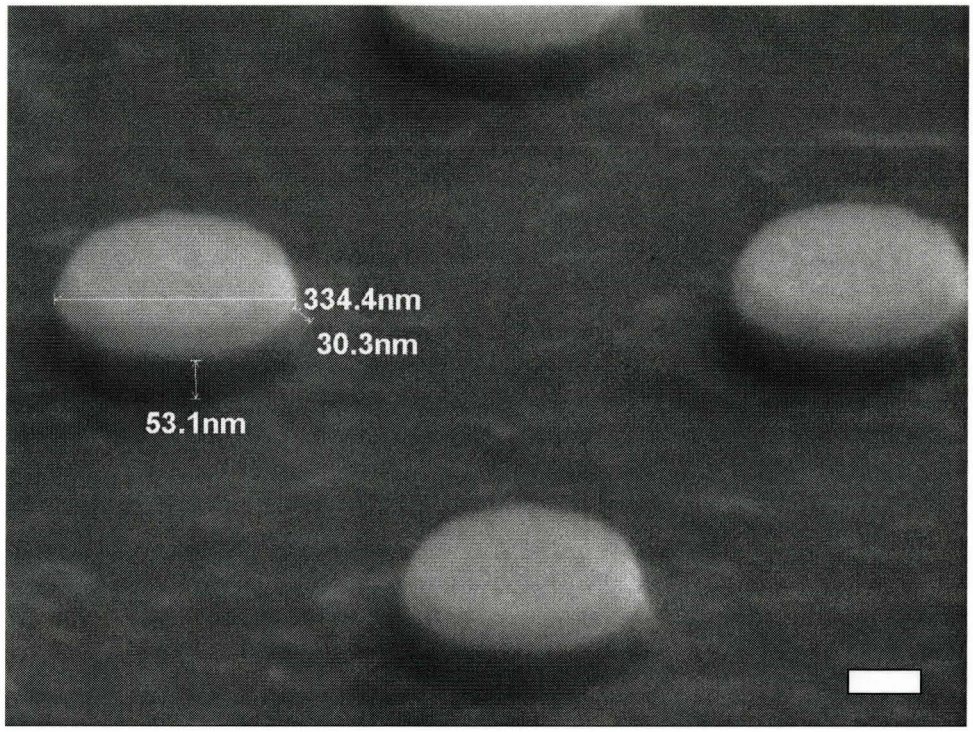

Figure 3.13. 60° tilted SEM view showing EBL-patterned Au dots after wet etching. Clearly visible GaAs mesa structures are evident. The length bar indicates 100nm.

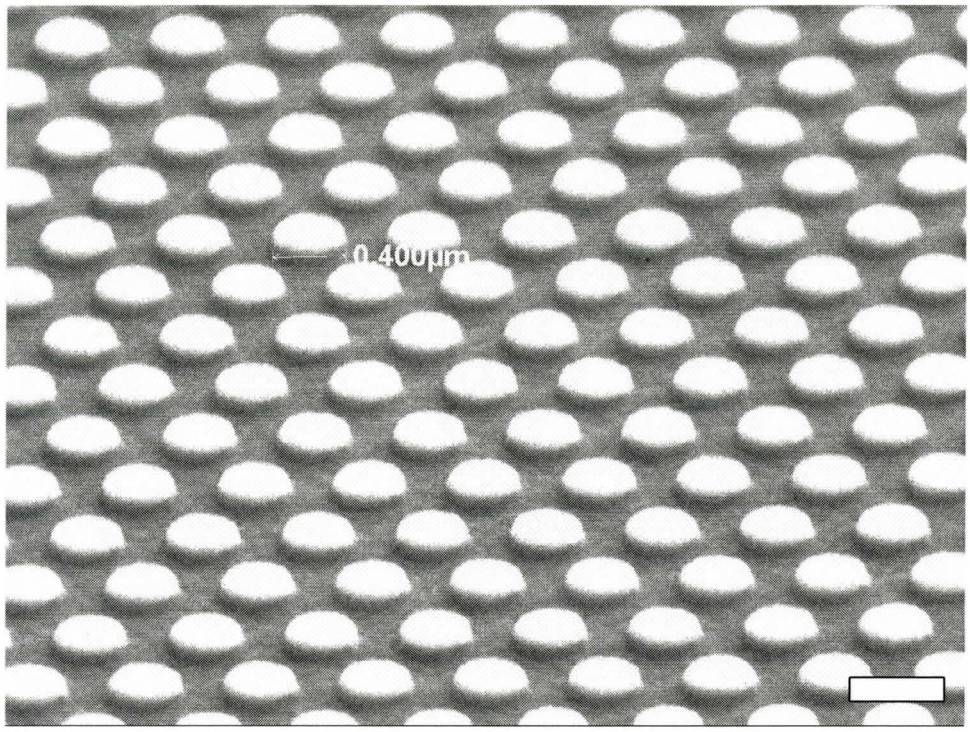

Figure 3.14. EBL-patterned sample after etching. Clearly visible GaAs mesa structures are evident. The length bar indicates 500nm.

After etching to define mesas, the mesa-supported Au structures were subjected to rapid thermal annealing (RTA) in the same manner as described earlier for the non-mesa samples. In the subsequent sections, the effect of annealing on the Au patterns will be assessed for as-deposited (no mesas) and mesa-supported structures. The results for each of the nominal Au thicknesses of 15, 25, 35, and 50nm are presented in separate sections below

3.3 Mesa Assisted Annealing vs. Non-mesa Assisted Annealing (Dots)

In this section, a comparison of mesa-assisted and non mesa-assisted samples is made to contrast the quality of the periodic array after annealing with and without mesa support. Dot and line structures of different thicknesses are discussed separately. It should be noted that in some samples, the 100nm dot structures could not be relocated after etching.

3.31 15nm Au Thickness Dot Structures

In all cases of annealing without mesa support, the original periodic array was disrupted. Migration of Au particles is evident in all samples and the quality of the array is compromised. Figures 3.15 to 3.19 reveal the influence of mesas for Au dot diameters of 60, 100, 140, 180, and 250nm nominal diameter structures. Figures 3.15(a) to 3.19(a) (left-hand images) demonstrate typical results for samples annealed without mesa support. The periodic array appears disrupted when the Au-Ga particles melt and was provided greater freedom to migrate on the surface of the substrate. However, the SEM images in Figures 3.15(b) to 3.19(b) (right-hand images) indicated that the mesa supported Au dots appeared more stationary. This is particularly evident in Figures 3.17 to 3.19.

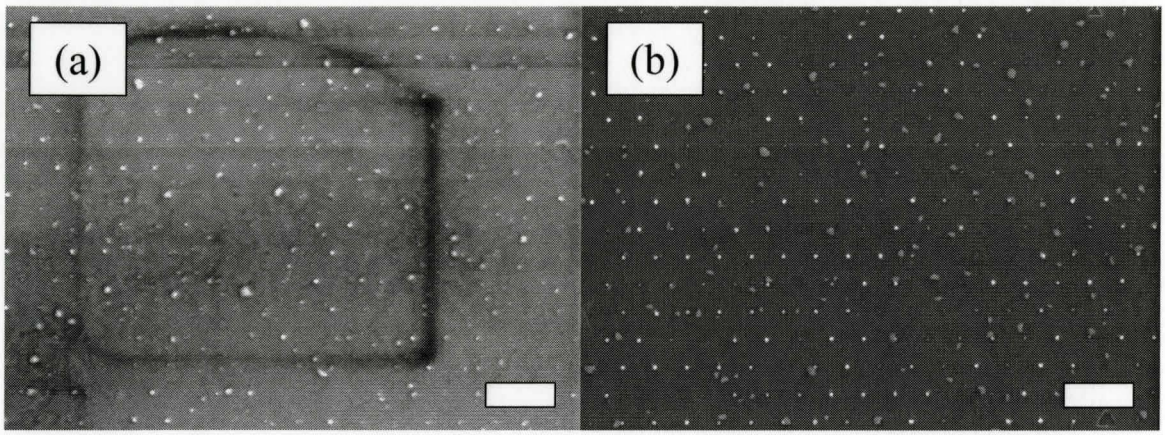

Figure 3.15. Top view SEM images of 15nm thick Au dots of 60nm nominal diameter annealed at 550°C for 5 minutes. (a) 60nm dots without mesa support. (b) 60nm dots with mesa support. The length bars indicate 1μm.

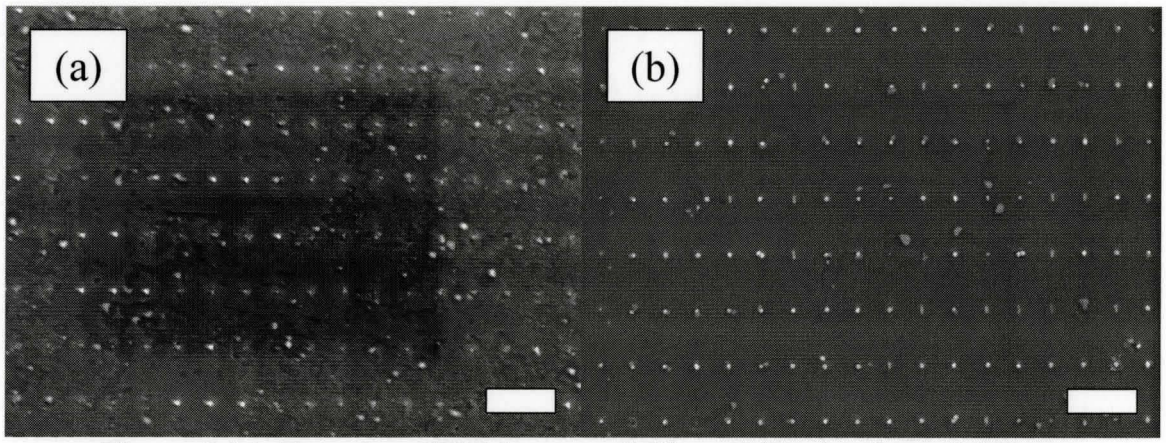

Figure 3.16. Top view SEM images of 15nm thick Au dots of 100nm nominal diameter annealed at 550°C for 5 minutes. (a) 100nm dots without mesa support. (b) 100nm dots with mesa support. The length bars indicate 1μm.

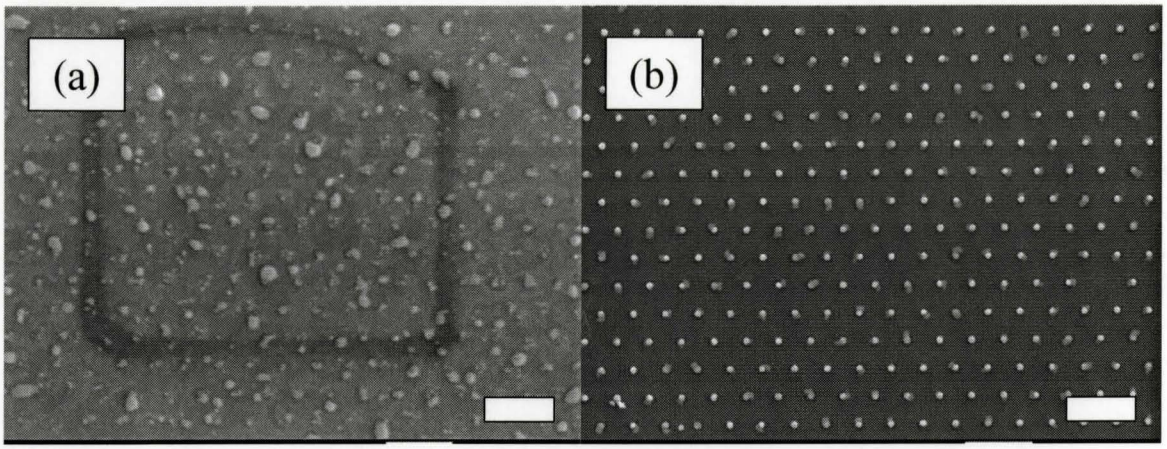

Figure 3.17. Top view SEM images of 15nm thick Au dots of 140nm nominal diameter annealed at 550°C for 5 minutes. (a) 140nm dots without mesa support. (b) 140nm dots with mesa support. The length bars indicate 1μm.

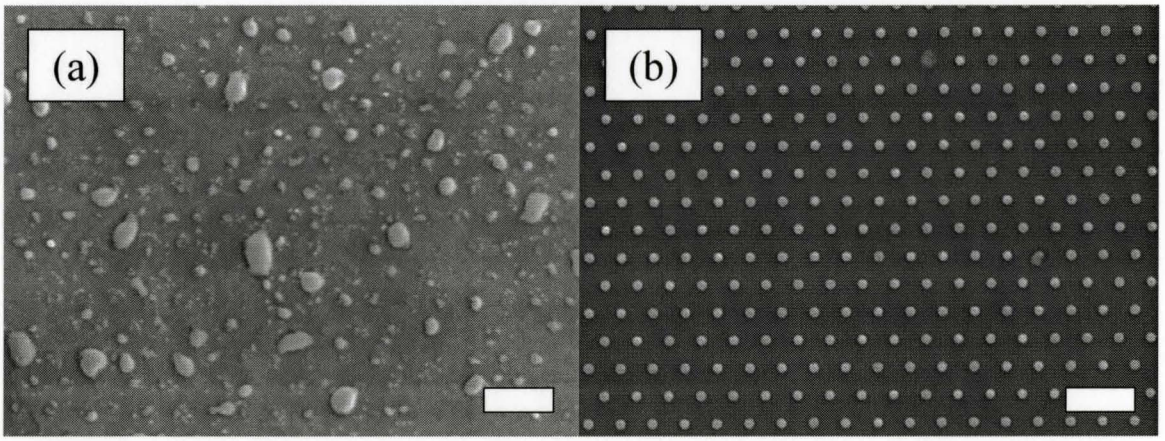

Figure 3.18. Top view SEM images of 15nm thick Au dots of 180 nm nominal diameter annealed at 550°C for 5 minutes. (a) 180nm dots without mesa support. (b) 180 nm dots with mesa support. The length bars indicate 1μm.

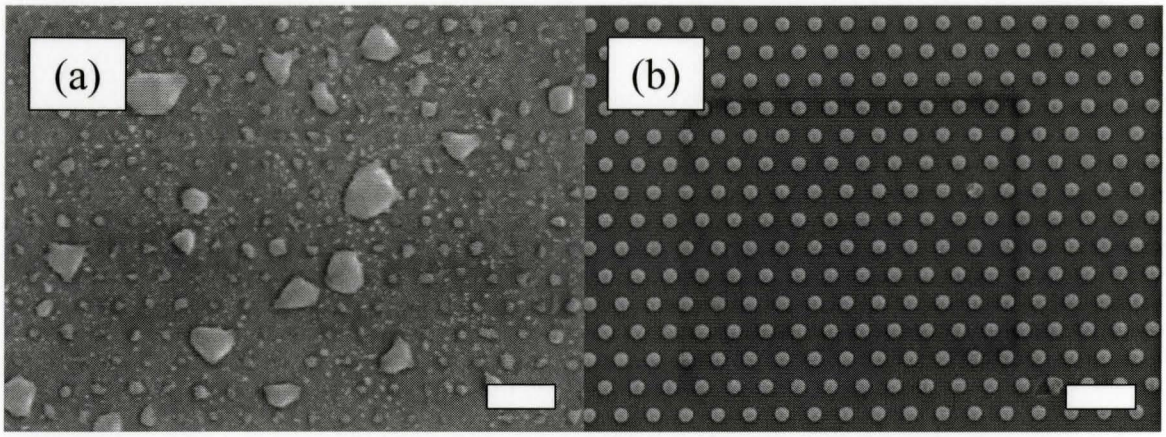

Figure 3.19. Top view SEM images of 15nm thick Au dots of 250nm nominal diameter annealed at 550°C for 5 minutes. (a) 250nm dots without mesa support. (b) 250nm dots with mesa support. The length bars indicate 1μm.

3.32 25nm Au Thickness Dot Structures

Images for 25nm Au thick structures are provided in Figures 3.20 to 3.23. The samples with mesa support revealed an increase in quality of the pattern with annealing as compared to the non-mesa supported samples. However, it is evident that the containment of the Au migration was not as effective in this case as compared to the 15nm thick Au samples presented in the previous section. When the Au thickness is too large, it appears that the Au "spills" over the mesa, which is particularly evident in Figure 3.22(b).

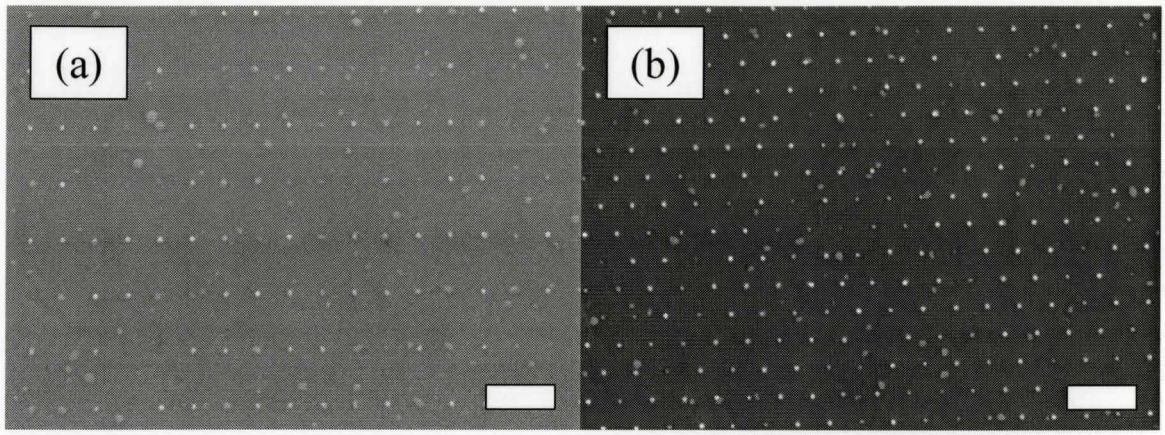

Figure 3.20. Top view SEM images of 25nm thick Au dots of 60 nm nominal diameter annealed at 550°C for 5 minutes. (a) 60nm dots without mesa support. Right) 60nm dots with mesa support. The length bars indicate 1μm.

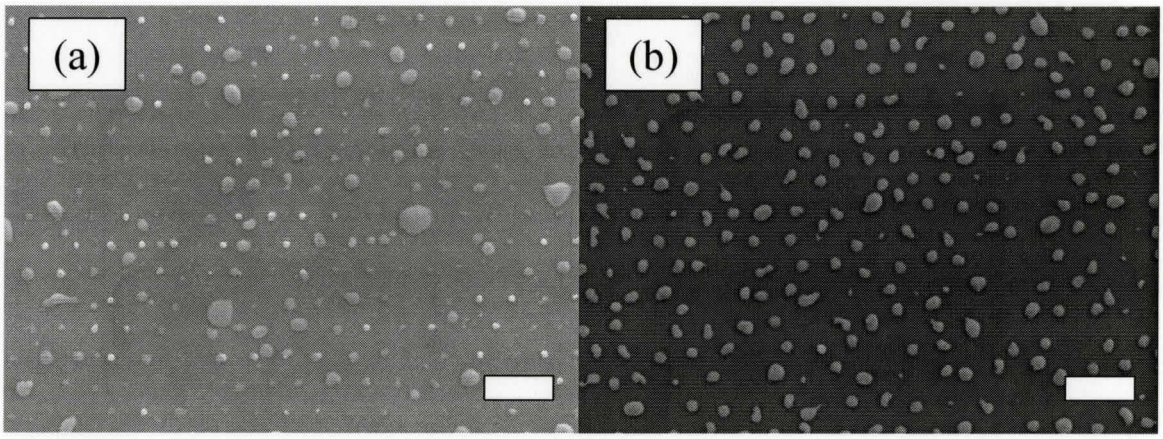

Figure 3.21. Top view SEM images of 25nm thick Au dots of 140 nm nominal diameter annealed at 550°C for 5 minutes. (a) 140nm dots without mesa support. (b) 140nm dots with mesa support. The length bars indicate 1μm.

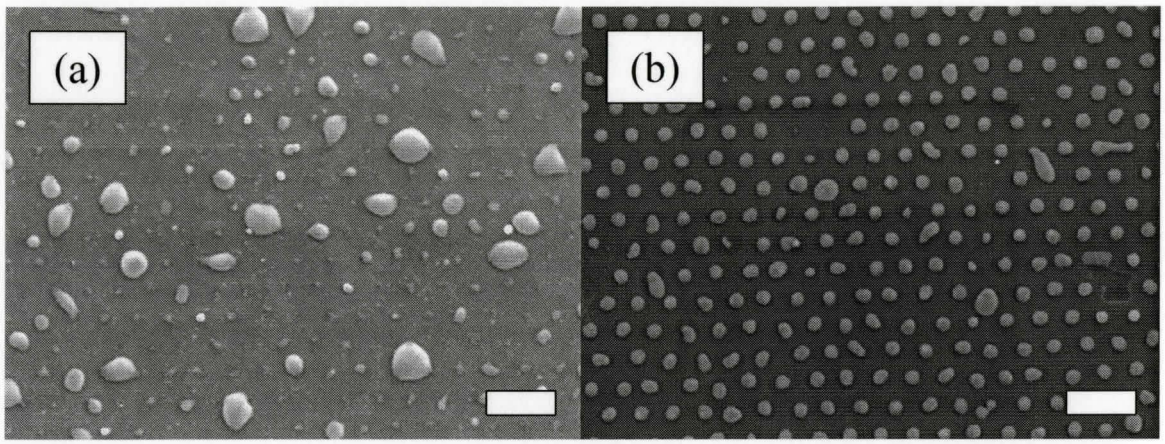

Figure 3.22. Top view SEM images of 25nm thick Au dots of 180nm nominal diameter annealed at 550°C for 5 minutes. (a) 180nm dots without mesa support. (b) 180nm dots with mesa support. The length bars indicate 1μm.

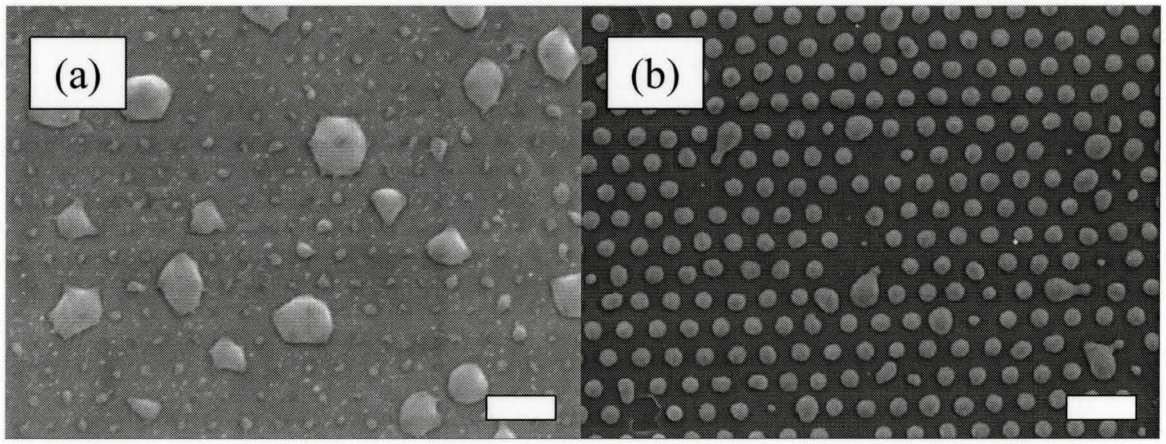

Figure 3.23. Top view SEM images of 25nm thick Au dots of 250nm nominal diameter annealed at 550°C for 5 minutes. (a) 250nm dots without mesa support. (b) 250nm dots with mesa support. The length bars indicate 1μm.

3.33 35nm Au Thickness Dot Structures

Structures of 35nm Au thickness were annealed in the same conditions as the previous samples, namely 550˚C for 5 minutes. Again, structures without mesa support were disrupted after annealing, while mesa-supported structures were improved, as

shown in Figures 3.24 to 3.28. Interestingly, it appears that the Au migrates along specific crystallographic directions. As can be seen in Figure 3.28(b), the formation of Au islands occurs in preferred directions. This is attributed to the sintering effect between the Au islands which spilled over the confines of the mesa. Once in a molten state on the surface, the forces driving the unification of the liquid Au-Ga particles were uninhibited. The resulting arrangements of Au in Figure 3.28(b) coincide very well with the results illustrated in an ideal case in Figure 3.7

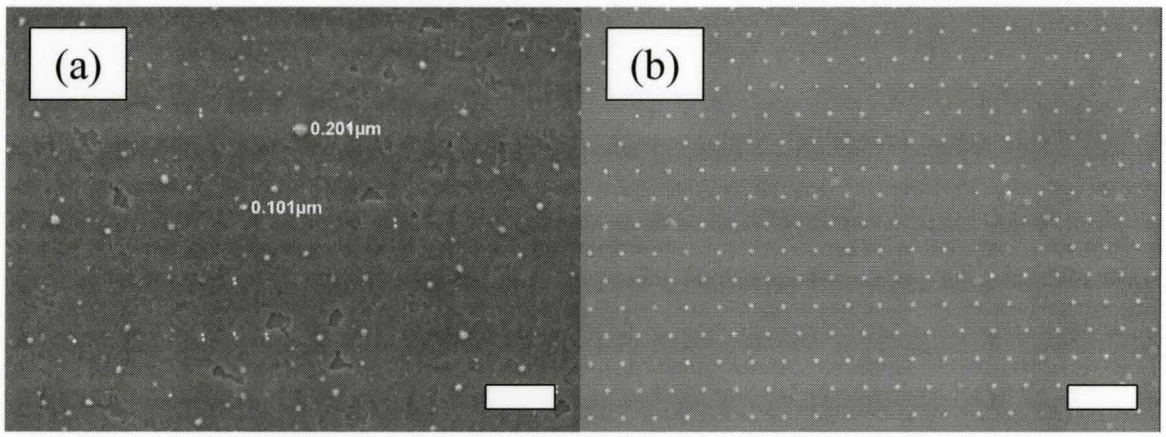

Figure 3.24. Top view SEM images of 35nm thick Au dots of 60nm nominal diameter annealed at 550°C for 5 minutes. (a) 60nm dots without mesa support. (b) 60nm dots with mesa support. The length bars indicate 1µm.

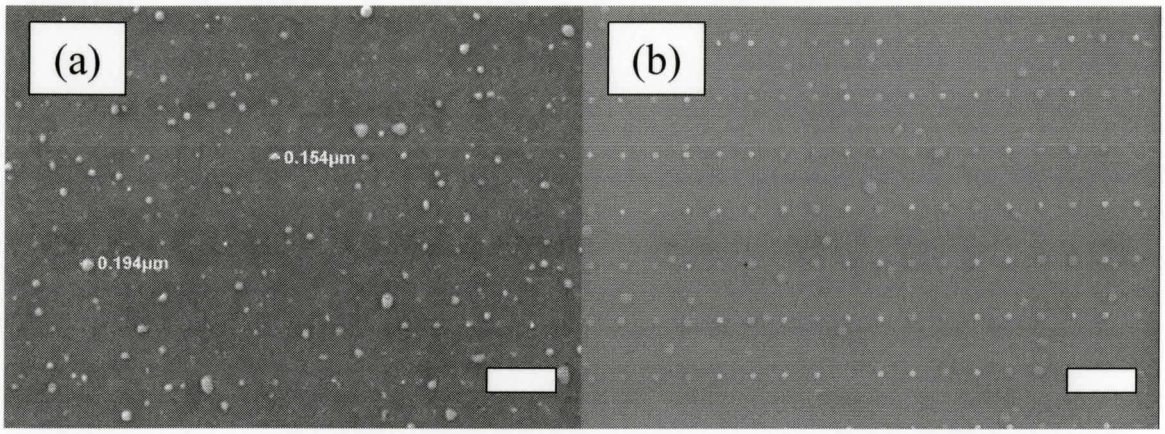

Figure 3.25. Top view SEM images of 35nm thick Au dots of 100nm nominal diameter annealed at 550°C for 5 minutes. (a) 100nm dots without mesa support. (b) 100nm dots with mesa support. The length bars indicate 1µm.

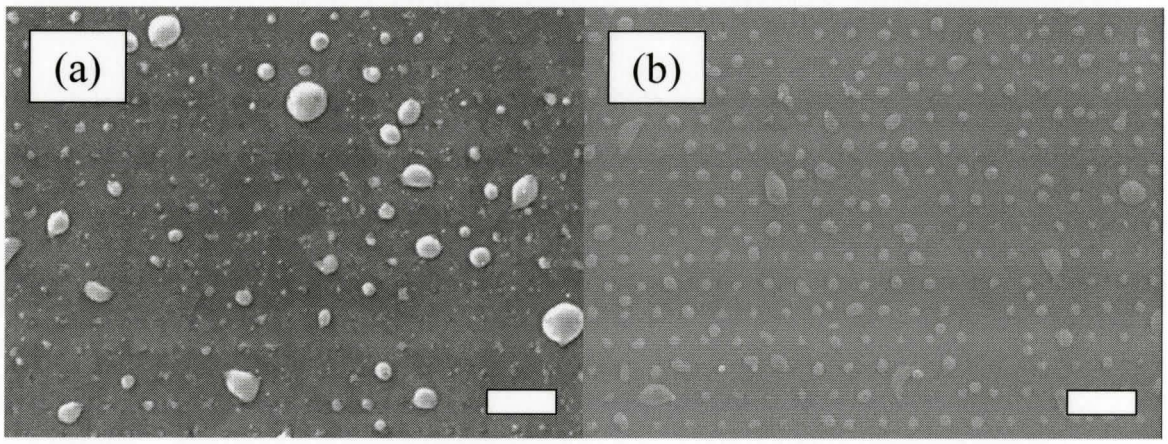

Figure 3.26. Top view SEM images of 35nm thick Au dots of 140nm nominal diameter annealed at 550°C for 5 minutes. (a) 140nm dots without mesa support. (b) 140nm dots with mesa support. The length bars indicate 1µm.

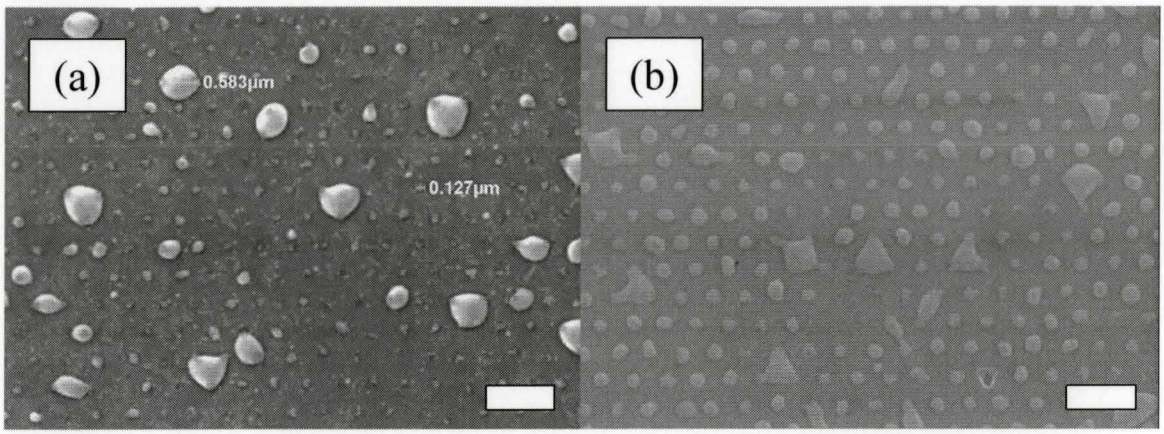

Figure 3.27. Top view SEM images of 35nm thick Au dots of 180nm nominal diameter annealed at 550°C for 5 minutes. (a) 180nm dots without mesa support. (b) 180nm dots with mesa support. The length bars indicate 1µm.

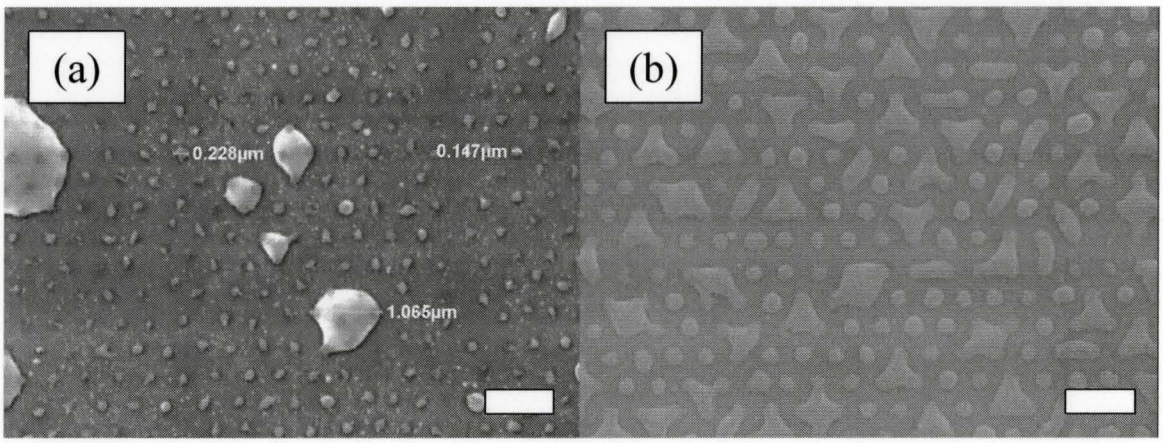

Figure 3.28. Top view SEM images of 35nm thick Au dots of 250nm nominal diameter annealed at 550°C for 5 minutes. (a) 250nm dots without mesa support. (b) 250nm dots with mesa support. The length bars indicate 1µm.

3.34 50nm Au Thickness Dot Structures

In all cases, the 50nm Au thickness appeared to be too large to be maintained by the mesas as illustrated in Figures 3.29 to 3.33

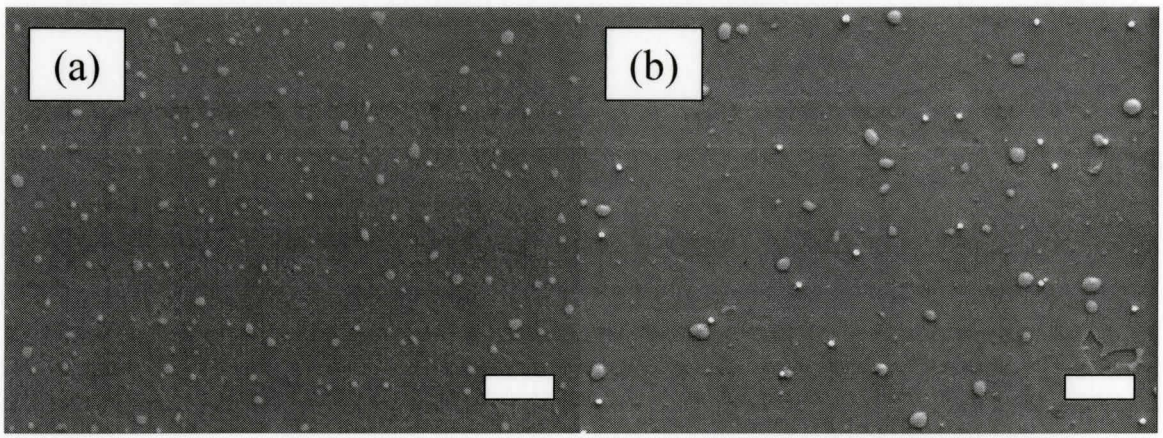

Figure 3.29. Top view SEM images of 50nm thick Au dots of 60nm nominal diameter annealed at 550°C for 5 minutes. (a) 60nm dots without mesa support. (b) 60nm dots with mesa support. The length bars indicate 1μm.

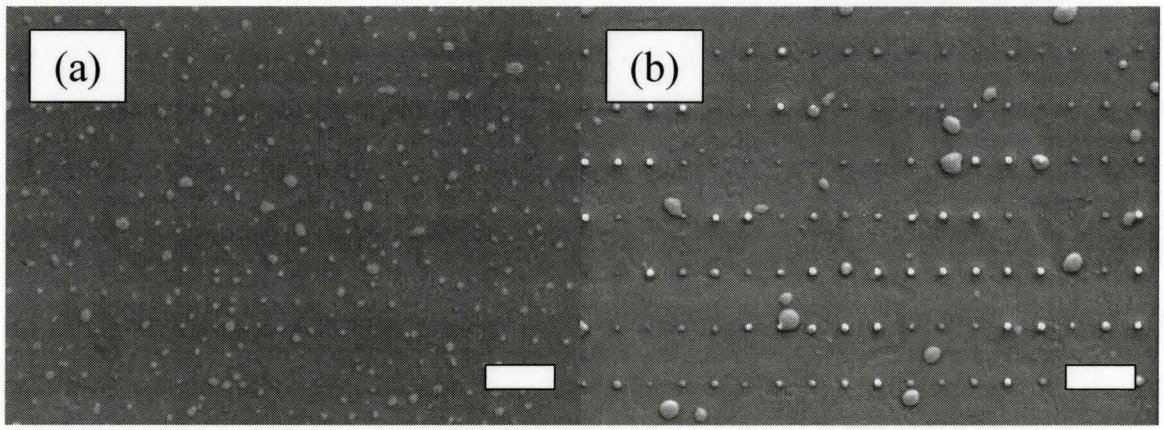

Figure 3.30. Top view SEM images of 50nm thick Au dots of 100nm nominal diameter annealed at 550°C for 5 minutes. (a) 100nm dots without mesa support. (b) 100nm dots with mesa support. The length bars indicate 1μm.

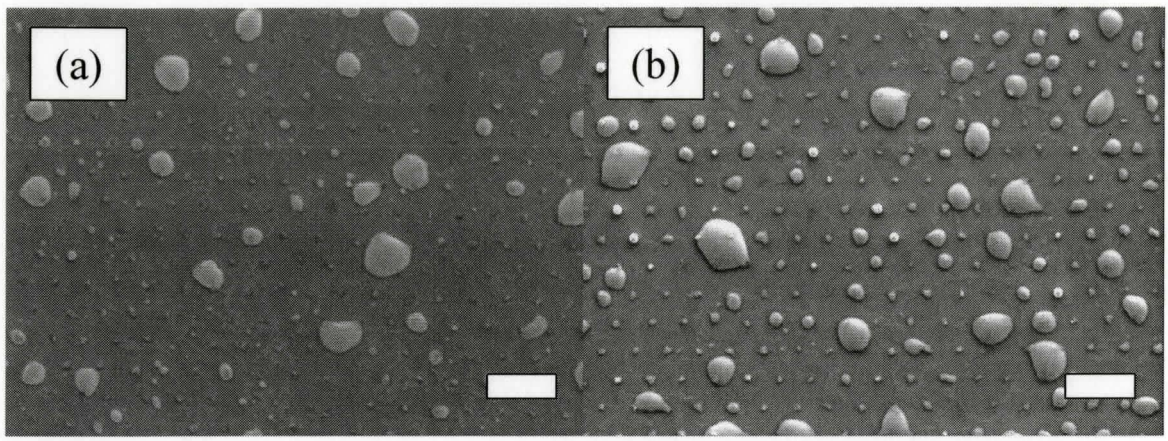

Figure 3.31. Top view SEM images of 50nm thick Au dots of 140nm nominal diameter annealed at 550°C for 5 minutes. (a) 140nm dots without mesa support. (b) 140nm dots with mesa support. The length bars indicate 1μm.

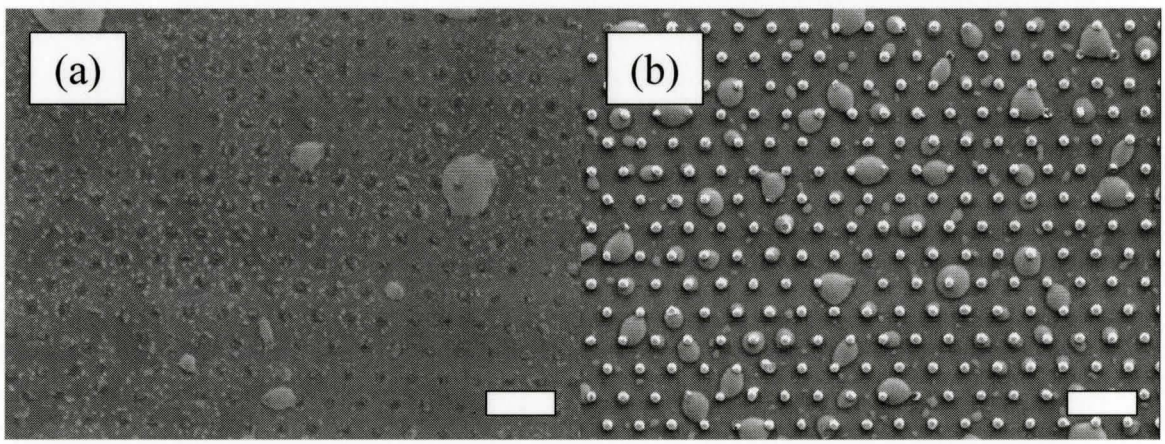

Figure 3.32. Top view SEM images of 50nm thick Au dots of 180nm nominal diameter annealed at 550°C for 5 minutes. (a) 180nm dots without mesa support. (b) 180nm dots with mesa support. The length bars indicate 1μm.

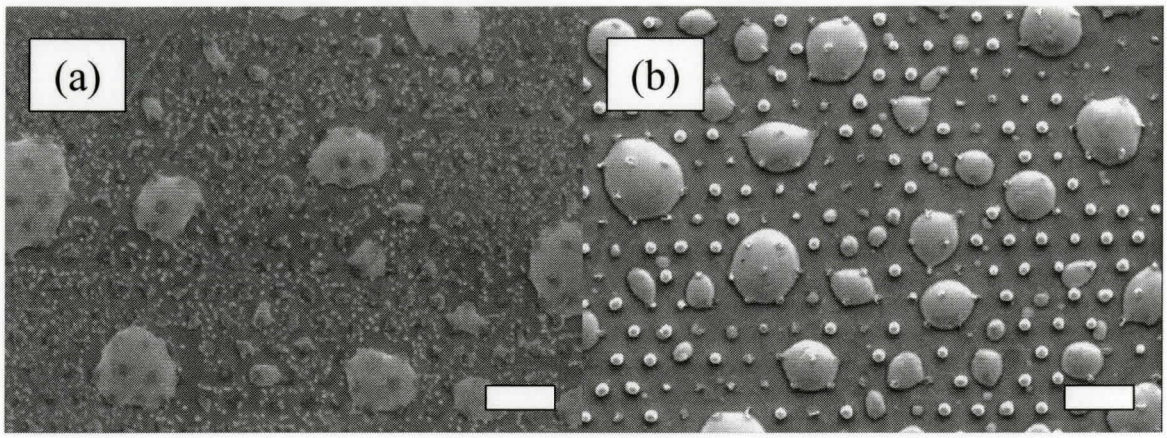

Figure 3.33. Top view SEM images of 50nm thick Au dots of 250nm nominal diameter annealed at 550°C for 5 minutes. (a) 250nm dots without mesa support. (b) 250nm dots with mesa support. The length bars indicate 1μm.

Close examination of the above results reveals that the best post-annealed patterns were obtained with 15 nm thick Au dots of 140, 180 and 250nm diameter, and the 25 nm thick Au dot of 250nm diameter. We note that for these particular samples the calculated change in diameter upon annealing was within 15% of the initial EBL-prescribed diameter as defined in Table 3.2. Conversely, the other samples underwent a change in diameter of 25% or larger, which evidently could not be contained by the mesa.

3.4 Mesa Assisted Annealing vs. Non-mesa Assisted Annealing (Lines)

In this section, a similar comparison is made between the effects of annealing line structures as was performed for the dots structures in section 3.3 Left-hand figures shown below demonstrate typical results annealed without mesa support while right-hand images show samples annealed with mesa support.

3.41 15nm Au Thickness Line Structures

In all cases of annealing (both with and without mesa support), the integrity of the original line structure was compromised. However, annealing with mesa support generally allowed the line structures to retain their initial structure more readily Figures 3.34 to 3.39 illustrate the results of annealing the structures of 15nm Au thickness. In particular, Figure 3.39 contrasts very clearly the varying quality of the results of annealing structures with and without mesa support.

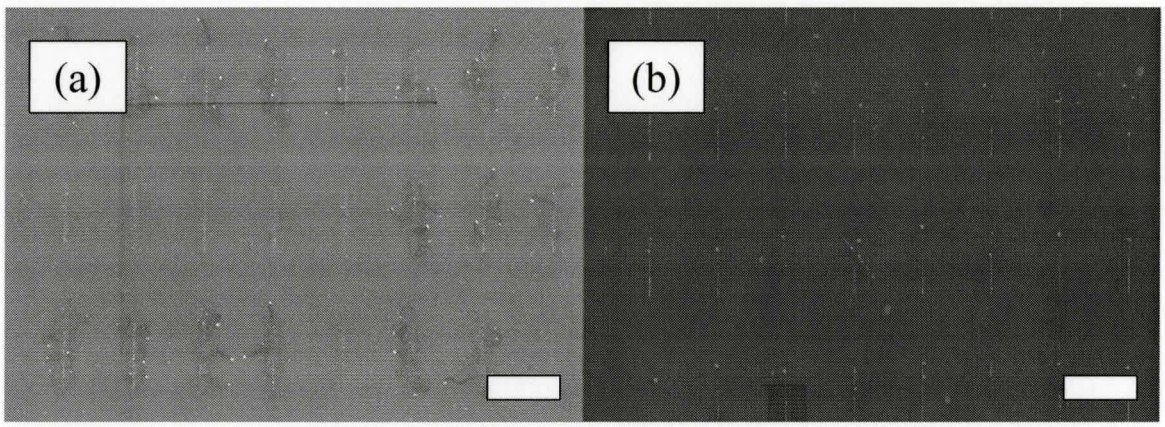

Figure 3.34. Top view SEM images of 15nm thick Au lines of 60nm nominal linewidth annealed at 550°C for 5 minutes. (a) 60nm lines without mesa support. (b) 60nm lines with mesa support. The length bars indicate 10μm.

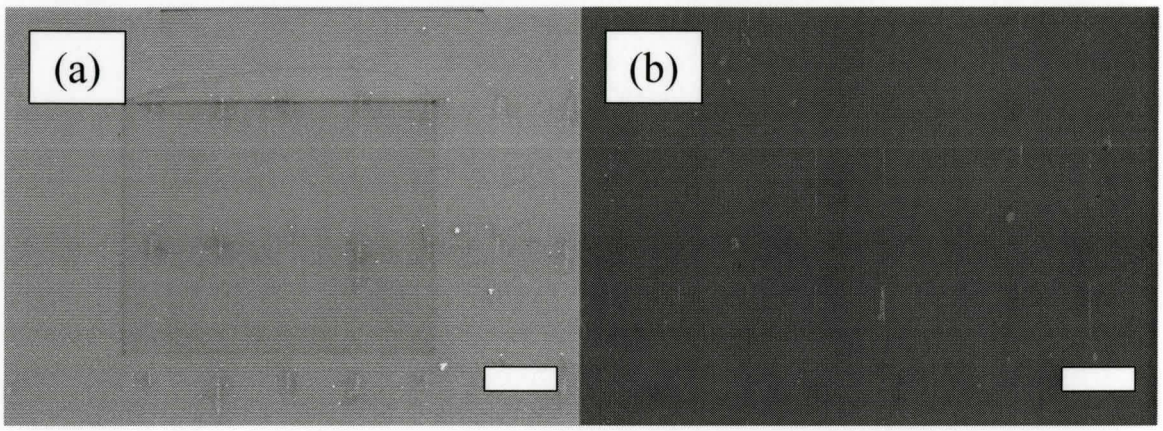

Figure 3.35. Top view SEM images of 15nm thick Au lines of 90nm nominal linewidth annealed at 550°C for 5 minutes. (a) 90nm lines without mesa support. (b) 90nm lines with mesa support. The length bars indicate 10μm.

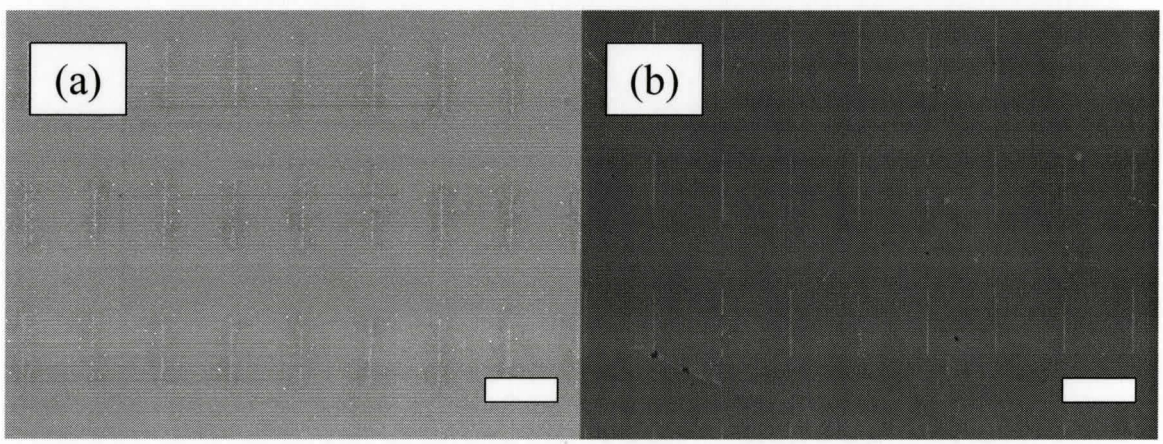

Figure 3.36. Top view SEM images of 15nm thick Au lines of 120nm nominal linewidth annealed at 550°C for 5 minutes. (a) 120nm lines without mesa support. (b) 120nm lines with mesa support. The length bars indicate 10μm.

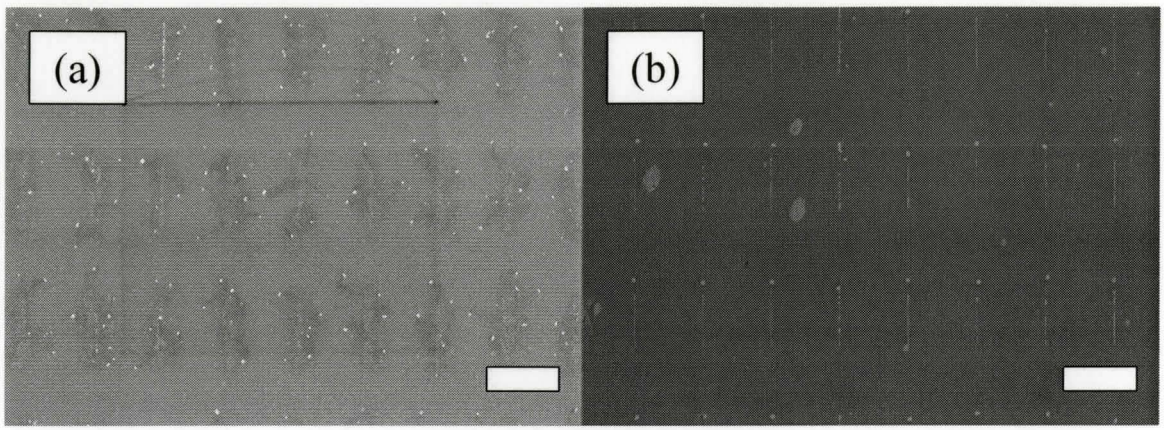

Figure 3.37. Top view SEM images of 15nm thick Au lines of 150nm nominal linewidth annealed at 550°C for 5 minutes. (a) 150nm lines without mesa support. (b) 150nm lines with mesa support. The length bars indicate 10μm.

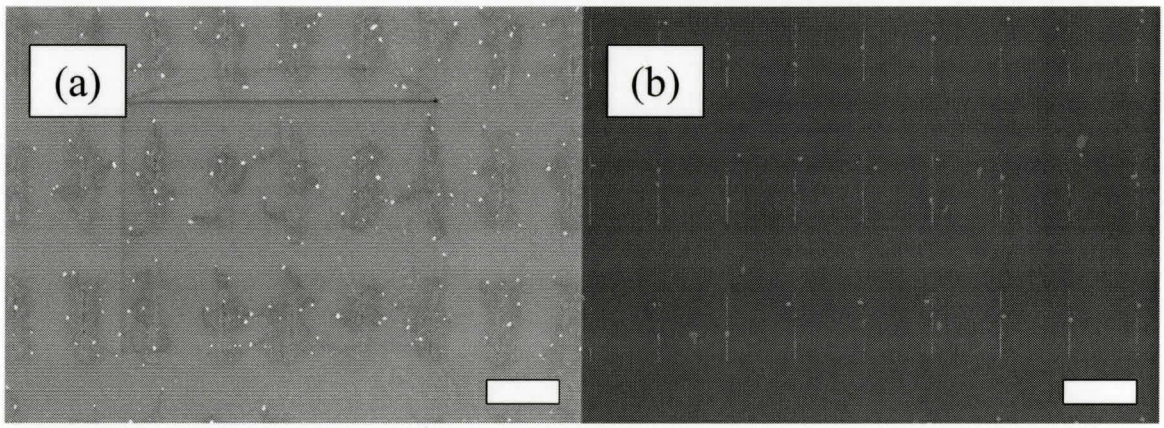

Figure 3.38. Top view SEM images of 15nm thick Au lines of 200nm nominal linewidth annealed at 550°C for 5 minutes. (a) 200nm lines without mesa support. (b) 200nm lines with mesa support. The length bars indicate 10μm.

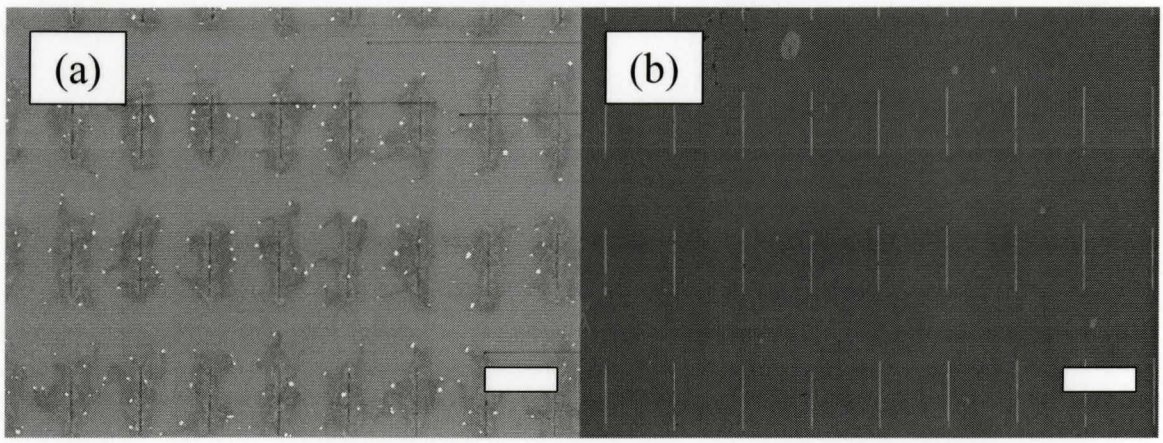

Figure 3.39. Top view SEM images of 15nm thick Au lines of 300nm nominal linewidth annealed at 550°C for 5 minutes. (a) 300nm lines without mesa support. (b) 300nm lines with mesa support. The length bars indicate 10μm.

3.42 25nm Au Thickness Line Structures

Figures 3.40 to 3.43 illustrate the results of annealing the structures of 25nm Au thickness. As can be seen through the progression of figures, the quality of the array is better maintained as the linewidth of the structures increases.

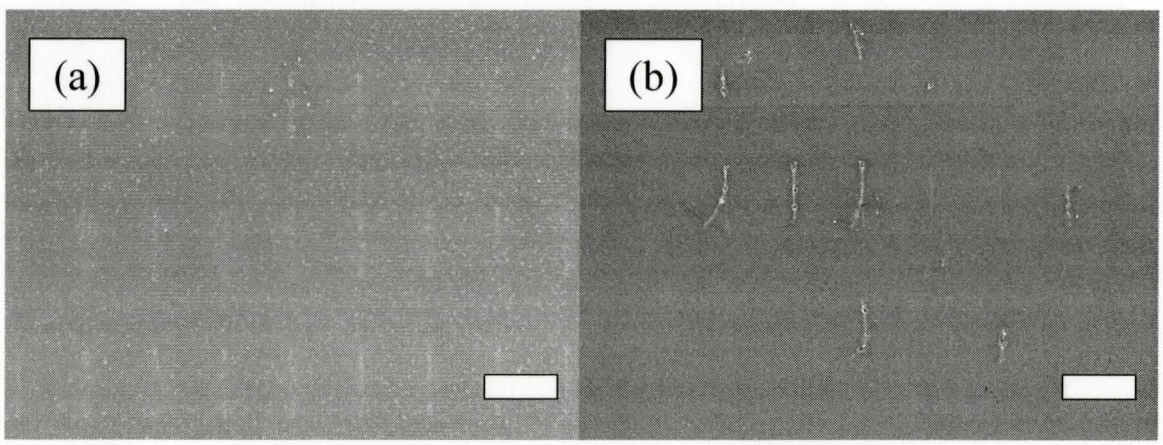

Figure 3.40. Top view SEM images of 25nm thick Au lines of 120nm nominal linewidth annealed at 550°C for 5 minutes. (a) 120nm lines without mesa support. (b) 120nm lines with mesa support. The length bars indicate 10μm.

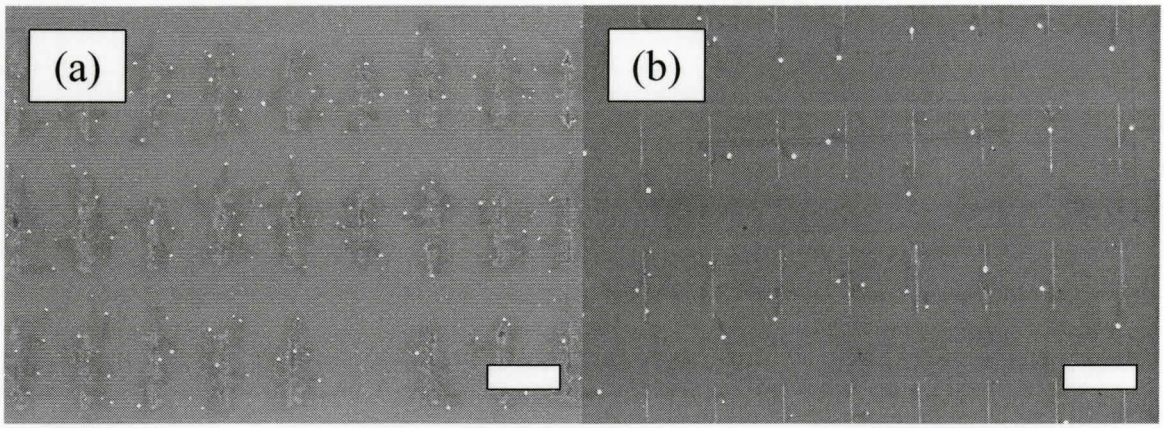

Figure 3.41. Top view SEM images of 25nm thick Au lines of 150nm nominal linewidth annealed at 550°C for 5 minutes. (a) 150nm lines without mesa support. (b) 150nm lines with mesa support. The length bars indicate 10μm.

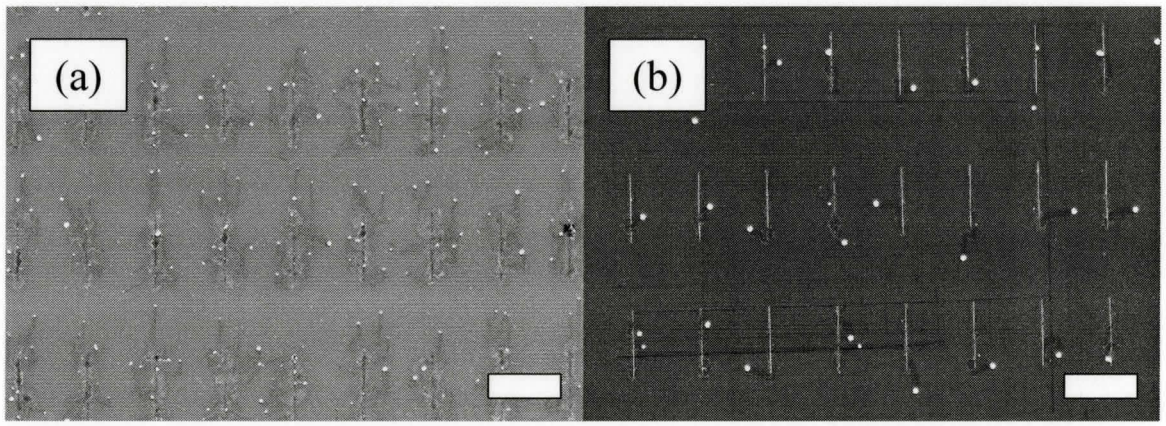

Figure 3.42. Top view SEM images of 25nm thick Au lines of 200nm nominal linewidth annealed at 550°C for 5 minutes. (a) 200nm lines without mesa support. (b) 200nm lines with mesa support. The length bars indicate 10μm.

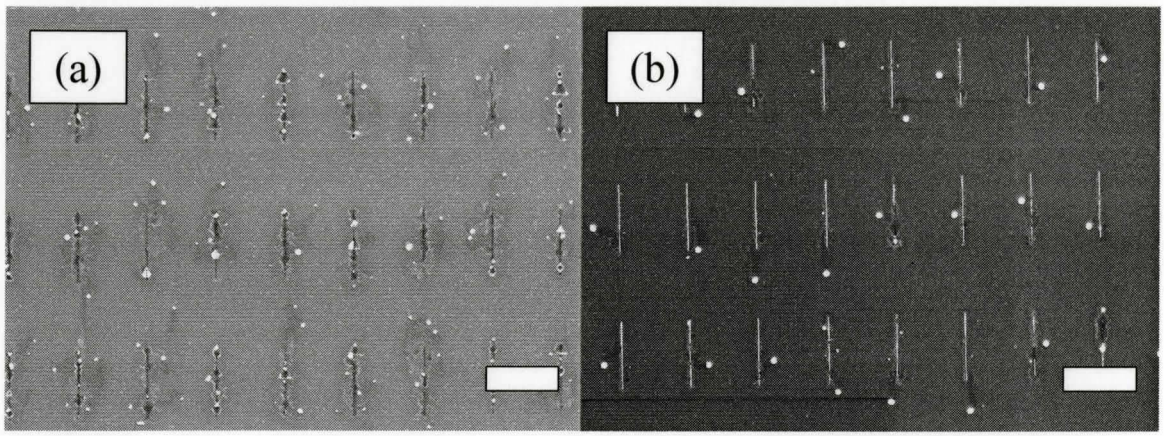

Figure 3.43. Top view SEM images of 25nm thick Au lines of 300nm nominal linewidth annealed at 550°C for 5 minutes. (a) 300nm lines without mesa support. (b) 300nm lines with mesa support. The length bars indicate 10μm.

3.43 35nm Au Thickness Line Structures

Figures 3.44 to 3.48 display the results of annealing line structures of 35nm Au thickness.

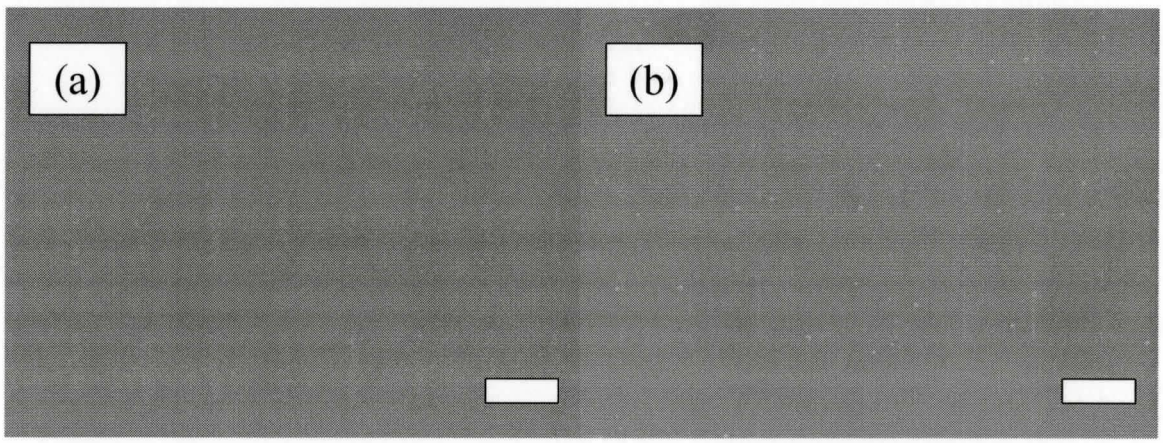

Figure 3.44. Top view SEM images of 35nm thick Au lines of 60nm nominal linewidth annealed at 550°C for 5 minutes. (a) 60nm lines without mesa support. (b) 60nm lines with mesa support. The length bars indicate 10μm.

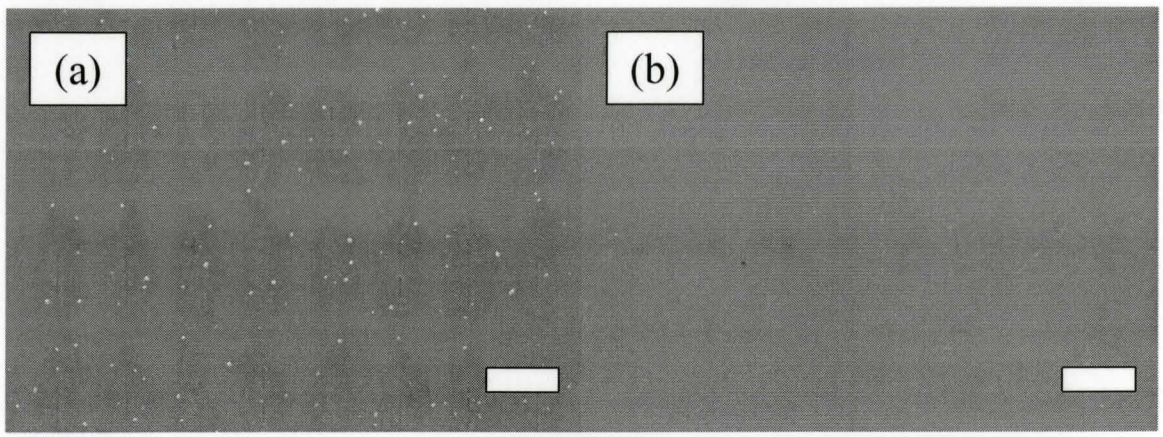

Figure 3.45. Top view SEM images of 35nm thick Au lines of 120nm nominal linewidth annealed at 550°C for 5 minutes. (a) 120nm lines without mesa support. (b) 120nm lines with mesa support. The length bars indicate 10μm.

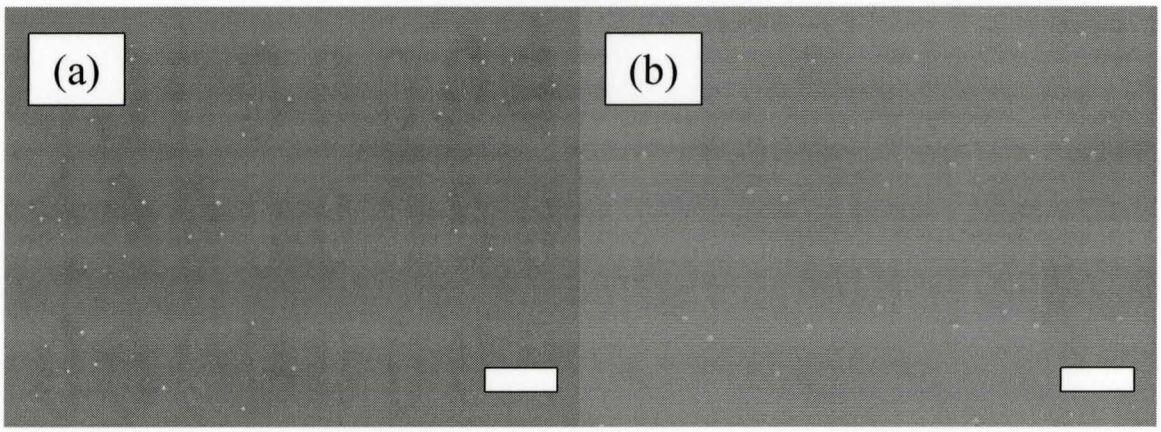

Figure 3.46. Top view SEM images of 35nm thick Au lines of 150nm nominal linewidth annealed at 550°C for 5 minutes. (a) 150nm lines without mesa support. (b) 150nm lines with mesa support. The length bars indicate 10μm.

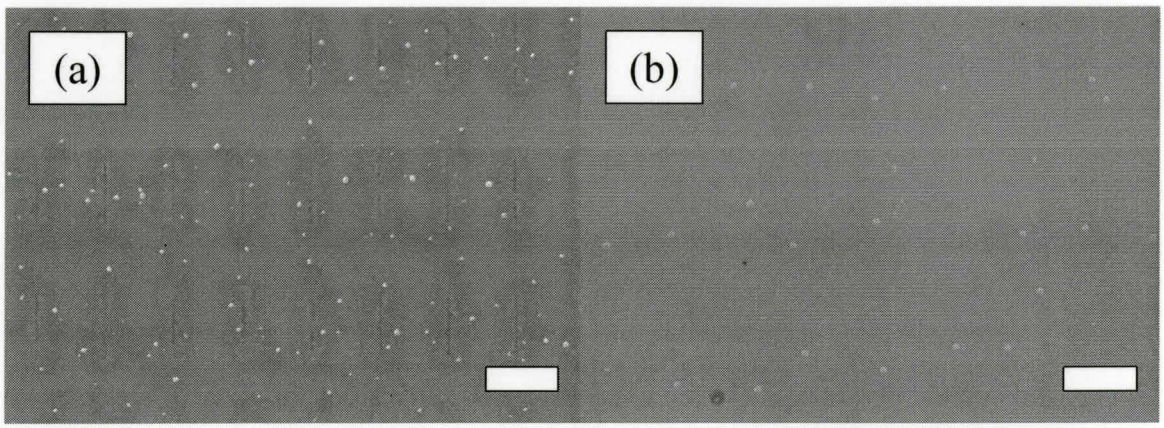

Figure 3.47. Top view SEM images of 35nm thick Au lines of 200nm nominal linewidth annealed at 550°C for 5 minutes. (a) 200nm lines without mesa support. (b) 200nm lines with mesa support. The length bars indicate 10μm.

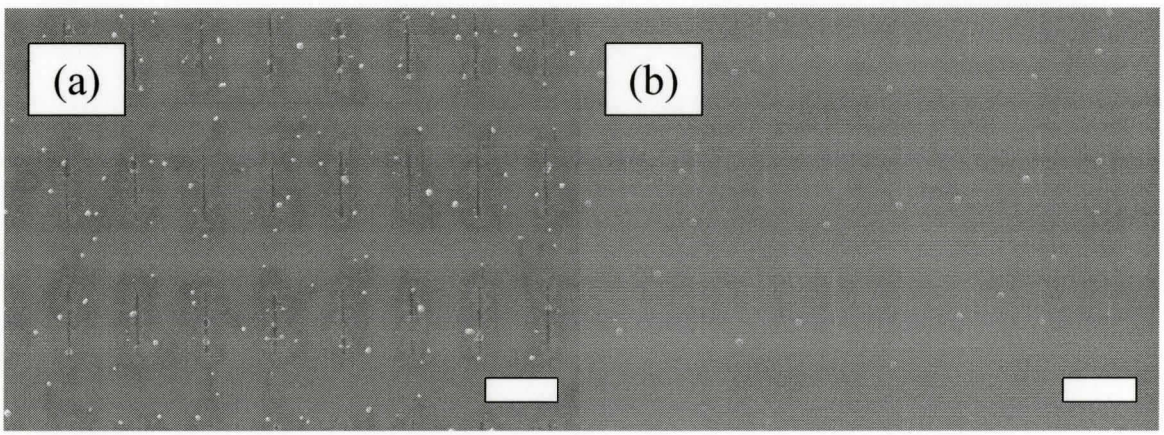

Figure 3.48. Top view SEM images of 35nm thick Au lines of 300nm nominal linewidth annealed at 550°C for 5 minutes. (a) 300nm lines without mesa support. (b) 300nm lines with mesa support. The length bars indicate 10μm.

3.44 50nm Au Thickness Line Structures

Figures 3.49 to 3.53 illustrate the results of annealing the structures of 50nm Au thickness. Of note are the 120nm line structures which could not be recovered in Figure 3.50(b). Only a subtle outline of the structures remained.

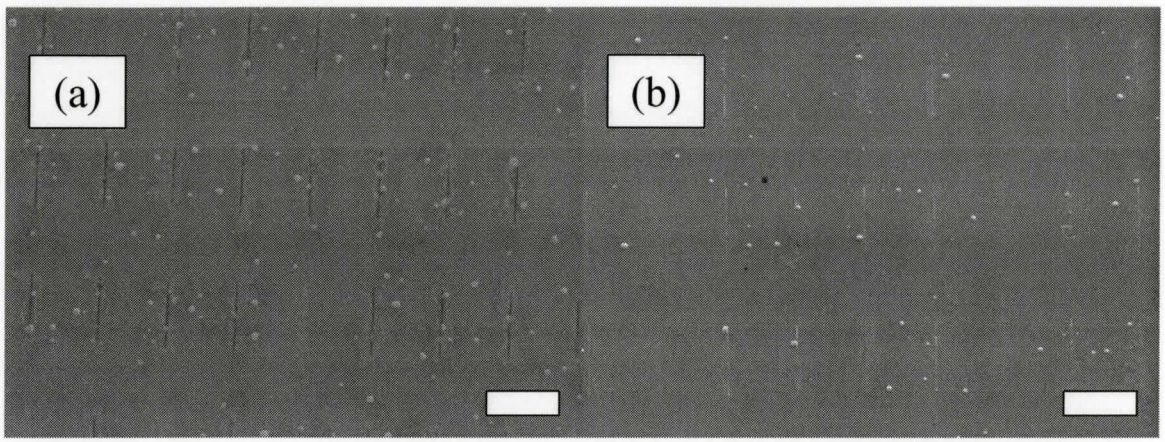

Figure 3.49. Top view SEM images of 50nm thick Au lines of 60nm nominal linewidth annealed at 550°C for 5 minutes. (a) 60nm lines without mesa support. (b) 60nm lines with mesa support. The length bars indicate 10μm.

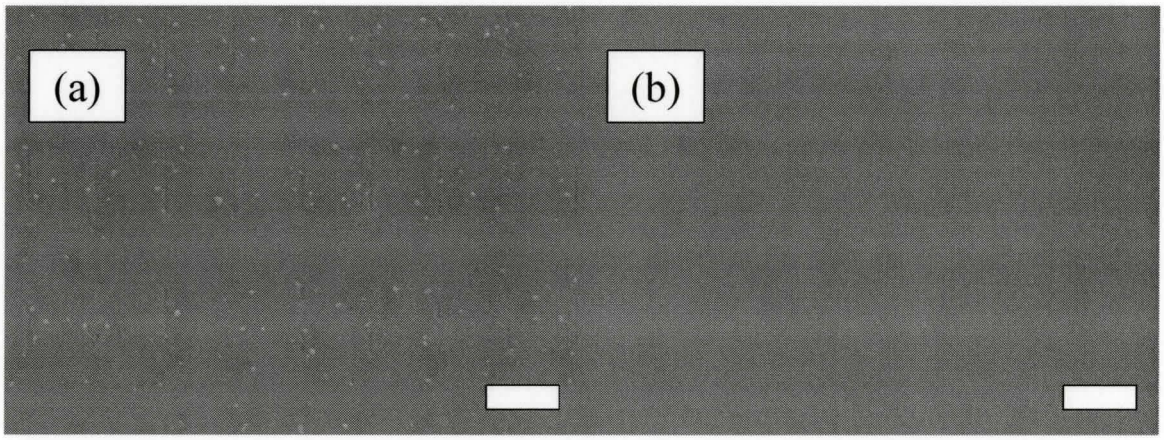

Figure 3.50. Top view SEM images of 50nm thick Au lines of 120nm nominal linewidth annealed at 550°C for 5 minutes. (a) 120nm lines without mesa support. (b) 120nm lines with mesa support. The length bars indicate 10μm.

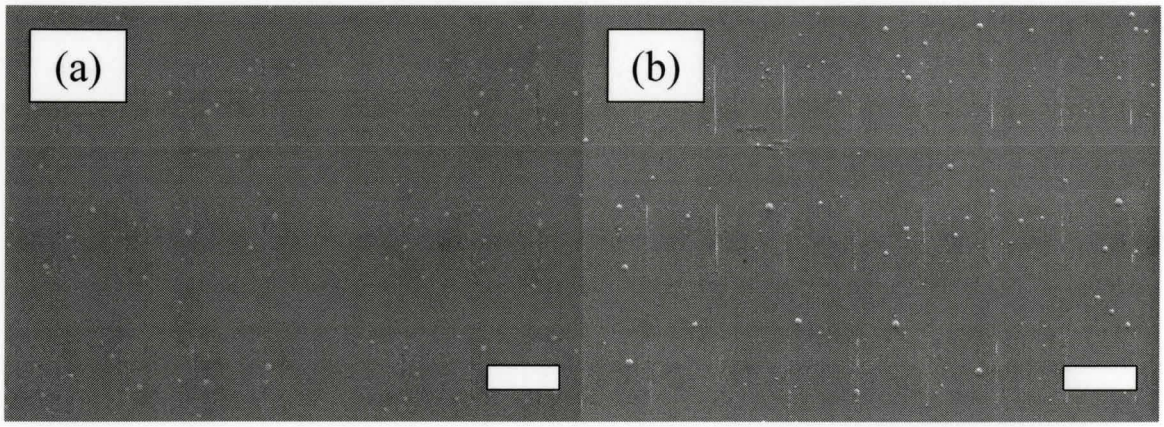

Figure 3.51. Top view SEM images of 50nm thick Au lines of 150nm nominal linewidth annealed at 550°C for 5 minutes. (a) 150nm lines without mesa support. (b) 150nm lines with mesa support. The length bars indicate 10μm.

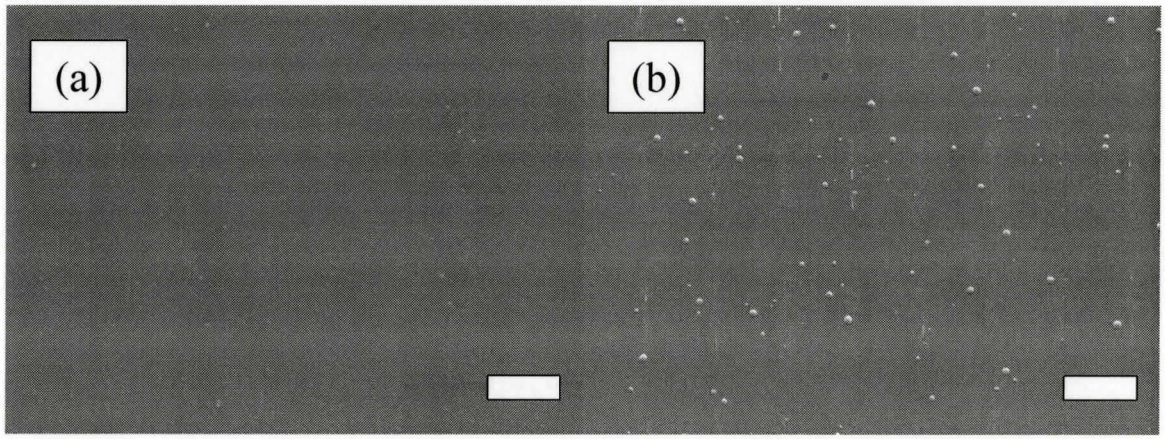

Figure 3.52. Top view SEM images of 50nm thick Au lines of 200nm nominal linewidth annealed at 550°C for 5 minutes. (a) 200nm lines without mesa support. (b) 200nm lines with mesa support. The length bars indicate 10μm.

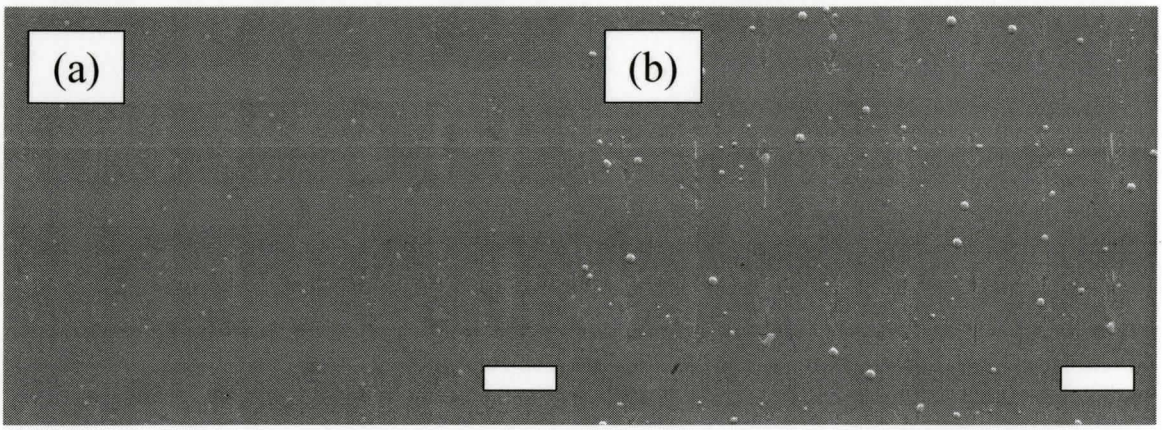

Figure 3.53. Top view SEM images of 50nm thick Au lines of 300nm nominal linewidth annealed at 550°C for 5 minutes. (a) 300nm lines without mesa support. (b) 300nm lines with mesa support. The length bars indicate 10μm.

Similar to the results presented in section 3.3 for the dots, it would appear that the mesa is most effective for lines with Au thickness of 15nm and widths of 120 to 300 nm range.

3.5 Mesa Assisted Annealing vs. Mesa Assisted Growth (Dots)

After the annealing experiments, the 4 samples with mesa support were then indium-mounted on an *n*-type GaAs wafer to be grown by gas source molecular beam epitaxy (GS-MBE). To mount the samples, In was melted on a hot plate at 300°C where it can be smeared on the bottom of the sample that is to be grown. The sample is then placed on a wafer and is then gently slid across the surface until the sample adheres to the supporting wafer via the tension provided by the liquid In. For GS-MBE Group III species (Ga) are supplied to the substrate from a solid elemental effusion source and the group V species (As) are supplied as dimers (As_2) from a hydride (AsH_3) gas cracker

operating at 950°C. A 15 minute degas process at 300°C was followed by oxide desorption at 550°C with hydrogen inductively coupled (ICP) plasma and an overpressure of As_2 at a rate of 3 standard cubic centimeters per minute. NW growth was initiated by opening the shutter of the Ga effusion cell. The cell is heated to provide a nominal growth rate of 1μm/hr at a V/III ratio of 2 to 1. After 15 minutes, the Ga cell was shuttered, to terminate the growth. The sample was cooled with remaining As_2 overpressure. After NW growth, the samples were again imaged via SEM. The results are presented separately below for the dots and lines of different thickness.

3.51 15nm Au Thickness Dot Structures

The SEM images in Figures 3.54 to 3.58 compare the post-annealed mesa-supported Au patterns with the identical samples after NW growth. While the pre-growth images show mildly disrupted Au patterns (as discussed previously), the post-growth images show that the location of NW growth is weakly correlated to the Au dot locations. Some pattern is observed in Figure 3.55(b). In general, however, it is evident as in Figures 3.57 and 3.58 that a patterned array of NW posts exists that are obscured amongst the growth of many smaller diameter wires. To verify this supposition, a micromanipulator in the SEM was used to remove the smaller diameter NWs surrounding a region of the periodic posts. Figure 3.59 shows a tilted-view SEM image after a micromanipulator had cleared the taller, thinner wires around the posts.

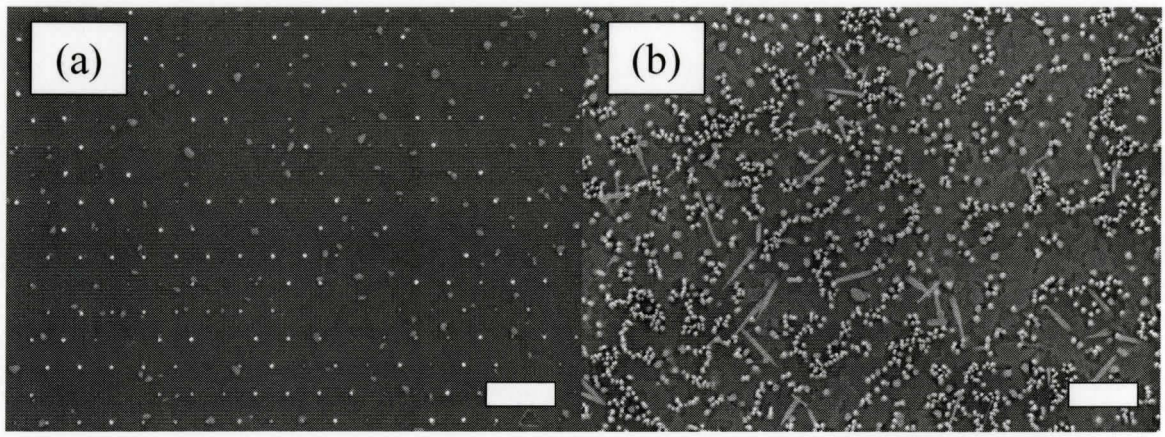

Figure 3.54. Top view SEM images comparing samples before and after NW growth for 15nm thick and 60nm diameter Au dots. (a) 60nm dots with mesa support annealed at 550°C for 5 minutes. (b) NWs grown from the sample shown in (a). The length bars indicate 1μm.

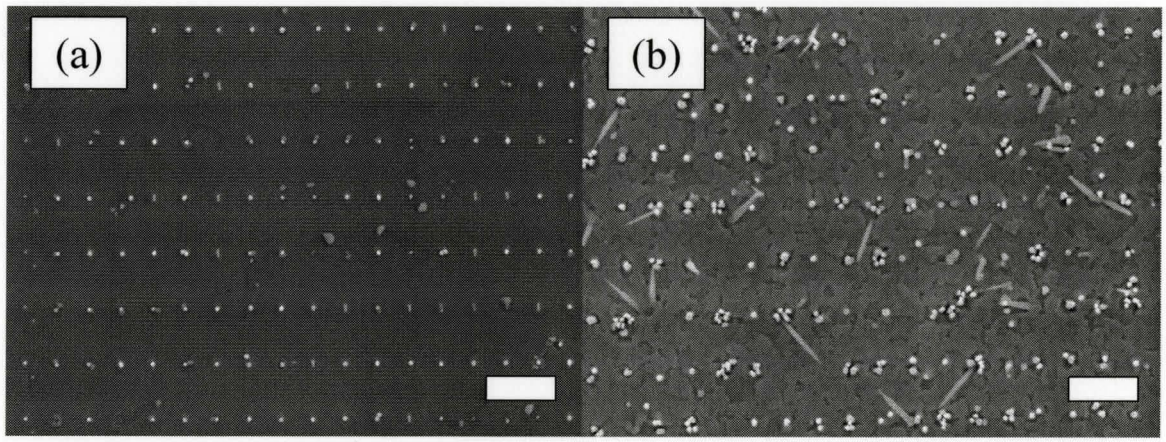

Figure 3.55. Top view SEM images comparing samples before and after NW growth for 15nm thick and 100nm diameter Au dots. (a) 100nm dots with mesa support annealed at 550°C for 5 minutes. (b) NWs grown from the sample shown in (a). The length bars indicate 1μm.

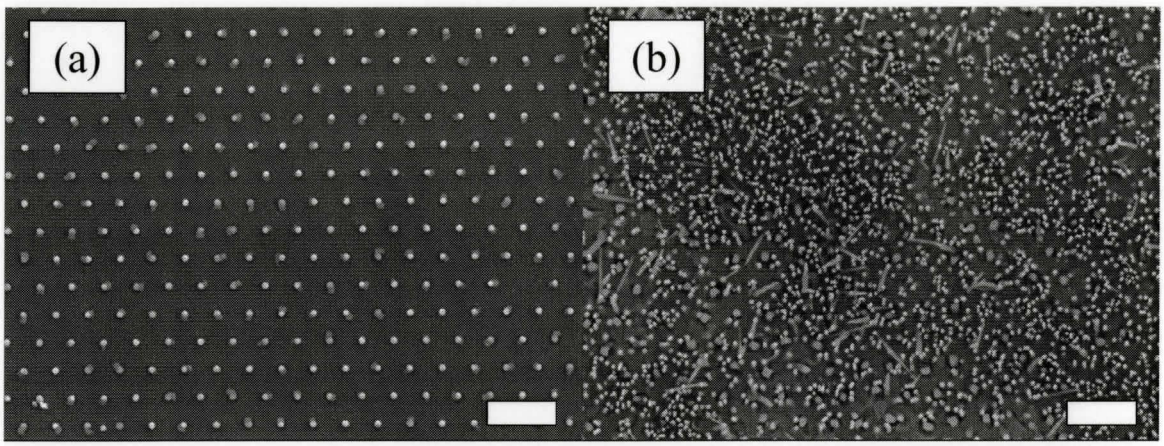

Figure 3.56. Top view SEM images comparing samples before and after NW growth for 15nm thick and 140nm diameter Au dots. (a) 140nm dots with mesa support annealed at 550°C for 5 minutes. (b) NWs grown from the sample shown in (a). The length bars indicate 1μm.

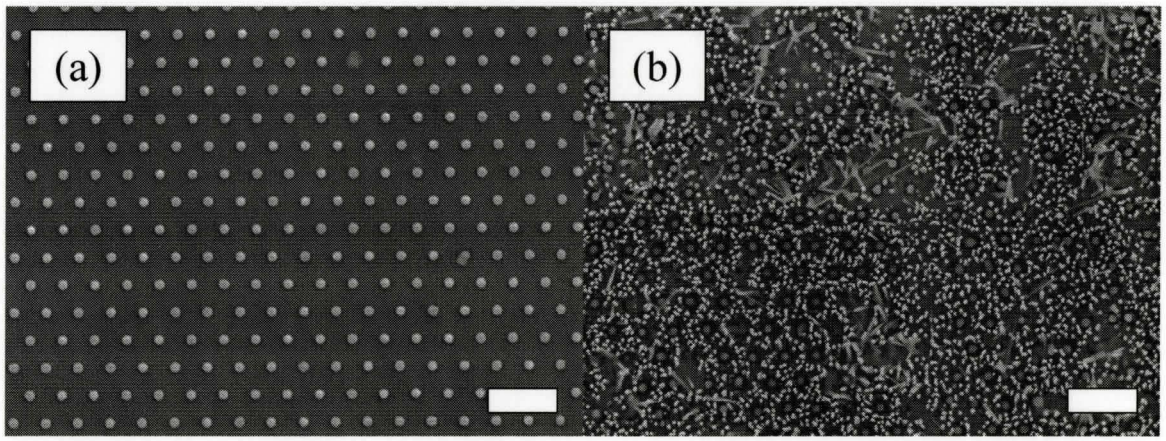

Figure 3.57. Top view SEM images comparing samples before and after NW growth for 15nm thick and 180nm diameter Au dots. (a) 180nm dots with mesa support annealed at 550°C for 5 minutes. (b) NWs grown from the sample shown in (a). The length bars indicate 1μm.

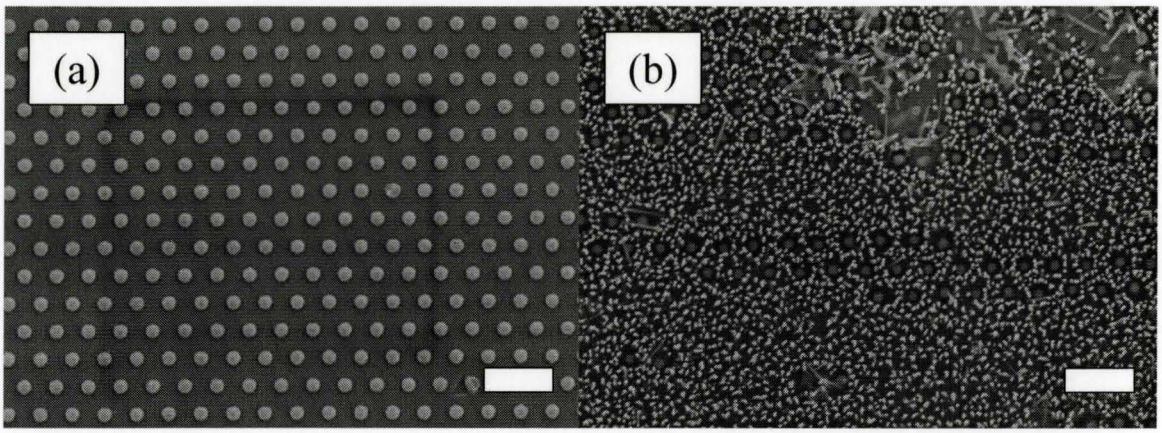

Figure 3.58. Top view SEM images comparing samples before and after NW growth for 15nm thick and 250nm diameter Au dots. (a) 250nm dots with mesa support annealed at 550°C for 5 minutes. (b) NWs grown from the sample shown in (a). The length bars indicate 1μm.

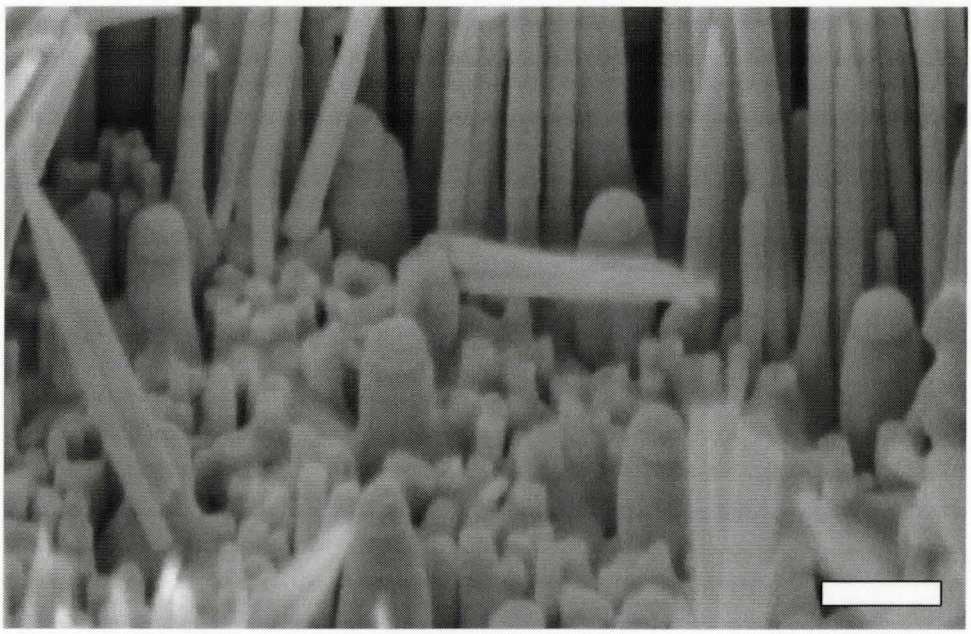

Figure 3.59. 60° Tilted SEM view of 180nm dots after a micromanipulator removed the surrounding wires. The length bar indicates 200nm.

3.52 25nm Au Thickness Dot Structures

Similar results were obtained in Figures 3.60 to 3.63 for the 25nm thick Au dots.

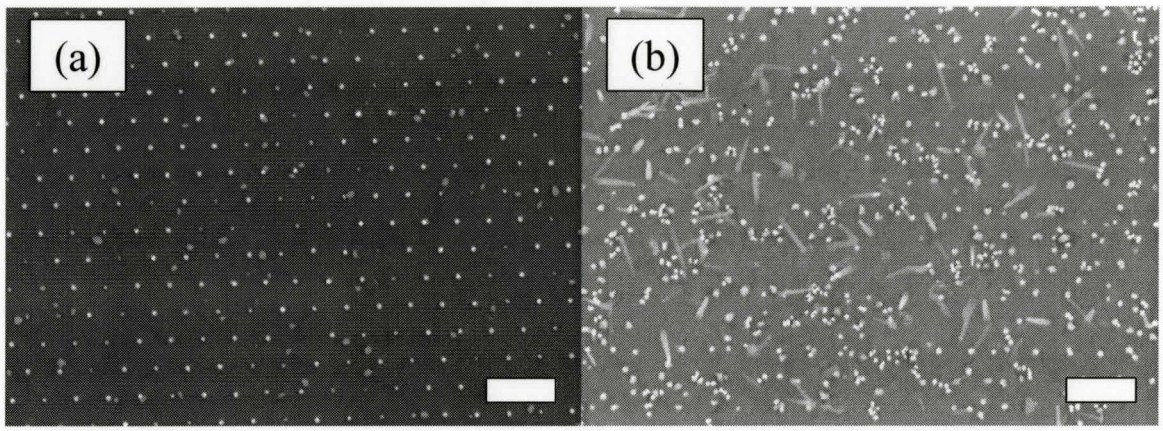

Figure 3.60. Top view SEM images comparing samples before and after NW growth for 25nm thick and 60nm diameter Au dots. (a) 60nm dots with mesa support annealed at 550°C for 5 minutes. (b) NWs grown from the sample shown in (a). The length bars indicate 1μm.

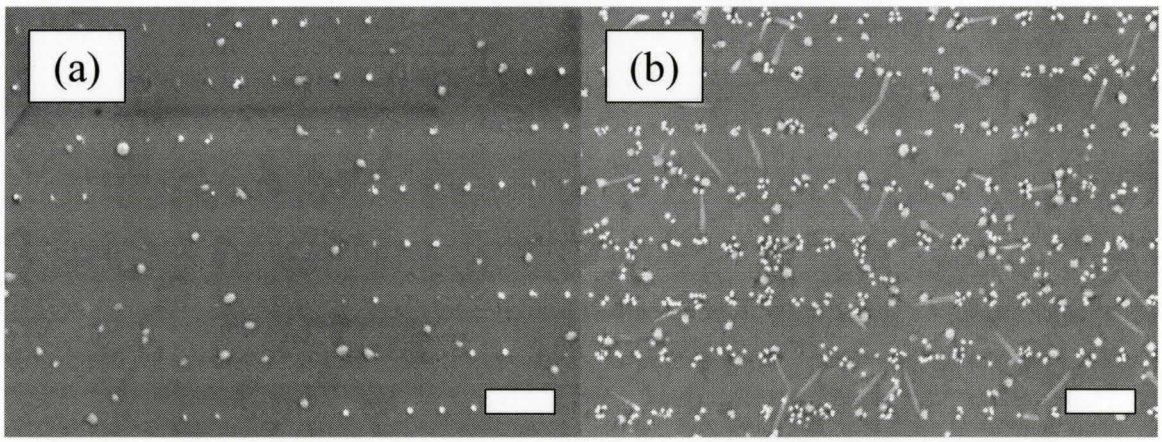

Figure 3.61. Top view SEM images comparing samples before and after NW growth for 25nm thick and 140nm diameter Au dots. (a) 140nm dots with mesa support annealed at 550°C for 5 minutes. (b) NWs grown from the sample shown in (a). The length bars indicate 1μm.

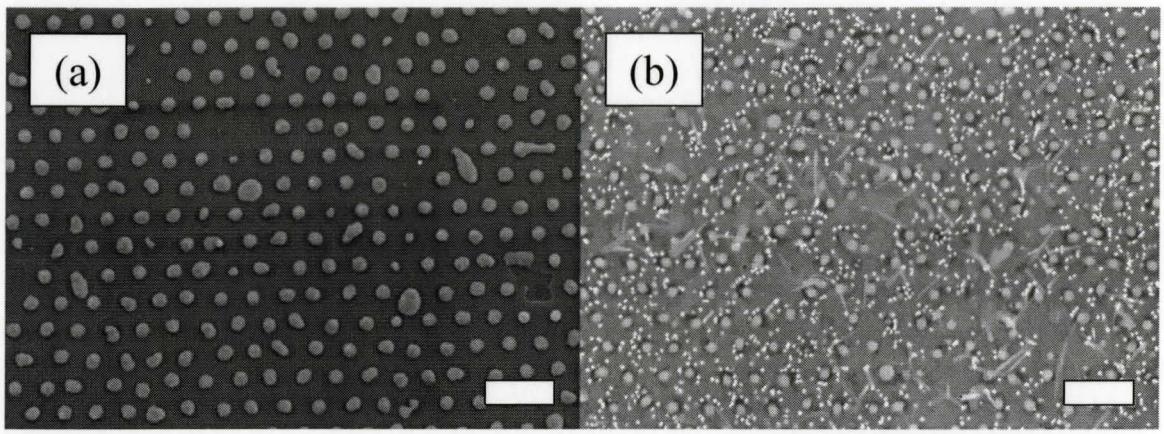

Figure 3.62. Top view SEM images comparing samples before and after NW growth for 25nm thick and 180nm diameter Au dots. (a) 180nm dots with mesa support annealed at 550°C for 5 minutes. (b) NWs grown from the sample shown in (a). The length bars indicate 1μm.

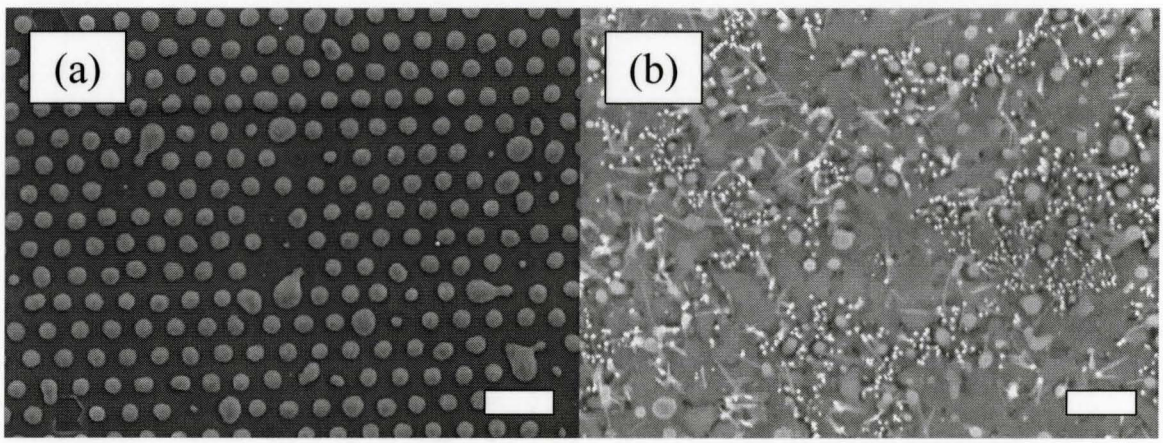

Figure 3.63. Top view SEM images comparing samples before and after NW growth for 25nm thick and 250nm diameter Au dots. (a) 250nm dots with mesa support annealed at 550°C for 5 minutes. (b) NWs grown from the sample shown in (a). The length bars indicate 1μm.

3.53 35nm Au Thickness Dot Structures

Samples containing 35nm Au thickness are shown in Figures 3.64 to 3.67

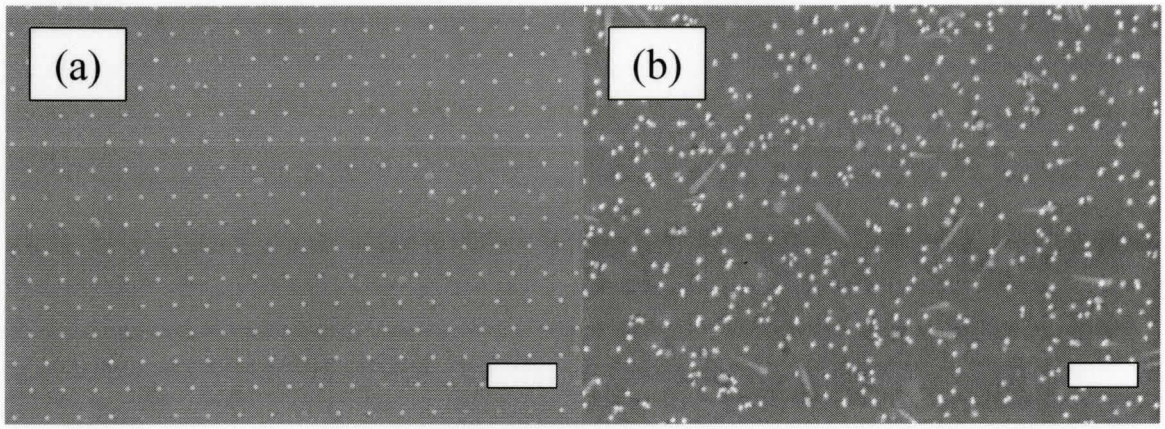

Figure 3.64. Top view SEM images comparing samples before and after NW growth for 35nm thick and 60nm diameter Au dots. (a) 60nm dots with mesa support annealed at 550°C for 5 minutes. (b) NWs grown from the sample shown in (a). The length bars indicate 1μm.

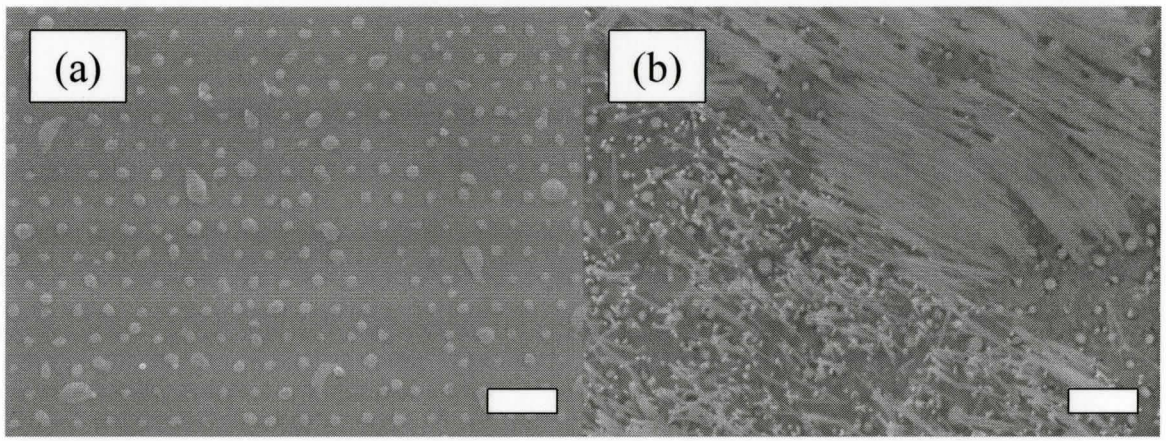

Figure 3.65. Top view SEM images comparing samples before and after NW growth for 35nm thick and 140nm diameter Au dots. (a) 140nm dots with mesa support annealed at 550°C for 5 minutes. (b) NWs grown from the sample shown in (a). A portion of wires in (b) have been tilted from interaction with the electron beam. The length bars indicate 1μm.

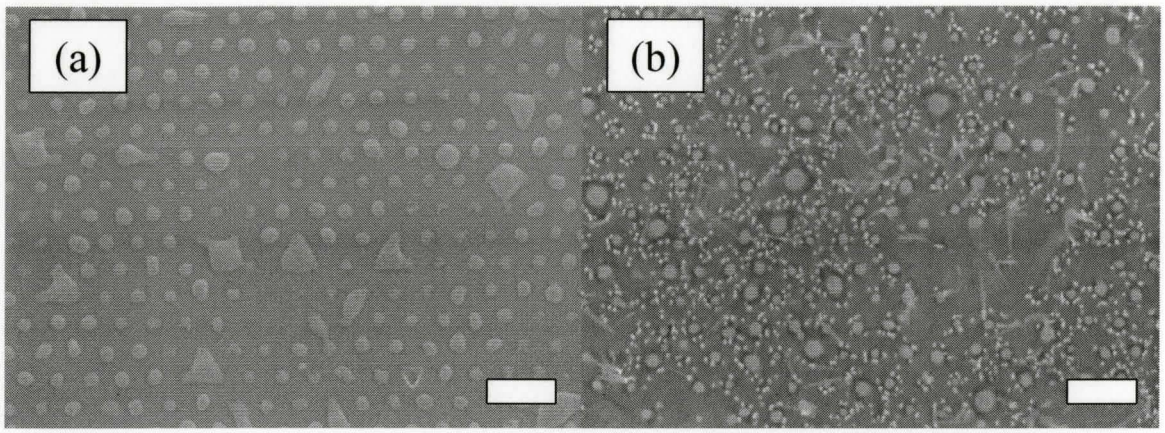

Figure 3.66. Top view SEM images comparing samples before and after NW growth for 35nm thick and 180nm diameter Au dots. (a) 180nm dots with mesa support annealed at 550°C for 5 minutes. (b) NWs grown from the sample shown in (a). The length bars indicate 1μm.

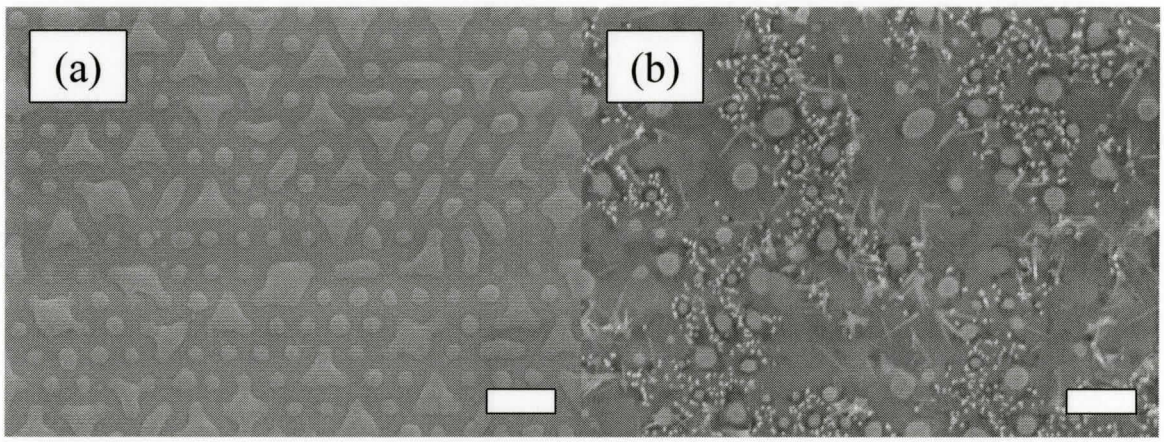

Figure 3.67. Top view SEM images comparing samples before and after NW growth for 35nm thick and 250nm diameter Au dots. (a) 250nm dots with mesa support annealed at 550°C for 5 minutes. (b) NWs grown from the sample shown in (a). The length bars indicate 1μm.

3.54 50nm Au Thickness Dot Structures

Samples containing 50nm Au thickness are shown in Figures 3.68 to 3.71

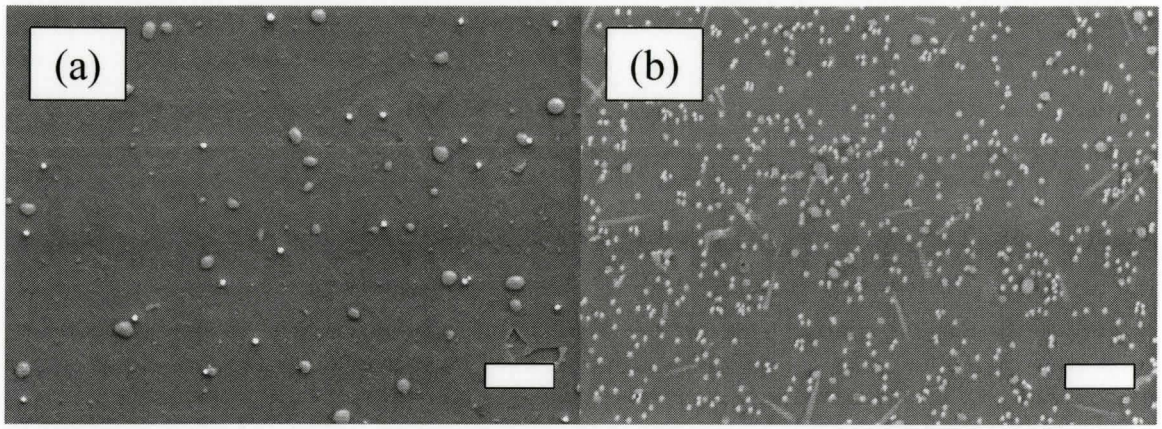

Figure 3.68. Top view SEM images comparing samples before and after NW growth for 50nm thick and 60nm diameter Au dots. (a) 60nm dots with mesa support annealed at 550°C for 5 minutes. (b) NWs grown from the sample shown in (a). The length bars indicate 1μm.

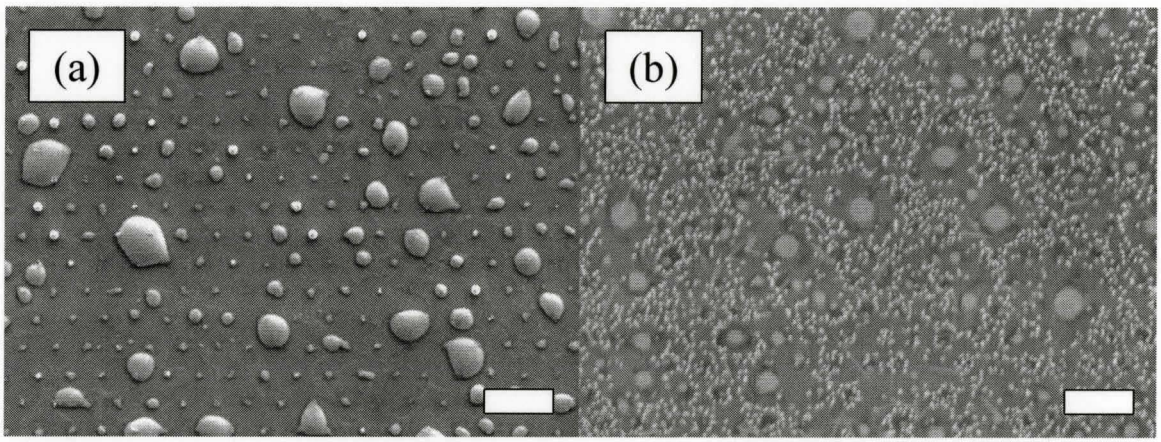

Figure 3.69. Top view SEM images comparing samples before and after NW growth for 50nm thick and 140nm diameter Au dots. (a) 140nm dots with mesa support annealed at 550°C for 5 minutes. (b) NWs grown from the sample shown in (a). The length bars indicate 1μm.

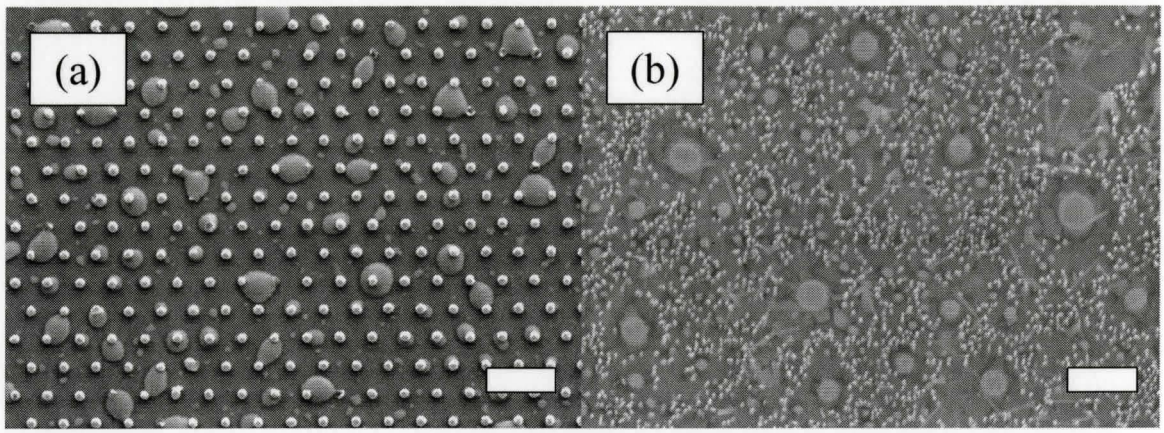

Figure 3.70. Top view SEM images comparing samples before and after NW growth for 50nm thick and 180nm diameter Au dots. (a) 180nm dots with mesa support annealed at 550°C for 5 minutes. (b) NWs grown from the sample shown in (a). The length bars indicate 1μm.

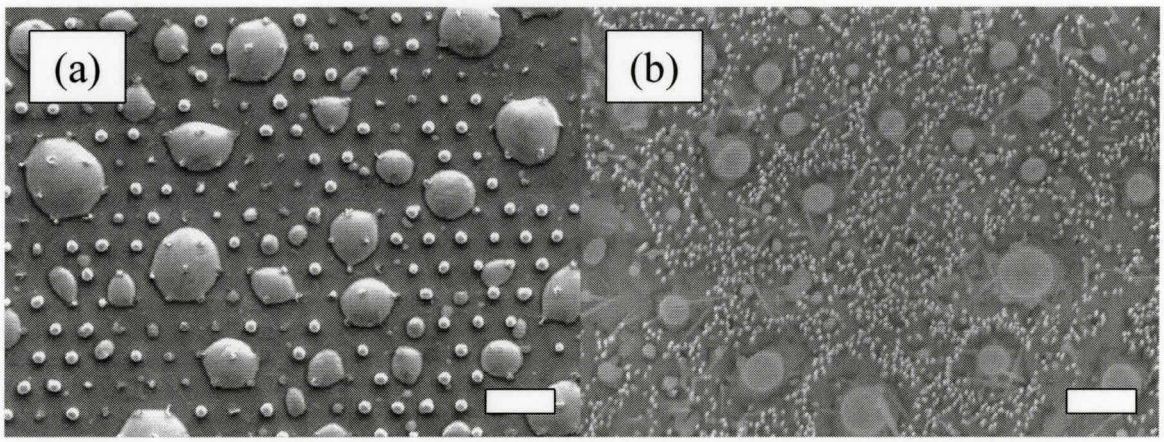

Figure 3.71. Top view SEM images comparing samples before and after NW growth for 50nm thick and 250nm diameter Au dots. (a) 250nm dots with mesa support annealed at 550°C for 5 minutes. (b) NWs grown from the sample shown in (a). The length bars indicate 1μm.

In the images of this section, it is apparent that the best results were obtained with the 15nm thick Au and the 180 and 250nm diameter dots. These cases also represented the best results obtained with the annealing experiments. In the latter case, NWs grew

from the locations of the original Au dots. However, it is also apparent that the Au dots were the source of many smaller Au seed particles from which smaller diameter NWs grew on the entire substrate surface. The precise reason for this observation is presently unclear although a number of conjectures can be made. Concurrent with NW growth, there also exists 2-D film growth occurring on the surface between the NWs. If the height of the 2-D film growth surpasses the height of the original mesa, the functionality of the mesa would be lost and the Au-Ga particle would migrate in a similar manner as seen without mesa support. This process would occur if there were initially a delay in NW growth compared to film growth; for example, due to the time for supersaturation of the Au particle before the onset of NW growth. Uptake of Ga may also destroy the mesa. The growth temperature conditions in the GS-MBE system also differs from that in the RTA, including annealing duration and ramp rate before the onset of growth. The GS-MBE increases temperature at a rate of 10°C per minute with intermittent pauses to allow the substrate temperature to equilibrate. In comparison, the RTA ramped at approximately 5°C per second. Consequently, the annealing time before MBE growth was much greater and more gradual when compared to the annealing time during the RTA experiments.

3.6 Mesa Assisted Annealing vs. Mesa Assisted Growth (Lines)

As was the case in the dot patterns after NW growth, the mesa-assisted line patterns were in much better condition in comparison to the results of the line structures without mesas. However, both the dot and line structures experienced

similar pitfalls during the growth process. That is, the mesas did not contain the Au entirely As well, the uniqueness of the line structures provided an expectation that NW growth would be confined by the geometry of the line. This was not observed in the following SEM images.

3.61 15nm Au Thickness Line Structures

The following section compares the results of line patterns before and after growth as shown in Figures 3.72 to 3.75.

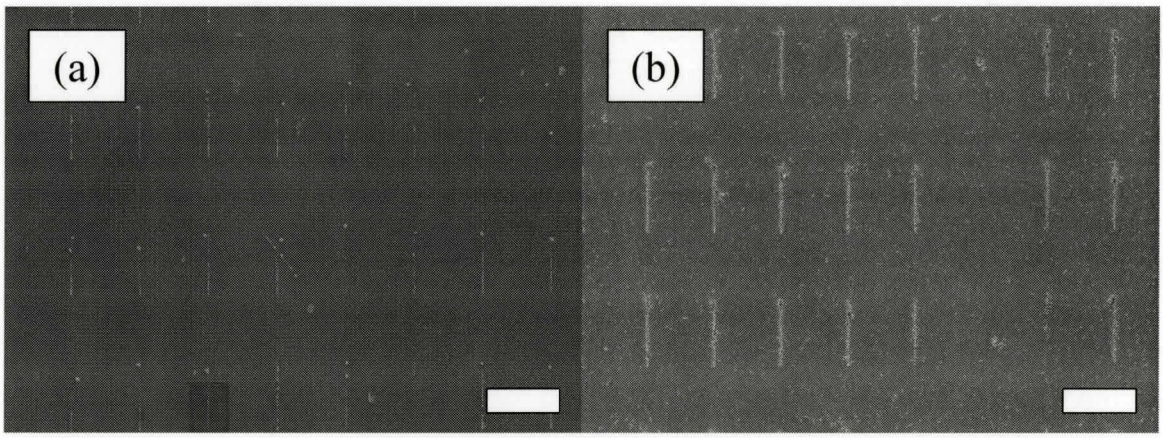

Figure 3.72. Comparison of samples before and after growth for 15nm thick and 60nm wide lines. (a) 60nm lines with mesa support annealed at 550°C for 5 minutes. (b) NWs grown from the sample shown in (a). The length bars indicate 10μm.

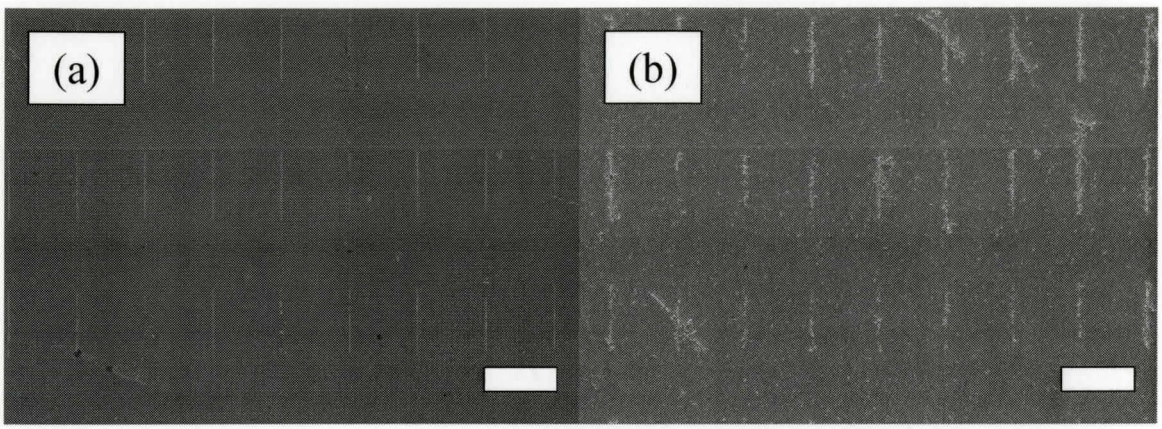

Figure 3.73. Comparison of samples before and after growth for 15nm thick and 150nm wide lines. (a) 150nm lines with mesa support annealed at 550°C for 5 minutes. (b) NWs grown from the sample shown in (a). The length bars indicate 10μm.

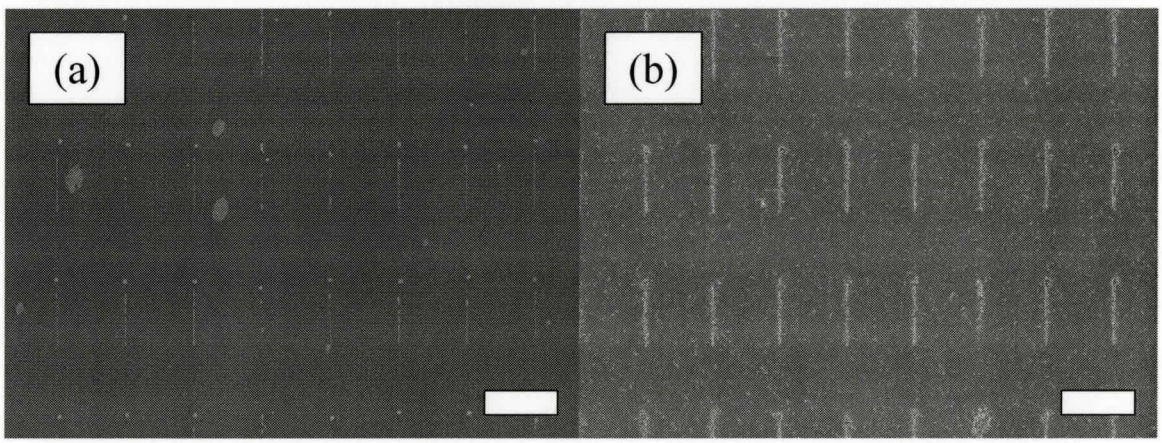

Figure 3.74. Comparison of samples before and after growth for 15nm thick and 200nm wide lines. (a) 200nm lines with mesa support annealed at 550°C for 5 minutes. (b) NWs grown from the sample shown in (a). The length bars indicate 10μm.

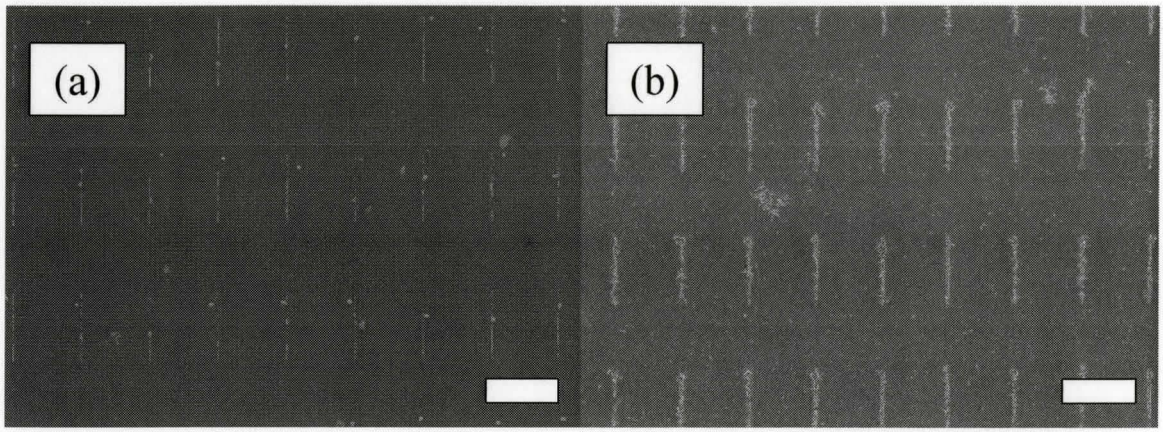

Figure 3.75. Comparison of samples before and after growth for 15nm thick and 300nm wide lines. (a) 300nm lines with mesa support annealed at 550°C for 5 minutes. (b) NWs grown from the sample shown in (a). The length bars indicate 10μm.

Of interest in all growth cases with mesa support is the concentration of wires near the prescribed mesa. The wires seem to grow in a nearly single-file line along the length of the mesa in cases where the original line width is small (in the 15nm Au thickness samples, only the 60nm linewidth produced single-file wires). This effect is shown in Figure 3.76 below

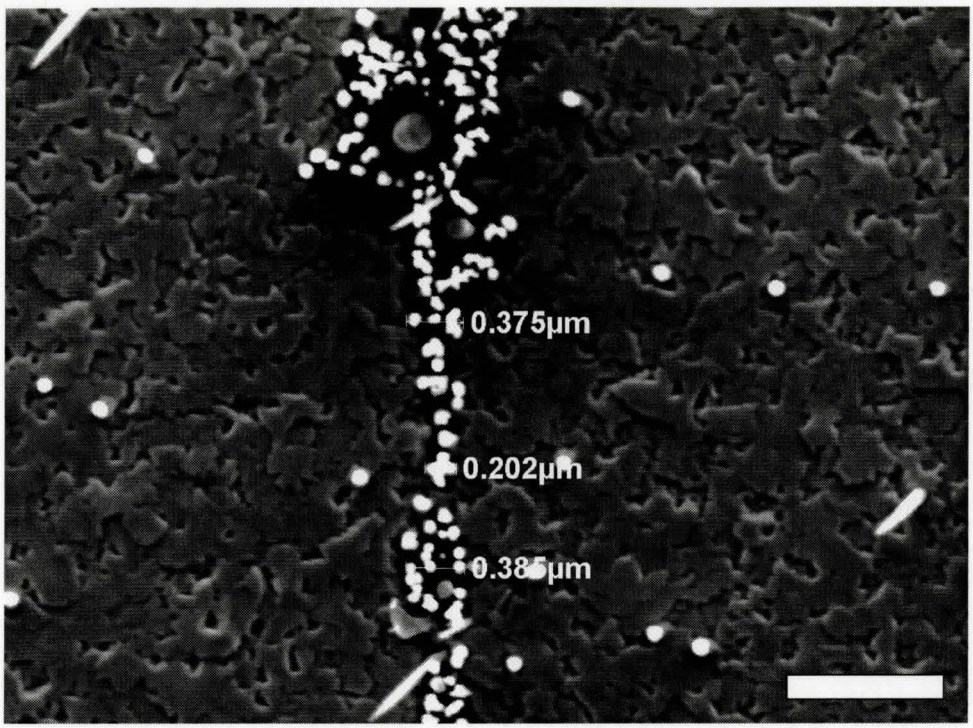

Figure 3.76. Top view SEM image of wire growth for a 60nm wide line. The length bar indicates 1µm.

However, as the linewidth increases, the number of wires that fit along the width of the mesa also increases. From these results, it appears as though the diameter of the wire will not conform entirely to the width prescribed by the Au structure. As the line width increased, the wires appear to have grown around the perimeter of the original mesa location (rather than uniformly dispersed) as shown in Figure 3.77

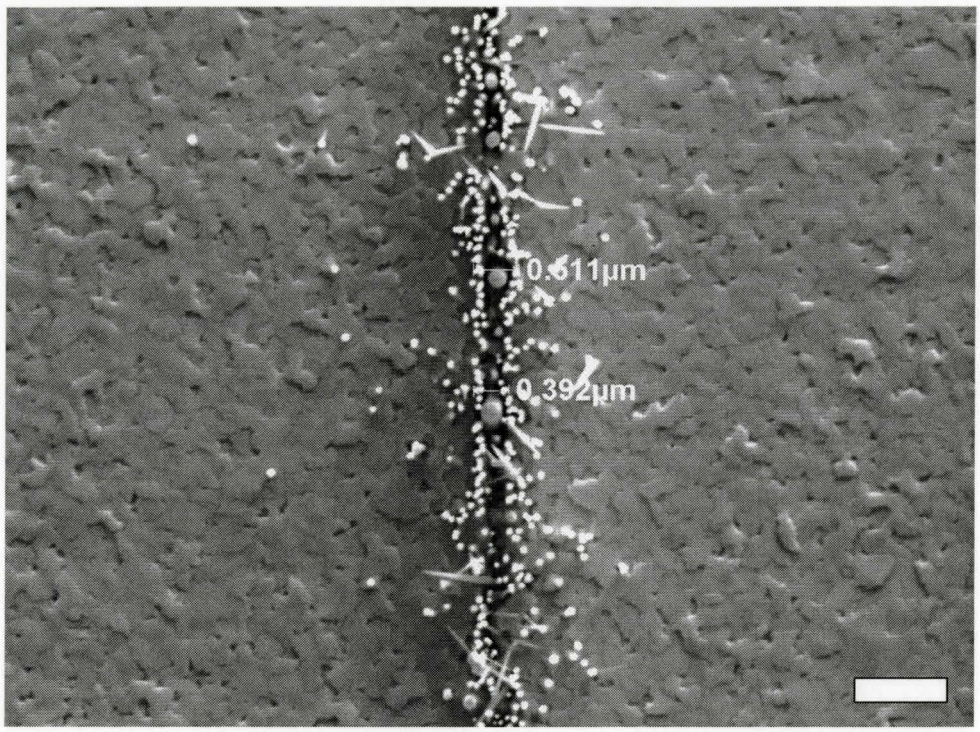

Figure 3.77. Top view SEM image of wire growth for a 200nm wide line. The length bar indicates 1µm.

The spatial extent of the wire growth is much wider than the prescribed width of the line. Both Figure 3.76 and 3 77 show linewidth much larger than the initial EBL-prescribed width.

3.62 25nm Au Thickness Line Structures

In the case of 25nm structures, similar results are observed as shown in Figures 3 78 to 3.82.

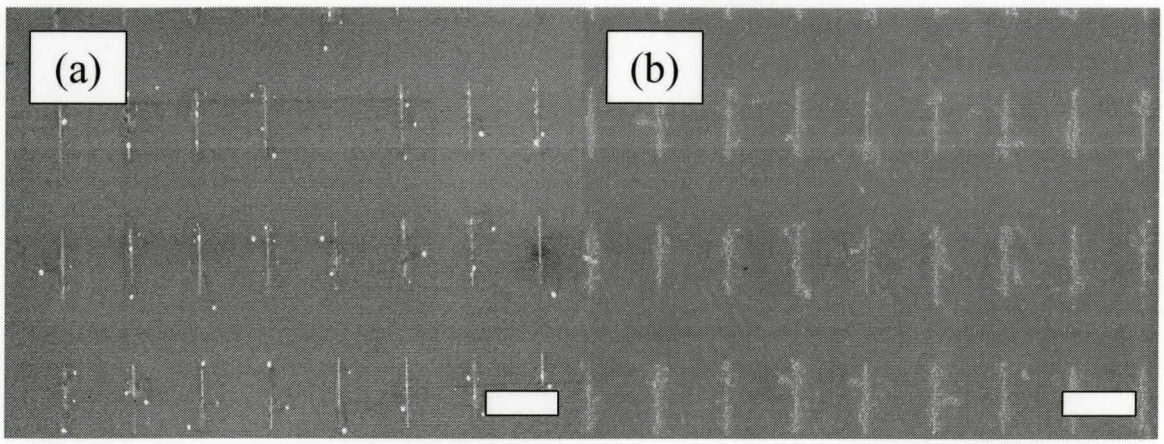

Figure 3.78. Comparison of samples before and after growth for 25nm thick and 60nm wide lines. (a) 60nm lines with mesa support annealed at 550°C for 5 minutes. (b) NWs grown from the sample shown in (a). The length bars indicate 10μm.

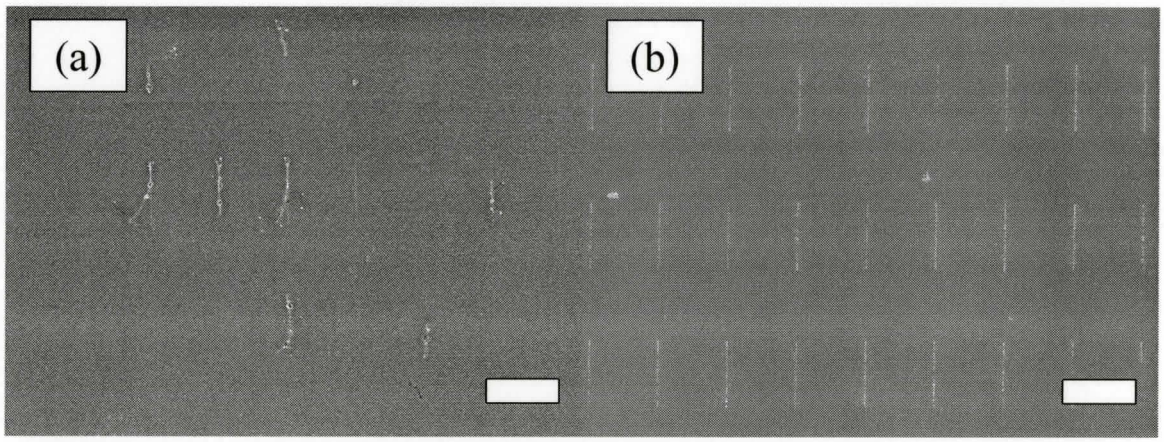

Figure 3.79. Comparison of samples before and after growth for 25nm thick and 120nm wide lines. (a) 120nm lines with mesa support annealed at 550°C for 5 minutes. (b) NWs grown from the sample shown in (a). The length bars indicate 10μm.

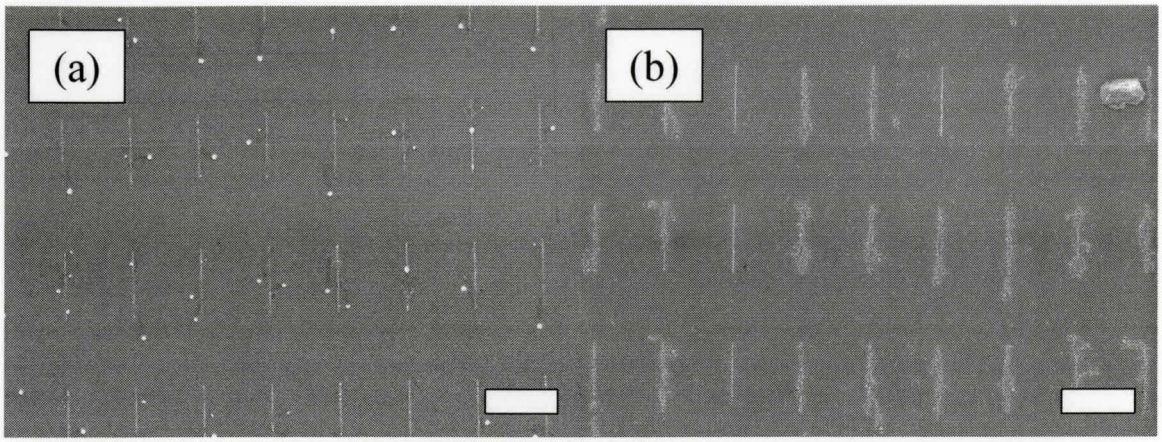

Figure 3.80. Comparison of samples before and after growth for 25nm thick and 150nm wide lines. (a) 150nm lines with mesa support annealed at 550°C for 5 minutes. (b) NWs grown from the sample shown in (a). The length bars indicate 10μm.

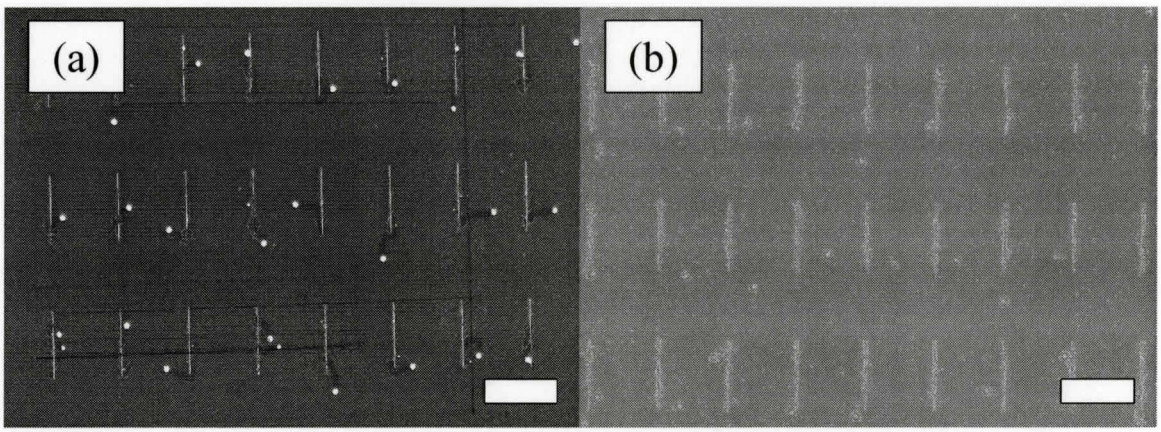

Figure 3.81. Comparison of samples before and after growth for 25nm thick and 200nm wide lines. (a) 200nm lines with mesa support annealed at 550°C for 5 minutes. (b) NWs grown from the sample shown in (a). The length bars indicate 10μm.

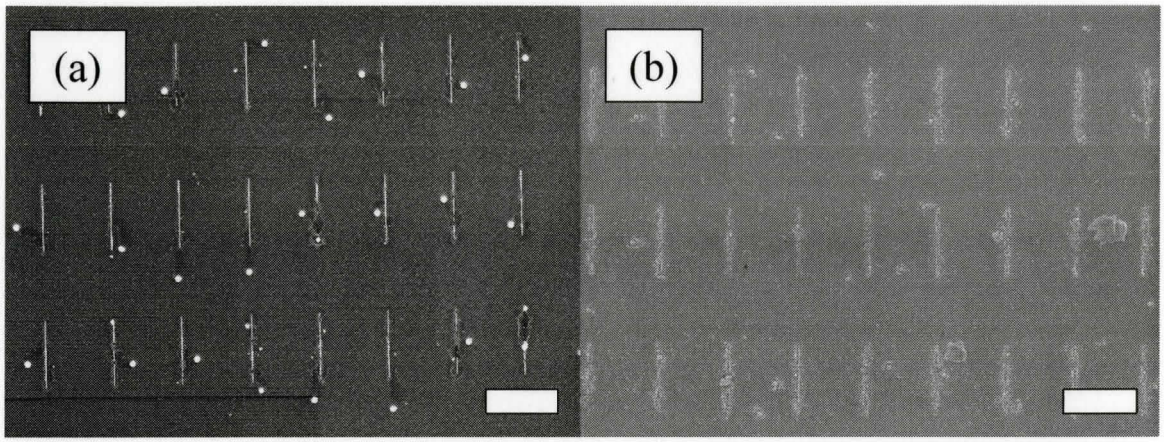

Figure 3.82. Comparison of samples before and after growth for 25nm thick and 300nm wide lines. (a) 300nm lines with mesa support annealed at 550°C for 5 minutes. (b) NWs grown from the sample shown in (a). The length bars indicate 10μm.

3.63 35nm Au Thickness Line Structures

Results for the 35nm Au structures are shown in Figures 3.83 to 3.87

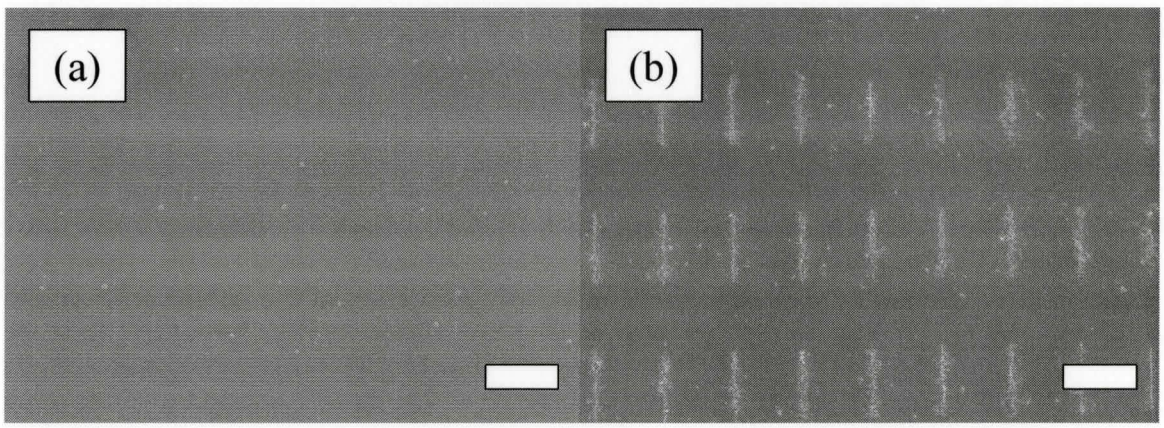

Figure 3.83. Comparison of samples before and after growth for 35nm thick and 60nm wide lines. (a) 60nm lines with mesa support annealed at 550°C for 5 minutes. (b) NWs grown from the sample shown in (a). The length bars indicate 10μm.

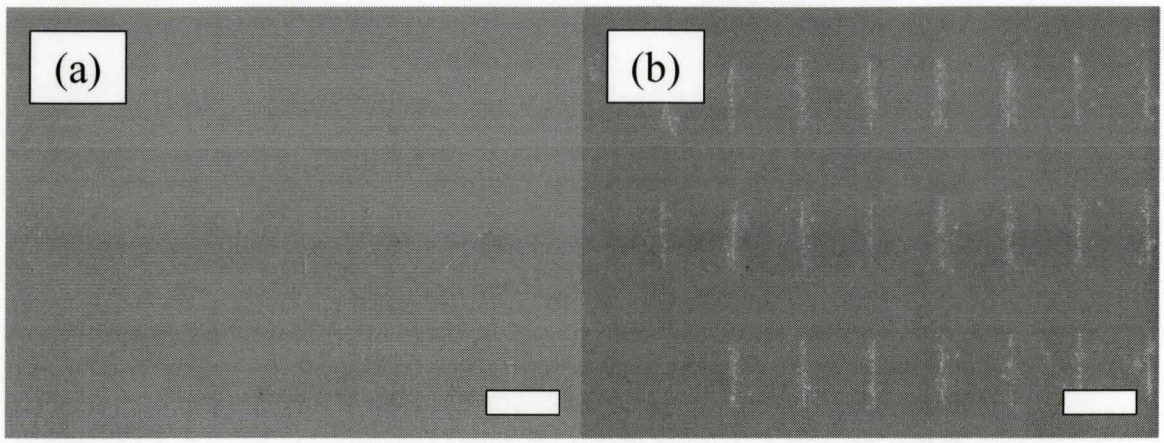

Figure 3.84. Comparison of samples before and after growth for 35nm thick and 120nm wide lines. (a) 120nm lines with mesa support annealed at 550°C for 5 minutes. (b) NWs grown from the sample shown in (a). The length bars indicate 10μm.

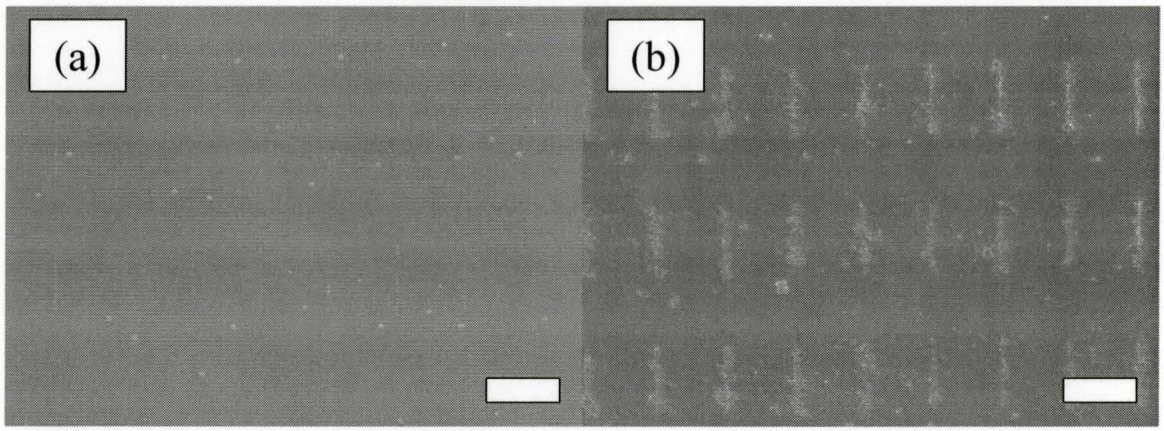

Figure 3.85. Comparison of samples before and after growth for 35nm thick and 150nm wide lines. (a) 150nm lines with mesa support annealed at 550°C for 5 minutes. (b) NWs grown from the sample shown in (a). The length bars indicate 10μm.

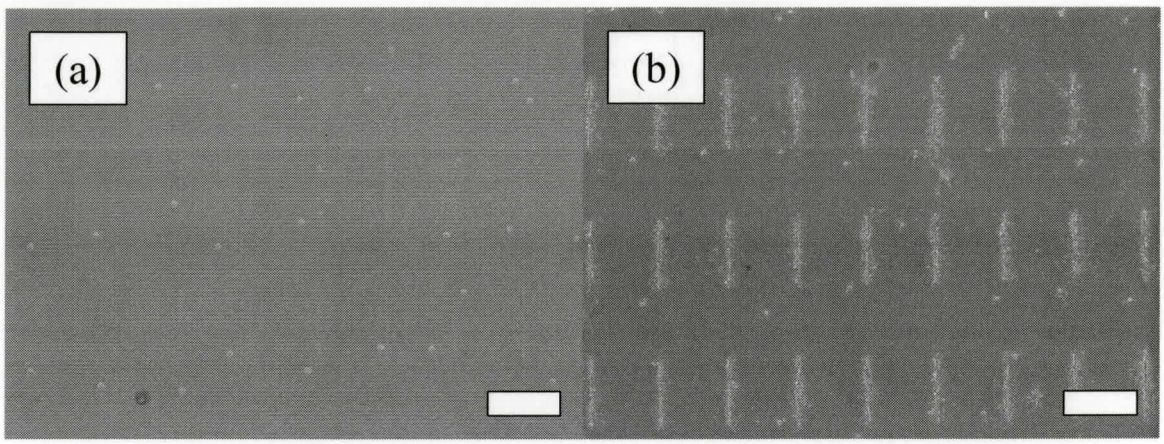

Figure 3.86. Comparison of samples before and after growth for 35nm thick and 200nm wide lines. (a) 200nm lines with mesa support annealed at 550°C for 5 minutes. (b) NWs grown from the sample shown in (a). The length bars indicate 10μm.

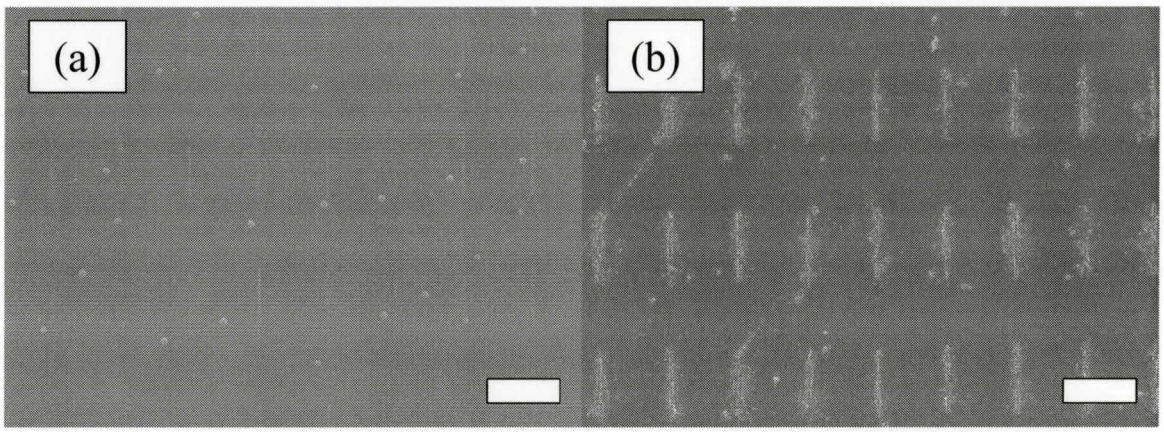

Figure 3.87. Comparison of samples before and after growth for 35nm thick and 200nm wide lines. (a) 200nm lines with mesa support annealed at 550°C for 5 minutes. (b) NWs grown from the sample shown in (a). The length bars indicate 10μm.

3.64 50nm Au Thickness Line Structures

Evidence of migration and fractionation are observed over all the line structures. However, even in the case of simple annealing in the RTA, the quality of the array is reduced as the Au becomes thicker. As was the case for the dot structures, it is apparent

in Figures 3.88 to 3.91 that the Au thickness was too great for containment by the mesa. The line structures at 50nm thickness were especially poor after growth. Au migrated and NWs grew on the order of a micron from the original line location.

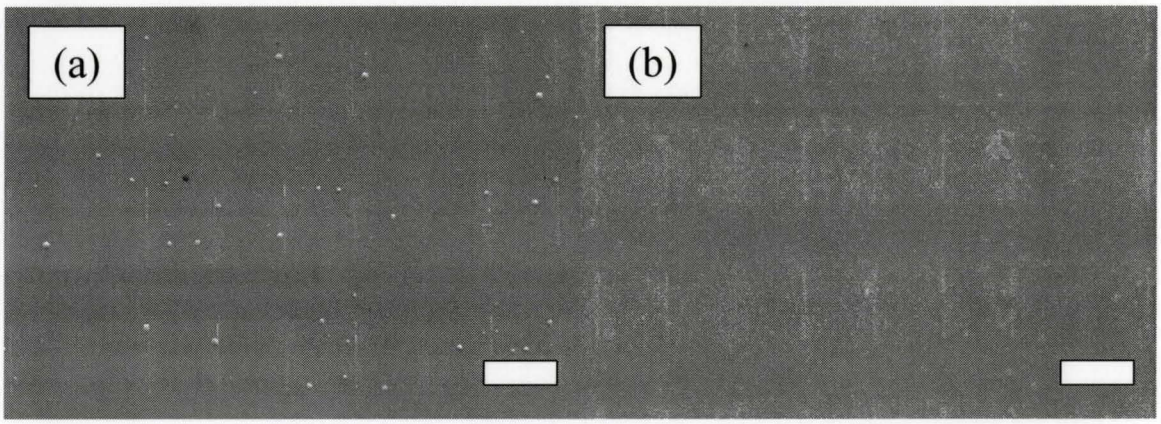

Figure 3.88. Comparison of samples before and after growth for 50nm thick and 60nm wide lines. (a) 60nm lines with mesa support annealed at 550°C for 5 minutes. (b) NWs grown from the sample shown in (a). The length bars indicate 10μm.

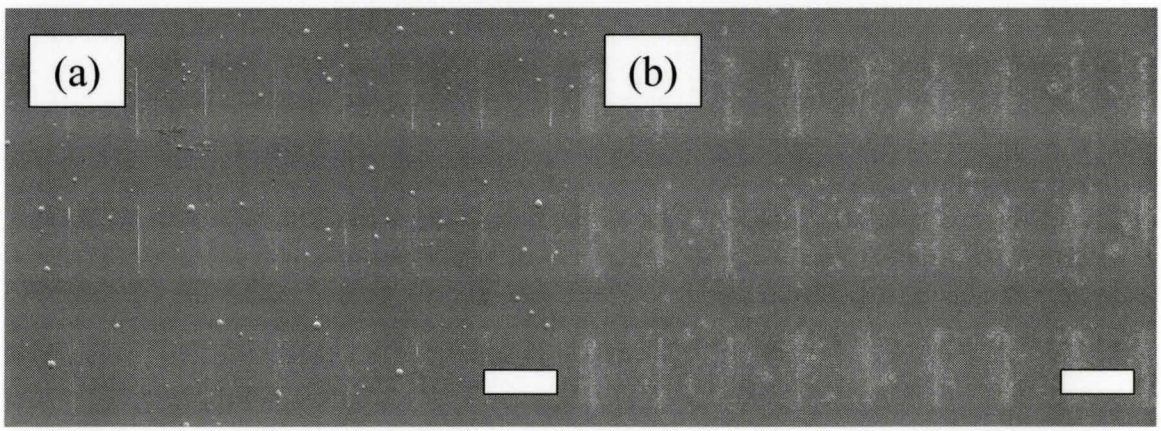

Figure 3.89. Comparison of samples before and after growth for 50nm thick and 150nm wide lines. (a) 150nm lines with mesa support annealed at 550°C for 5 minutes. (b) NWs grown from the sample shown in (a). The length bars indicate 10μm.

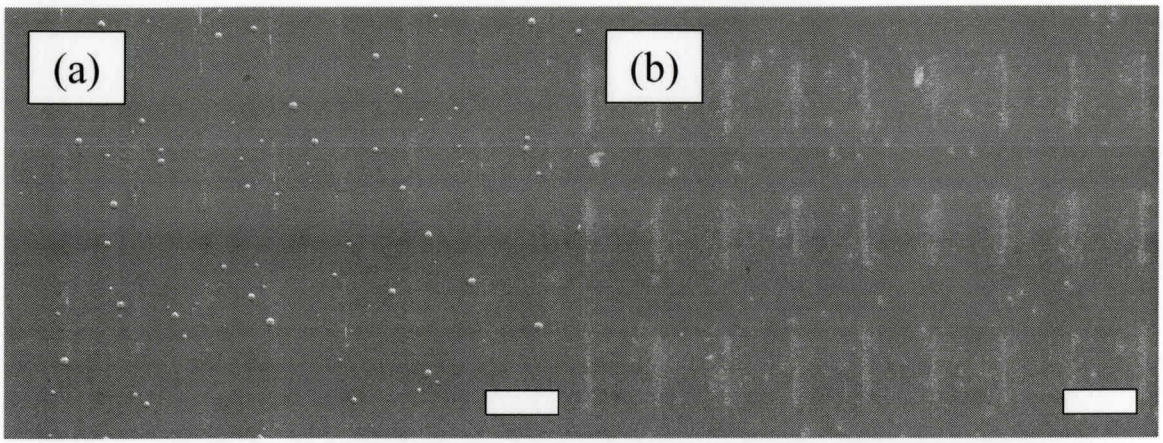

Figure 3.90. Comparison of samples before and after growth for 50nm thick and 200nm wide lines. (a) 200nm lines with mesa support annealed at 550°C for 5 minutes. (b) NWs grown from the sample shown in (a). The length bars indicate 10μm.

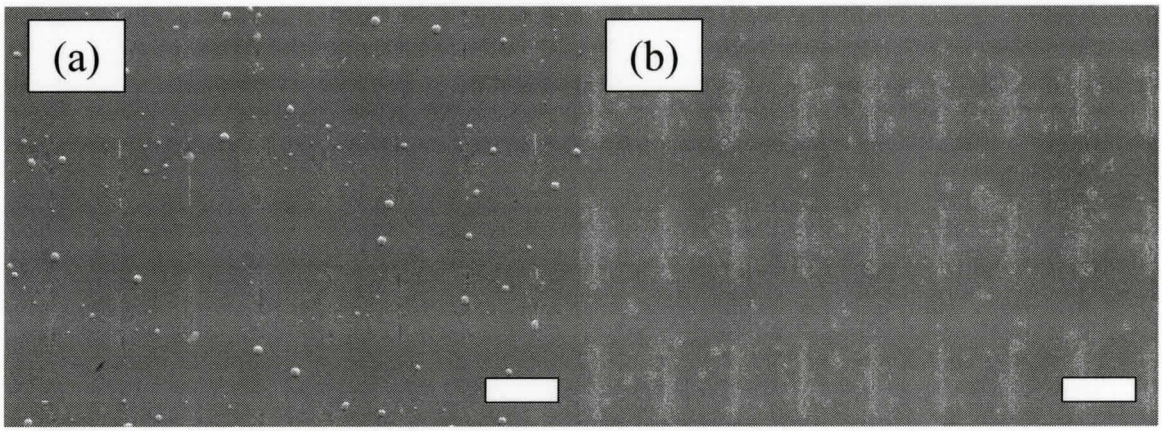

Figure 3.91. Comparison of samples before and after growth for 50nm thick and 300nm wide lines. (a) 300nm lines with mesa support annealed at 550°C for 5 minutes. (b) NWs grown from the sample shown in (a). The length bars indicate 10μm.

3.7 Chapter Summary

The analysis of the Au-Ga phase diagram reveals the structure of the Au-Ga alloy and is applied to provide an estimate of the radius of the melted Au-Ga structure upon cooling to room temperature. When the natural contact angle of the Au-Ga alloy

produces a resulting Au-Ga structure diameter which exceeds the diameter of the etched mesa by more than approximately 25%, the liquid alloy spills over the structure and migration is permitted to occur. Coupled with the results observed via SEM, this suggests that the surface tension modeling will permit the wires to grow as expected when certain dimension ratios are met between the diameter of the mesa and the height of the Au. As well, the discrepancy between results observed before and after growth indicates differences between RTA annealing and MBE growth processes. It is suspected that 2-D film growth on the substrate prior to NW growth may render the mesa less effective. The 2-D film growth that occurs at a rate of 1μm/hr requires only 2 minutes in order to surpass the 30-50nm height of the mesa sacrificing the functionality of the structure. Similar results were found when examining the line structures in section 3.4 and 3.6.

4 Conclusions and Future Work

Patterns were fabricated via EBL to design periodic arrays of Au structures on GaAs (111)B substrates. Samples were reproduced twice identically. One set of samples was etched using a selective etchant employing the Au as a shadow mask to produce mesa structures on which the Au rested. The other set was used as a control sample. Both sets of samples were annealed at typical growth temperatures (550°C) for 5 minutes and later analyzed via SEM. In general, Au structures with mesa support were in significantly better condition than their counterparts without support. A model is proposed to describe the diameter of the resulting truncated sphere after the Au structure is melted. It is shown that the surface tension provided by the mesa structure is sufficient in confining Au particles in which the resulting Au-Ga island diameter is no greater than approximately 15 to 25% of the mesa diameter. To more precisely define the capability of the mesa to support larger diameter Au structures, further experiments are required with a more well-defined set of Au thicknesses for a given diameter. In general, this would be best achieved by creating structures with a larger mesa diameter or a smaller Au thickness. However, it is preferable to focus efforts towards creating smaller structures, in which case decreasing the initial Au diameter and drastically lowering the Au thickness to fit within the limits of the 25% diameter criterion would be ideal.

After annealing experiments were completed, the sample set with mesa support was exposed to VLS growth conditions in the GS-MBE system. SEM imaging was then completed and comparison was made between the annealed samples and their grown

counterparts (both with mesa support). Differences between the annealed and grown samples were obvious. In most cases, the mesas provided almost no support and NWs were randomly distributed over the substrate surface with little evidence of periodicity except in a few cases. In samples with the best annealing results (15nm Au thickness with 140, 180, 250nm diameter and 25nm Au thickness with 250nm diameter), NWs did grow in the prescribed pattern designed by EBL processing. NWs also grew outside of the mesa structure as well though, indicating Au was not entirely confined by the mesas. It is suspected that the functionality of the mesas is reduced when exposed to GS-MBE growth conditions because the onset of NW growth is dependent on the growth interface saturating with adatoms. Before this occurs, 2-D film growth continues at a rate of 1μm/hr. With mesas on the order of 30-50nm, only 2 to 3 minutes are required for the 2-D film growth to overtake the height of the mesa structure. Uptake of Ga may also destroy the mesa. In order to confirm this, mesa structures of significantly greater height could be constructed. However, wet etching a deeper mesa is difficult as undercutting of the mesa could potentially remove the Au structures from the surface. More detailed experiments to precisely define the maximum possible mesa height without losing Au structures could be completed. As well, other routes towards confining the periodic Au structures could be explored. This includes dry etching mesas through reactive ion etching as well as using pits or holes to confine the NW growth.

Line structures provided unique insight into the migration of Au after both annealing and growth. While the general trends were similar, the dot patterns were designed with a very small pitch (500nm) making it very difficult to track Au migration.

In the case of lines, the pitch was very large (10μm). Upon growing NWs, it was clearly evident which NWs belonged to a particular Au structure despite achieving NWs which grew up to a few microns from the original structure.

The intermediate annealing experiments were useful in analyzing the ability of the mesa to confine the Au structure. Before designing experiments to grow NWs with functional mesas, Au structures with appropriate volumes should be fabricated. The 15% standard provides only a starting point for calculating the final diameter of the Au structure evolving from the pillbox to the truncated sphere. The RTA annealing conditions should also more accurately represent the annealing conditions in the GS-MBE. The drastically different temperature ramp rates as well as soak time (over the drawn out GS-MBE ramping process) provides the Au significantly more time to migrate.

Producing periodic arrays to withstand typical NW conditions requires two immediate improvements on the sample parameters used in this thesis. That is, 1) mesa structures of a given diameter must have a specific Au height in order for the truncated sphere to remain confined during the growth procedure, and 2) a means to grow NWs in which the 2-D film growth on the substrate does not render the mesa structures dysfunctional.

References

[1.1] M. K. Sunkara, S. Gubbala and J. Thangala, "Nanowire-based electrochromic devices," *Solar Energy Mater. Solar Cells,* vol. 91, pp. 813-20, 05/23. 2007.

[1.2] Y. Li, F. Qian, J. Xiang and C. M. Lieber, "Nanowire electronic and optoelectronic devices," *Materials Today,* vol. 9, pp. 18-27, 10. 2006.

[1.3] D. P. Norton, H. Young-Woo, L. C. Tien, M. P. Ivill, Y. Li, B. S. Kang, F. Ren, J. Kelly, A. F. Hebard and S. Pearton, "ZnO spintronics and nanowire devices," in *Progress in Compound Semiconductor Materials IV - Electronic and Optoelectronic Applications,* 2005, pp. 339-350.

[1.4] Pei Li-Zhai, Tang Yuan-Hong, Chen Yang-Wen, Z. Yong and G. Chi, "Nanoelectronic devices fabricated technology with Si nanowire," *Electronic Components & Materials,* vol. 23, pp. 44-7, 10. 2004.

[1.5] Sung-Wook Chung, Jae-Young Yu and J. R. Heath, "Silicon nanowire devices," *Appl. Phys. Lett.,* vol. 76, pp. 2068-70, 04/10. 2000.

[1.6] J. Motohisa, J. Takeda, M. Inari, J. Noborisaka and T. Fukui, "Growth of GaAs/AlGaAs hexagonal pillars on GaAs (111)B surfaces by selective-area MOVPE," in *Fifth International Workshop on Epitaxial Semiconductors on Patterned Substrates and Novel Index Surfaces (ESPS-NIS),* 2004, pp. 298-304.

[1.7] Y. Huang, X. Duan, Y. Cui, L. J. Lauhon, K. -. Kim and C. M. Lieber, "Logic gates and computation from assembled nanowire building blocks," *Science,* vol. 294, pp. 1313-17, 11/09. 2001.

[1.8] S. Kasai and H. Hasegawa, "A single electron binary-decision-diagram quantum logic circuit based on Schottky wrap gate control of a GaAs nanowire hexagon," *IEEE Electron Device Lett.,* vol. 23, pp. 446-8, 08. 2002.

[1.9] M. Shin, "Quantum simulation of device characteristics of silicon nanowire FETs," *IEEE Transactions on Nanotechnology,* vol. 6, pp. 230-7, 03. 2007.

[1.10] J. Hahm and C. M. Lieber, "Direct ultrasensitive electrical detection of DNA and DNA sequence variations using nanowire nanosensors," *Nano Letters,* vol. 4, pp. 51-4, 01. 2004.

[1.11] F. Patolsky, G. Zheng and C. M. Lieber, "Large-scale, multiplexed electrical detection of proteins and viruses by ultrasensitive nanowire sensor arrays," in *208th Meeting of the Electrochemical Society,* 2005, pp. 766.

[1.12] A. B. Greytak, C. J. Barrelet, Y. Li and C. M. Lieber, "Semiconductor nanowire laser and nanowire waveguide electro-optic modulators," *Appl. Phys. Lett.*, vol. 87, pp. 151103, 2005.

[1.13] X. Duan, Y. Huang, Y. Cui, J. Wang and C. M. Lieber, "Indium phosphide nanowires as building blocks for nanoscale electronic and optoelectronic devices," *Nature,* vol. 409, pp. 66-9, 01/04. 2001.

[1.14] Y. Huang, X. Duan and C. M. Lieber, "Nanowires for integrated multicolor nanophotonics," *Small,* vol. 1, pp. 142-147, 2005.

[1.15] H. Pettersson, J. Tragardh, A. I. Persson, L. Landin, D. Hessman and L. Samuelson, "Infrared photodetectors in heterostructure nanowires," *Nano Letters,* vol. 6, pp. 4, 02. 2006.

[1.16] E. Yablonovitch, "Inhibited spontaneous emission in solid-state physics and electronics," *Phys. Rev. Lett.*, vol. 58, pp. 2059-62, 05/18. 1987.

[1.17] H. W. Kim and S. H. Shim, "Growth of MgO nanowires assisted by the annealing treatment of Au-coated substrates," *Chemical Physics Letters,* vol. 422, pp. 165-169, 2006.

[1.18] C. Chen, M. C. Plante, C. Fradin and R. R. LaPierre, "Layer-by-layer and step-flow growth mechanisms in GaAsP/GaP nanowire heterostructures," *J. Mater. Res.*, vol. 21, pp. 2801-9, 11. 2006.

[1.19] R. S. Wagner and W. C. Ellis, "Vapor-liquid-solid mechanism of single crystal growth," *Appl. Phys. Lett.*, pp. 89, 1964.

[1.20] K. A. Dick, K. Deppert, L. S. Karlsson, L. R. Wallenberg, L. Samuelson and W. Seifert, "A new understanding of Au-assisted growth of III-V semiconductor nanowires," *Advanced Functional Materials,* vol. 15, pp. 1603-10, 10. 2005.

[1.21] J. Noborisaka, J. Motohisa, S. Hara and T. Fukui, "Growth and characterization of GaAs/AlGaAs core-shell nanowires and AlGaAs nanotubes," in *NSTI Nanotech 2005,* 2005, pp. 225-8.

[1.22] H. J. Joyce, Y. Kim, Q. Gao, H. H. Tan and C. Jagadish, "Growth, structural and optical properties of GaAs/AlGaAs core/shell nanowires with and without quantum well shells," in *2006 International Conference on Nanoscience and Nanotechnology,* 2007, pp. 4.

[1.23] M. Paladugu, J. Zou, G. J. Auchterlonie, Y. N. Guo, Y. Kim, H. J. Joyce, Q. Gao, H. H. Tan and C. Jagadish, "Evolution of InAs branches in InAs/GaAs nanowire heterostructures," *Appl. Phys. Lett.*, vol. 91, pp. 1-3, 2007.

[1.24] L. J. Lauhon, M. S. Gudiksen, D. Wang and C. M. Lieber, "Epitaxial core-shell and core-multishell nanowire heterostructures," *Nature,* vol. 420, pp. 57-61, 11/07. 2002.

[1.25] S. Gradecak, F. Qian, Y. Li, Hong-Gyu Park and C. M. Lieber, "GaN nanowire lasers with low lasing thresholds," *Appl. Phys. Lett.,* vol. 87, pp. 173111-1, 10/24. 2005.

[2.1] R. F. Egerton, "Physical Principles of Electron Microscopy: An Introduction to TEM, SEM, and AEM", New York: Springer, 2005, pp. 125-129.

[2.2] L. Reimer, "Scanning Electron Microscopy: Physics of Image Formation and Microanalysis", Heidelberg: Springer-Verlag, 1985, pp. 20-36.

[2.3] L. Reimer, "Scanning Electron Microscopy: Physics of Image Formation and Microanalysis", Heidelberg: Springer-Verlag, 1985, pp. 3-7.

[2.4] R. F. Egerton, "Physical Principles of Electron Microscopy: An Introduction to TEM, SEM, and AEM", New York: Springer, 2005, pp. 137-139.

[2.5] R. F. Egerton, "Physical Principles of Electron Microscopy: An Introduction to TEM, SEM, and AEM", New York: Springer, 2005, pp. 131-136.

[2.6] G. R. Brewer, "Electron Beam Technology in Microelectronic Fabrication", New York: Academic Press, 1980, pp. 11-17.

[2.7] J. Drelich and K. L. Mittal, "Atomic Force Microscopy in Adhesion Studies", Netherlands: VSP, 2005, pp. 4-9.

[2.8] M. A. Herman and H. Sitter, "Molecular Beam Epitaxy: Fundamentals and Current Status", New York: Springer-Verlag, 1996, pp. 1-32.

[3.1] L. F. Garcia, J. Silva-Valencia, I. D. Mikhailov and J. E. Galvan-Moya, "Ground state energies of neutral and negatively charged donors in nanowire superlattice," *Physica B: Physics of Condensed Matter,* vol. 403, pp. 5-11, 01/01. 2008.

[3.2] M. Willatzen, R. V. N. Melnik, C. Galeriu and Lew Yan Voon, L.C., "Quantum confinement phenomena in nanowire superlattice structures," *Math. Comput. Simul.,* vol. 65, pp. 385-97, 05/11. 2004.

[3.3] A. Zhang, L. C. L. Y. Voon and M. Willatzen, "Dynamics of a nanowire superlattice in an ac electric field," *Physical Review B (Condensed Matter and Materials Physics),* vol. 73, pp. 45316-1, 01/15. 2006.

[3.4] P. Mohan, J. Motohisa and T. Fukui, "Controlled growth of highly uniform, axial/radial direction-defined, individually addressable InP nanowire arrays," *Nanotechnology,* vol. 16, pp. 2903-7, 12. 2005.

[3.5] V. G. Dubrovskii, G. E. Cirlin, I. P. Soshnikov, A. A. Tonkikh, N. V. Sibirev, Y. B. Samsonenko and V. M. Ustinov, "Diffusion-induced growth of GaAs nanowhiskers during molecular beam epitaxy: theory and experiment," *Physical Review B (Condensed Matter and Materials Physics),* vol. 71, pp. 205325-1, 05/15. 2005.

[3.6] V. G. Dubrovskii, N. V. Sibirev, G. E. Cirlin, J. C. Harmand and V. M. Ustinov, "Theoretical analysis of the vapor-liquid-solid mechanism of nanowire growth during molecular beam epitaxy," *Physical Review E (Statistical, Nonlinear, and Soft Matter Physics),* vol. 73, pp. 21603-1, 02. 2006.

[3.7] L. Schubert, P. Werner, N. D. Zakharov, G. Gerth, F. M. Kolb, L. Long, U. Gosele and T. Y. Tan, "Silicon nanowhiskers grown on Si substrates by molecular-beam epitaxy," *Appl. Phys. Lett.,* vol. 84, pp. 4968-70, 06/14. 2004.

[3.8] M. C. Plante, J. Garrett, S. C. Ghosh, P. Kruse, H. Schriemer, T. Hall and R. R. LaPierre, "The formation of supported monodisperse Au nanoparticles by UV/ozone oxidation process," *Appl. Surf. Sci.,* vol. 253, pp. 2348-2354, 2006.

[3.9] H. Baker, L. H. Bennett, T. B. Massalski and J. L. Murray, "Binary Alloy Phase Diagrams", vol. 1, 1986, pp. 258-261.

[3.10] H. Baker, L. H. Bennett, T. B. Massalski and J. L. Murray, "Binary Alloy Phase Diagrams", vol. 1, 1986, pp. 191-192.

[3.11] M. Ohring, "The Materials Science of Thin Films", San Diego: Academic Press Ltd., 1992, pp. 213-219.

[3.12] D. A. Porter and K. E. Easterling, "Phase Transformations in Metals and Alloys", London: Chapman & Hall, 1992, pp. 110-116.

[3.13] M. Ohring, "The Materials Science of Thin Films", San Diego: Academic Press Ltd., 1992, pp. 198-206.

[3.14] M. Li and W. A. Goddard III, "Interstitial-electron model for lattice dynamics in FCC metals," *Physical Review B (Condensed Matter),* vol. 40, pp. 12155-63, 12/15. 1989.

[3.15] I. G. Edmunds and M. M. Qurashi, "The structure of γ-phase in the silver-zinc system," *Acta Cryst.,* pp. 417, 1951.